Investigation of indium-rich InGaN alloys and kinetic growth regime of GaN

THÈSE N^{O} 5776 (2013)

PRÉSENTÉE LE 5 JUILLET 2013
À LA FACULTÉ DES SCIENCES DE BASE
LABORATOIRE EN SEMICONDUCTEURS AVANCÉS POUR LA PHOTONIQUE ET L'ÉLECTRONIQUE
PROGRAMME DOCTORAL EN PHOTONIQUE

ÉCOLE POLYTECHNIQUE FÉDÉRALE DE LAUSANNE

POUR L'OBTENTION DU GRADE DE DOCTEUR ÈS SCIENCES

PAR

Nils Asmus Kristian KAUFMANN

acceptée sur proposition du jury:

Prof. C. Moser, président du jury
Prof. N. Grandjean, directeur de thèse
Prof. E. Calleja Pardo, rapporteur
Dr J.-D. Ganière, rapporteur
Prof. P. Parbrook, rapporteur

ÉCOLE POLYTECHNIQUE
FÉDÉRALE DE LAUSANNE

Suisse
2013

God made the bulk;
surfaces were invented by the devil.
— Wolfgang Ernst Pauli

This dissertation is dedicated to my family

Acknowledgements

I am very grateful to the great number of people who have offered me their help over the last four and a half years while I was pursuing this work, and to my family and friends who have been very supportive during that time. Although I cannot name them all here a few people deserve a particularly special mention.

Firstly, I would like to thank my supervisor, Prof. Nicolas Grandjean, for giving me the opportunity to work on this interesting project, and for all the support he has offered me. I would also like to thank Prof. Michael Heuken, my former supervisor in Aachen, who ignited my interest in the field of semiconductors and guided me towards the nitrides. At the EPFL, I want to give special thanks to Amelie Dussaigne who introduced me to the MBE growth, and to Denis Martin who was a great support and help during the whole time. I want to mention the rest of the MBE team, Marco Malinverni, Etienne Giraud and Lise Lahourcade, whom I have to thank for countless discussion and good feedback. For introduction and help with the MOVPE, I want to thank Jean-Francois Carlin, as well as Eric Feltin and Jerome Napierala and again Lise and Denis. The people who shared the office with me, Gatien Cosendey, Georg Rossbach and Jacques Levrat, I thank for the good time we spent together.

Finally, but by no means least, I would like to thank my parents, my brother and my fiancé for their support.

This thesis was supported by and carried out in the framework of the Marie Curie initial training network Rainbow (FP7).

Lausanne, 29 Mai 2013 Nils A. K. Kaufmann

Abstract

Nowadays, light emitting diodes (LEDs) and laser diodes (LDs) are part of our daily life. More and more devices incorporate InGaN-based optoelectronic devices. In fact, since the first demonstration of a candela-class InGaN-based LED in the beginning of the nineties, those LEDs have quickly become popular. The efficiency of blue InGaN LEDs is nowadays very high and when coated with a yellow phosphor, they can efficiently emit white light. Such white LEDs are more and more used for different lighting applications, from home lighting to car lighting. Another application of blue InGaN emitters that is found in many households is the Blu-ray disc, based on a 405 nm LD. The great success of the III-nitrides in the blue range created a strong interest to extend the wavelength range into the green, as efficient green emitters are missing. However, their performance is still low compared to their blue counterparts.

The goal of this dissertation is to investigate issues that limit the performance of green InGaN LEDs and LDs. To achieve efficient green emission, the growth temperature needs to be reduced to incorporate more indium into the active region. In this context, the present study is divided into two parts. In the first one, the growth regime of GaN as a function of the temperature is investigated and the physical origin of the surface features is discussed. When lowering the temperature, the so called Ehrlich-Schwöbel barrier, a barrier at the step-edges, causes a different attachment probability for the adatoms arriving from the different sides. This asymmetry can lead to the appearance of three different kinetic surface morphologies: hillocks, fingers, or step-bunching. After presenting the theory, the three different regimes are demonstrated for GaN, and the growth parameters that allow to control the morphology are investigated. Indeed, the different morphologies usually reported for the different growth techniques can be attributed to the different growth parameters commonly used. In the end of the first part, the influence of the underlaying morphology on the properties of the active region of an LED is discussed.

In the second part, the impact of the thermal budget on the properties of InGaN quantum wells (QWs) is discussed. Active regions with a high In content can degrade easily when the *p*-type layer is grown on top, due to being exposed to a too high thermal budget. This is especially critical for green LDs which require thick cladding layers, *i.e.* a long growth time. The origin of the degradation and the parameters influencing it are discussed first: when an In-rich QW is annealed at a too high temperature, its emission intensity is reduced and dark spots appear on PL maps. The annealing temperature causing this degradation depends on the indium content, the QW thickness and the number of QWs. It is shown that these dark spots exhibit a peculiar emission spectra, with a characteristic emission at 2.75 eV. This emission is tentatively attributed to nitrogen vacancies that are created by the formation of metallic indium clusters in the active region. Then the focus is laid on the beneficial effects that can take place when an In-rich active region is exposed to a moderate thermal budget. Apart from reducing the linewidth of the emission, a strong improvement in photoluminescence intensity can be achieved. This improvement increases for high indium content QWs, *i.e.* when the growth temperature is low. In fact, this improvement is more pronounced for molecular beam epitaxy grown structures whose active regions are grown at a much lower temperatures than their metal organic vapor phase epitaxy counterparts. This is tentatively ascribed to the reduction of point defects by thermal annealing. As a consequence, a moderate annealing can be beneficial for both to reduce the non-radiative recombinations and the linewidth. It is finally proposed to perform a short annealing step of high indium content QWs before growing the *p*-type (cladding) layer at low temperature.

Keywords: III-nitrides, gallium nitride, indium gallium nitride, light emitting diodes, laser diodes, Ehrlich-Schwöbel barrier, growth kinetics, thermal annealing, point defects

Zusammenfassung

Leuchtdioden (LEDs, von engl. *light emitting diode*) und Laserdioden (LDs) sind heutzutage Teil unseres alltäglichen Lebens. Immer mehr Geräte verwenden InGaN basierte optoelektronische Bauteile. Seit der ersten Demonstration einer InGaN basierten LED in den späten Achtzigern des 20ten Jahrhunderts wurden solche LEDs schnell populär. Die Effizienz von blauen InGaN LEDs ist sehr hoch. Beschichtet mit einem gelben Phosphor können sie weißes Licht ausstrahlen. Solche weißen LEDs werden mehr und mehr für Beleuchtungszwecke verwendet. Die Anwendungen reichen von der Innenraumbeleuchtung bis hin zu Autoscheinwerfern. Eine weitere Anwendung von solchen InGaN Emittern, die in vielen Haushalten anzutreffen ist, ist der Blu-ray Player, der auf InGaN LDs mit einer Wellenlänge von 405 nm basiert. Der große Erfolg der blauen InGaN Emitter sorgt für ein großes Interesse, ihre Emissionswellenlänge in den grünen Spektralbereich auszudehnen, da effiziente grüne Halbleiterlichtquellen bisher fehlen.

Das Ziel dieser Dissertation ist die Untersuchung von Problemen, die die Leistung von grünen InGaN LEDs und LDs begrenzen. Um eine effiziente grüne Emission zu erreichen, muß die Wachstumstemperatur des InGaNs gesenkt werden, damit mehr Indium eingebunden werden kann. Dies führt zu Problemen mit der Kristallqualität und der Homogenität der Schichten. In diesem Kontext ist die Studie in zwei Teile aufgeteilt. Im ersten wird die Veränderung des Wachstumsregimes untersucht, welche beim Senken der Wachstumstemperatur auftritt, und der physikalische Ursprung der beobachteten Oberflächenmorphologien wird diskutiert. Wenn die Temperatur gesenkt wird, wird die sogenannte Ehrlich-Schwöbel Barriere relevant. Sie ist eine energetische Barriere für adsorbierte Atome und befindet sich an den Stufenkanten der Wachstumsoberfläche. Sie beeinflusst die Wahrscheinlichkeit einer Anlagerung von adsorbierten Atomen an einer Stufenkante in Abhängigkeit von deren Ursprung: Die Anlagerung von Atomen der darüberliegenden Stufe wird reduziert, wenn eine ausgeprägte Ehrlich-Schwöbel Barriere vorhanden ist. Diese Asymmetrie führt zu dem Entstehen von drei speziellen kinetischen Oberflächenmorphologien: Hügel (engl. *hillocks*), Meander und Stufenbündelung (engl. *step-bunching*). Nach der Vorstellung der entsprechenden Wachstumstheorie werden die drei verschiedenen Wachstumsregimes für GaN präsentiert, und die Wachstumsparameter, die die Kontrolle der Oberflächenmorphologie erlauben, untersucht. In der Tat lassen sich die verschiedenen Oberflächenmorphologien, die sich in der Literatur für die verschiedenen Wachstumsmethoden finden lassen, auf die jeweils typischen

Wachstumsparameter zurückführen. Alle präsentierten Morphologien können jedoch mit sowohl mit metallorganischer Gasphasenepitaxie (MOVPE, von engl. *metallorganic vapor phase epitaxy*) als auch mit Molekularstrahlepitaxie (MBE, von engl. *molecular beam epitaxy*) realisiert werden, wenn die Wachstumsparameter angepasst werden. Am Ende des ersten Teils wird schließlich der Einfluss der darunterliegenden Oberflächenmorphologie auf die Eigenschaften der aktiven Zone einer LED diskutiert.

Im zweiten Teil wird das Problem der thermischen Stabilität betrachtet. Eine aktive Zone mit einem hohen Indiumanteil kann leicht degradieren, falls die darüberliegende p-dotierte Schicht mit einer zu hohen Temperatur aufgewachsen wird. Dies ist besonders relevant für LD, wo die Wachstumszeit der p-dotierten Schichten bis zu zwei Stunden betragen kann und daher ein großes thermisches Budget induziert wird. Der Ursprung der Degradierung und die Parameter, die diese beeinflussen, werden zuerst diskutiert. Wenn eine indiumreiche Struktur mit einer zu hohen Temperatur getempert wird, reduziert sich ihre Emissionsintensität durch Bildung von lokal begrenzten Regionen sehr niedriger Emissionsintensität. Die Tempertemperatur, für die eine Degradierung auftritt, hängt von dem Indiumanteil, der Quantentopf- (QW, von engl. *quantum well*) Dicke und von deren Anzahl ab. Es wird gezeigt, dass jene Regionen mit niedriger Intensität ein geändertes Emissionsspektrum haben, welches eine zusätzliche blaue Emission bei 2,75 eV aufweist. Diese Emission könnte von Stickstoff-Gitterlücken kommen, die durch die Bildung von metallischen Indiumanhäufungen in der aktiven Zone entstehen. Danach fokussiert die Studie auf die vorteilhaften Effekte, die beim Tempern von indiumreichen InGaN Verbindungen auftreten können. Neben der Reduzierung der Photolumineszenz-Linienbreite kann auch eine starke Verbesserung von deren Intensität erreicht werden. Diese Verbesserung erhöht sich mit steigendem Indiumanteil und sinkender Wachstumstemperatur. In der Tat ist diese Verbesserung stärker ausgeprägt für Proben, die mit MBE bei tieferen Temperaturen aufgewachsen wurden, als für Proben, die mit MOVPE hergestellt wurden. Die Verbesserung der Intensität könnte auf einer Reduzierung der Punktdefektdichte durch das Tempern basieren. Tempern kann also eine Verbesserung der Linienbreite und eine Reduzierung der nicht-strahlenden Rekombinationszentren bewirken. Letzteres scheint bereits beim Wachstum von Strukturen mit mehreren QWs einzutreten, bei denen die QWs durch die längere Wachstumsdauer bereits leicht getempert werden. Als Konsequenz wird vorgeschlagen, die aktive Zone von indiumreichen InGaN QWs mit einem passenden thermischen Budget zu tempern, und die anschliessende p-dotierte Schicht bei niedriger Temperatur aufzuwachsen.

Schlagwörter: III-Nitride, Galliumnitrid, Indiumgalliumnitrid, Leuchtdiode, Laserdiode, Ehrlich-Schwöbel Barriere, Wachstumskinetik, Tempern, Punktdefekte

Contents

Introduction

InGaN-based light sources are nowadays common devices for many applications. While their success story started not that long ago, the first investigation of nitride semiconductors started over a century ago, with AlN in 1907 [1], and 25 years later with GaN [2]. GaN was first grown epitaxially on sapphire in 1969 [3]. It was one of the first materials grown by metal organic vapor phase epitaxy (MOVPE) [4]. While its basic properties were investigated [5] and electroluminescence was realized in 1971 [6], this materials system still exhibited a poor crystalline quality. Unlike the other III-V semiconductors, such as GaAs, which experienced a rapid development in the 70s, GaN was held back due to the lack of *p*-conductivity. Only in the late eighties, Amano *et al.* discovered that an activation of magnesium-doped GaN enabled *p*-conductivity [7]. This development led to the first p/n junction and the first GaN light emitting diode (LED).

After the principle of activation of Mg-doped GaN was demonstrated by low-energy electron-beam irradiation, Nakamura *et al.* showed that a simple annealing in a nitrogen atmosphere is sufficient to activate the magnesium [8]. This sparked a rapid development with the realization of the first blue high-brightness LED in 1994 by the company Nichia [9, 10, 11]. Just shortly afterwards, the first injection laser diode (LD) was demonstrated [12].

Nowadays, InGaN-based LEDs cover a broad spectral range, from yellow down to UV [13]. However, the highest efficiency of InGaN-based LEDs and LDs is obtained for blue emission [14]. Both are becoming more and more part of the everyday life. As an example, blue LDs are used to increase the density of information in optical data storage (Blu-ray discs) and LEDs are used for displays (e.g. in TVs, laptops, outdoor screens, or mobile phones). The most striking application is the white LED which is used for lighting, e.g. in cars, streets, or houses. To obtain white emission, a blue InGaN LED is covered with a yellow phosphor [15]: the phosphor absorbs part of the light emitted by the InGaN layer and reemitts in the yellow spectral range. The resulting spectra is perceived as white by the human eye. By adjusting the phosphor material, the color can be perceived warmer (yellowish) or colder (blueish).

Despite their widespread commercial applications, III-nitrides have still unsolved issues, such as the strong drop in efficiency for devices emitting in the green range. Indeed, the success of blue InGaN LEDs and LDs created an interest to extend those highly efficient devices to a longer wavelength range. Green LDs could be used e.g for pico-projectors, while yellow ones could have potential biomedical applications. However, the device performance drops strongly when the wavelength is increased. In a review, Wu called this issue the “green valley of death” [13]. Indeed, not only the efficiency of the InGaN-based emitter drops strongly when approaching the green range, but the same happens to phosphide-based light emitters, usually used for red LEDs, when approaching the green gap from the other side of the spectrum.

One of the main issues is to maintain a high crystalline quality while increasing the indium content to reach green emission [16]. Typically, over 25 % indium is needed for efficient green emitters [17]. This makes green high brightness LEDs and LDs very challenging, because of alloy disorder and thermal stability. Although several companies have published very promising results on green LDs since 2009 [18, 19, 20], only a handful of them are able to market green LDs.

One of the issues to achieve high indium content alloys needed for such devices is the thermal stability of the In-rich InGaN alloy. This implies a low growth temperature. In this context, different growth techniques, molecular beam epitaxy (MBE) and MOVPE, have been considered. MOVPE is the technique of choice for industrial production and MBE is mainly used for research, at least for III-nitrides. Actually, MBE grown GaN-based devices have not reached the performance of their MOVPE counterparts yet. Böttcher called this “the “scientific” world of MBE” and “the “magic” world of MOVPE” [21].

The manuscript starts with a short introduction which presents the basics of the materials system, the growth techniques, and the analyzing tools. Then the manuscript consists of two distinct studies. In the first part, the effect of the growth kinetics on the growth mode is investigated for both MOVPE and MBE, and the physics behind the different observed surface morphologies is discussed. In the second part, the thermal stability and materials quality of In-rich InGaN QWs grown at low temperatures are are studied, with a focus on the effect of the temperature on point defect density.

1 Basics of the III-nitrides and experimental techniques

In this part, some of the basics of the III-nitrides will be reviewed first, with a focus on growth-related issues. Then, the experimental growth techniques and the tools used for layer characterization will be presented.

1.1 Introduction to the group-III nitrides

The first focus is on the basic materials properties of the III-nitride system. Note that for very basic concepts, the reader is referred to references [22, 23], as the main focus will be on the concepts that will play a role for the experimental part.

Gallium nitride (GaN), indium nitride (InN) and aluminum nitride (AlN) are the building blocks of nitride-based optoelectronic devices. Other binary III-nitride compounds like boron nitride (BN) are not used for devices and will not be discussed further here. GaN, InN and AlN share common features. They form crystals in the hexagonal wurtzite structure (space group C_{6v}^4 / point group C_{6v}). A schematic of the wurtzite structure is displayed in Fig. 1.1. Each type

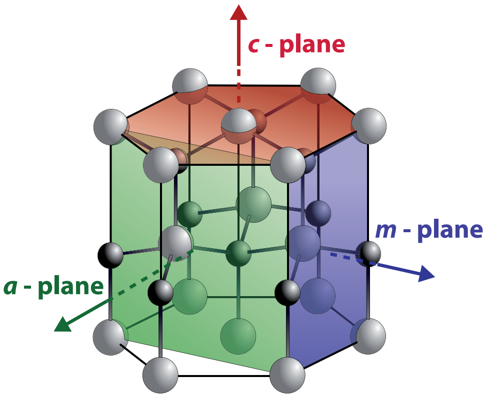

Figure 1.1: Schematic drawing of a HCP unit cell for a binary compounds, by courtesy of G. Rossbach (LASPE-EPFL).

Table 1.1: Basic properties of the III-nitrides, taken from [13] and [24, 25, 26, 27, 28, 29].

Parameter:	AlN	GaN	InN
Lattice constant a at 300K (nm) [24]	0.3112	0.3189	0.3533
Thermal expansion along a (10^{-6}/K) [24]	4.2	5.6	3.8
Lattice constant c at 300K (nm) [24]	0.4982	0.5185	0.5693
Thermal expansion along c (10^{-6}/K) [24]	5.3	3.2	2.9
Bandgap E_g at 0K (eV) [25]	6.25	3.51	0.69
Bandgap E_g at 300K (eV) [25]	6.14	3.43	0.64
Varshni parameter α (meV/K) [25]	1.799	0.909	0.414
Varshni parameter β (K) [25]	1462	830	454
Exciton binding energy (meV)	48 [26]	27 [27, 28]	5 [29]
Spontaneous polarization (C/m^2) [25]	-0.090	-0.034	-0.042

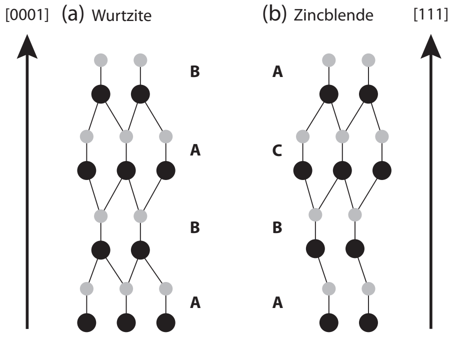

Figure 1.2: Schematic drawings of the (a) AB AB and (b) ABC ABC stacking orders along the polar c-axis for wurtzite and zincblende crystals, respectively. Adapted from [30].

of atom (metal and nitrogen) is arranged in a hexagonal close-packed system, shifted with respect to the other along the c-axis ([0001]). The lattice parameters of each of the three binary compounds are given in Tab. 1.1. Note that it is also possible to obtain a metastable cubic zincblende phase for III-nitrides grown under certain conditions. However, only the wurtzite structure is treated in this work.

The wurtzite structure is characterized by an AB AB sequence, while zincblende has an ABC ABC one (see Fig. 1.2). Each atomic layer is rotated by 30° in-plane with respect to the subsequent one. One important phenomenon arises from the wurtzite structure. The barycenters of the positive and negative charges are not superimposed along the c-axis [30]. This leads to spontaneous polarization in the bulk material along the so-called polar c-axis. The magnitude of the spontaneous polarization depends on the deviation from the ideal crystal structure. Moreover, external stress can induce a piezoelectric polarization by deforming the lattice. These two types of polarization are displayed in Fig. 1.3. Similarly, an applied external field can also deform the lattice, as a reversal of the piezoelectric effect. The spontaneous polarization coefficients of the binary compounds are given in Tab. 1.1. Those of the ternary alloys are not

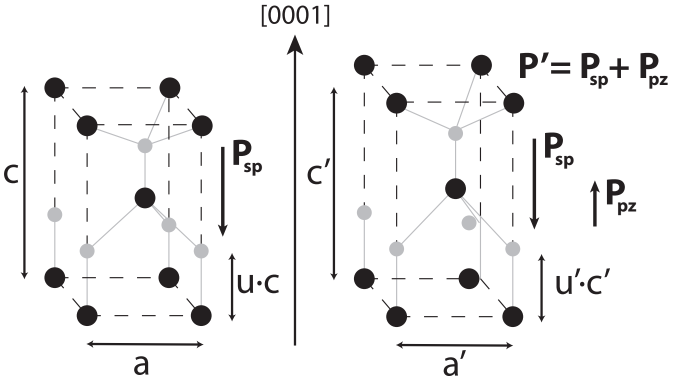

Figure 1.3: Schematic representation of the (a) spontaneous (P_{sp}) and (b) piezoelectric (P_{pz}) polarization in III-nitrides. Adapted from [30].

Table 1.2: Valence band offset and bowing parameters of the ternary alloys

Parameter	AlN-GaN	GaN-InN	AlN-InN
Valence band offset (eV) [31]	-0.7	-1.1	-1.8
Alloy bandgap bowing (eV)	0.6 [32]	1.4 [33]	5.0 [34]

simple linear combination but exhibit a bowing [30].

As mentioned in the introduction, the importance of the III-nitrides for the optoelectronic industry comes from the fact that they are wide bandgap semiconductors, which also have a direct bandgap, thus allowing a direct emission of photons. Furthermore, the bandgaps of the three binary compounds cover a broad spectrum (see Tab. 1.1), including the whole visible range from the UV (6.14 eV for AlN) to the infrared (0.64 eV for InN).

For most applications, combinations of binary compounds are used to synthesize ternary alloy or quaternary alloys. Their bandgaps *vs* lattice parameters are displayed in Fig. 1.4. A few things need to be discussed in more detail. First, the bandgaps of ternary alloys are bent following the Eq. (1.1) for an $A_{1-x}B_xN$ alloy:

$$E_g(x) = E_g(AN) \cdot (1-x) + E_g(BN) \cdot x - b \cdot x \cdot (1-x), \tag{1.1}$$

with b the bowing parameter, given by Tab. 1.2 for each ternary alloy. Second, at an interface between two different semiconductors, there is a valence band discontinuity [31]. These values are also given in Tab 1.2 for the case of binary compound interfaces. Third, alloys with a high indium content are especially challenging to realize, due to the different in lattice parameters of the binaries they are made of.

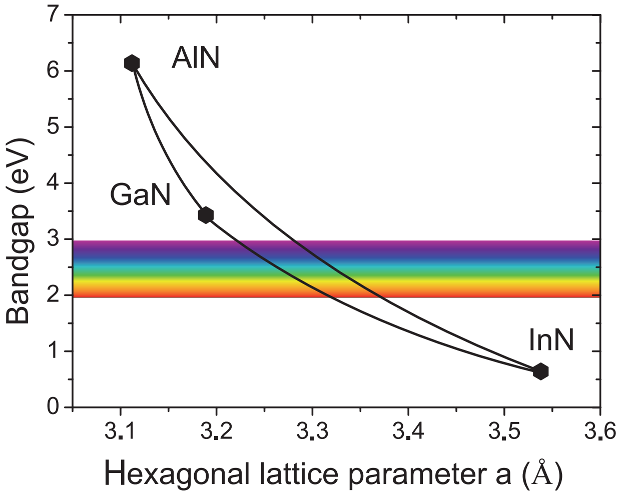

Figure 1.4: Bandgap energy over lattice parameter for III-nitrides.

1.2 Epitaxy and growth-related issues

Growing one material on itself (e.g. GaN on GaN) is called homoepitaxy, otherwise, it is called heteroepitaxy (e.g. InGaN or AlN on GaN). Homoepitaxially grown layers are *de facto* lattice-matched, as well as some alloys that can be latticed-matched to other materials. The most notable for the III-nitrides is $In_{0.17}Al_{0.83}N$, which is lattice-matched to GaN when grown along the *c*-axis [35].

In heteroepitaxy, depending on whether the underlaying layer has a smaller or a larger lattice parameter, the top layer is under compressive or tensile strain, respectively. Usually, the strain causes the in-plane lattice structure of the top layer to adapt to the underlaying one, while deforming the lattice parameter in the growth direction. This typically happens for thin layers. The second option is that the top layer relaxes to its original lattice parameter *via* the introduction of crystal defects at the interface, or gradually after a certain thickness. This happens when the elastic energy, which depends on the thickness and the strain, becomes too high. These processes are schematically displayed in Fig. 1.5.

One can not discuss growth and strain without addressing the issue of the substrate. A substrate should meet several requirements, mainly a similar lattice parameter (or at least enabling a minimal strain) and a similar thermal expansion coefficient to the subsequently grown material. One can also add a good thermal conductivity, a suitable surface chemistry, the ability to be mechanically structured (e.g. offcut) and last but not least, the availability and affordability are also important requirements. The use of foreign substrates generally leads to the formation of various defects, as well as to cracks, which affect the optical and electrical properties. Delamination, especially for different thermal expansion coefficients, e.g. for GaN on silicon (Si), may also occur. No foreign lattice-matched substrates are available for the III-nitride system [36]. However, bulk GaN substrates have become available and their quality has improved over the past years, but they are still very expensive. As a consequence, foreign

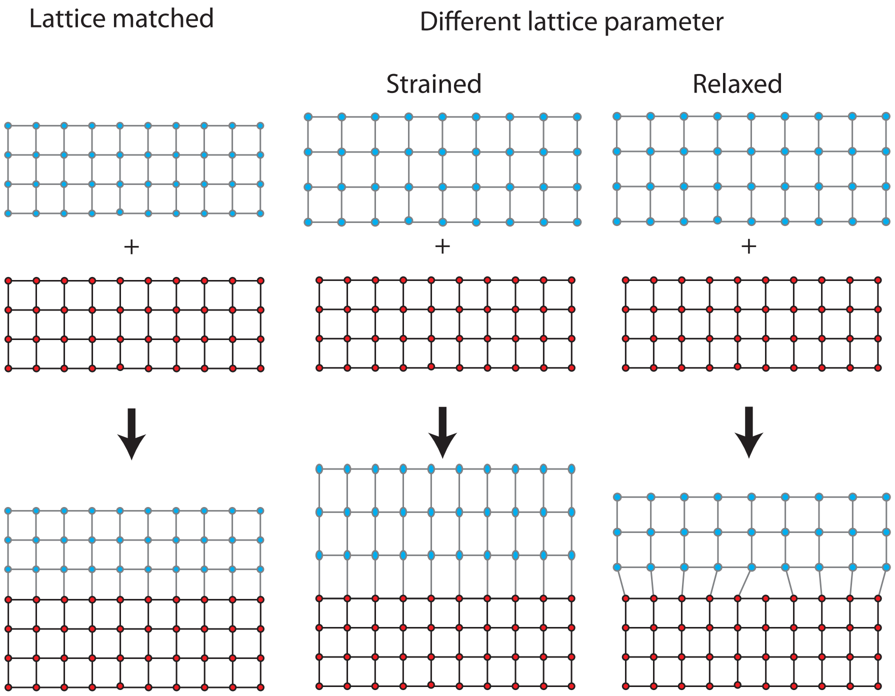

Figure 1.5: Schematic representation of heteroepitaxial layers.

substrates, especially sapphire and Si, are very common and more relevant for most industrial applications. Nowadays, the most commonly used substrate is sapphire, due to its low price, high availability, and compatibility with GaN, although its thermal conductivity, as well as its lattice mismatch to GaN, are less optimal. Silicon, being by far the most mature substrate, is available with a ultra high purity and crystalline quality and in much larger diameters. As its price is the most competitive and its processing the most developed, several groups are actively working on reducing or circumventing the drawbacks of its use as a substrate. Indeed, GaN on Si is highly strained and the difference in thermal expansion coefficients can lead to cracks. In this work, only sapphire and bulk GaN (in the following called free standing GaN (FS GaN)) are used as substrates.

1.2.1 Epitaxy: the different growth modes

For crystal growth in general, there are different possible growth modes. On a flat and defect free surface, depending on the wetting behavior, *i.e* if the surface free-energy of the growing film is lower than that of the substrate, two dimensional (2D) islands nucleate. In this smooth layer-by-layer growth mode - called Van der Merwe growth mode [37] - each monolayer is completed; the second layer only starts once all the vacant atom site positions are filled. Opposite to this 2D growth is a three dimensional (3D) growth, called Volmer-Weber growth mode [38]. A naive view is that the space between the initial islands is not filled up and new islands nucleate on top of the existing ones. A third intermediate growth mode is called Stranski-Krastanow growth mode [39, 40]. it starts with a 2D growth and - e.g. due to strain

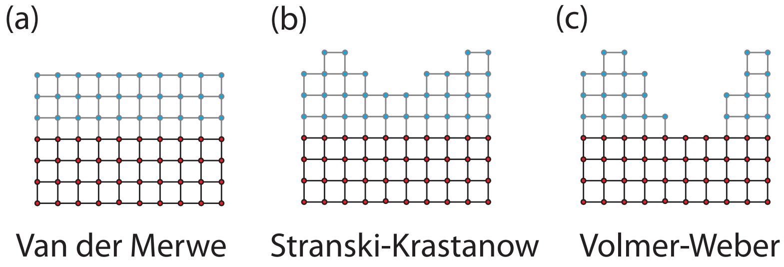

Figure 1.6: Schematic representations of the different growth modes: (a) Van der Merwe, (b) Stranski-Krastanow and (c) Volmer-Weber.

- continues with a 3D growth. A schematic representation of these three growth modes is displayed in Fig. 1.6. One thing to note is that the distance between the (initial) nucleated island will depend on the growth conditions (mainly the diffusion length), as well as on the growth rate (V_{gr}), as it affects the mean free path that particles have on the surface.

On vicinal offcut surfaces, either intentionally or originating from interaction with defects, the nucleation is affected. Burton, Cabrera and Frank showed that under these conditions, the nucleation preferentially takes place at the step-edges [41]. This growth mode is called step-flow growth mode and will be discussed in more depth the beginning of chapter 2. It should be pointed out that the step-flow growth mode is a kind of one dimensional (1D) growth due to lateral growth of the step-edges. Furthermore, it should also be mentioned that this growth mode is only valid for a sufficient diffusion length: for all adatoms to reach the step-edges, their diffusion length should be at least half the step width. When the diffusion length is reduced, the nucleation at the step-edges is accompanied by a nucleation on the steps, leading to a transition to a 2D nucleation.

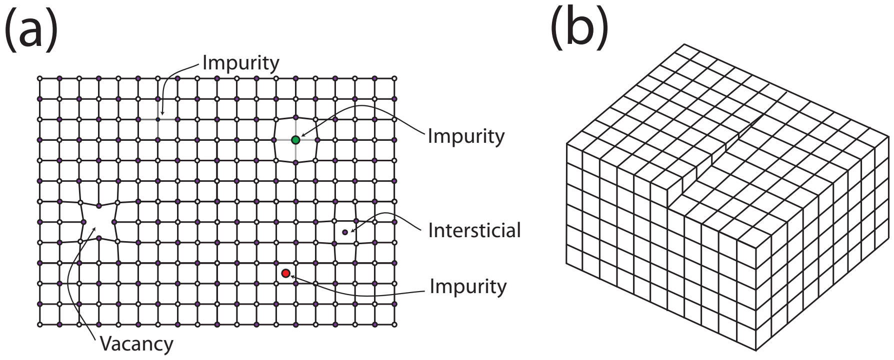

Figure 1.7: Schematic representation of (a) the different types of point defects (vacancies, interstitials and foreign atoms (impurities)), and (b) a screw dislocation.

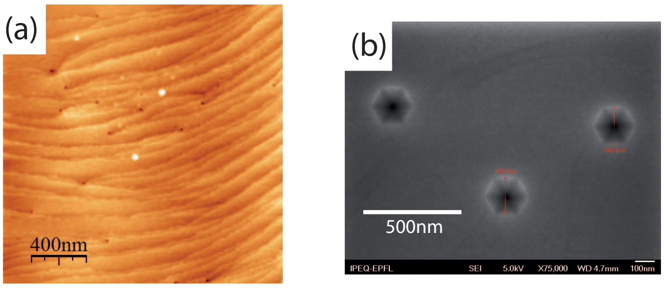

Figure 1.8: (a) 2 x 2 μm^2 AFM image and (b) SEM image (top view) of the surface of a GaN layer, displaying typical defects. In (a) dislocations are visible as black spots, while in (b) V-pits with well-resolved facets are observed.

1.2.2 Point defects and dislocations

In most cases, the crystal is locally disturbed by defects, from zero dimensional (0D) defects to 3D ones:

0D defects, the so-called point defects, represent defects of single atoms in the crystal lattice. This can be either a missing atom, called a vacancy, or an atom sitting between the normal lattice sites, called an interstitial, or a replacement of an atom with a different type, called an impurity (substitutional); impurities can also be on interstitial positions. If an impurity is introduced deliberately, it is called a dopant. Usually Si is used as a dopant to achieve *n*-type conductivity, while magnesium (Mg) is used to for hole conductivity [7]. The different types of point defects are schematically displayed in Fig. 1.7 (a). Note that it is very difficult to directly access their density. Two techniques, namely positron annihilation spectroscopy (PAS) and optical detected magnetic resonance (ODMR) can measure some kind of point defects (negatively charged ones for PAS and magnetic ones for ODMR). Otherwise, only indirect measurements are possible when the point defect density is low. For higher densities of impurities, tools like secondary ion mass spectroscopy can also be used.

1D defects refer to crystallographic defects such as screw, edge or mixed dislocations (a combination of both). Screw dislocations - schematically displayed in Fig. 1.7 (b) - are dislocations with an upwards pointing burger vector [42, 43]. They can pin steps and lead to the appearance of a growth spiral, as first described by Frank *et al.* [43]. Such a spiral is often observed in III-nitrides layers [44], as their screw-type dislocation density is usually very high.

Stacking faults or stack order faults are 2D defect types. They can be observed by transmission electron microscopy (TEM) or high resolution TEM (HR-TEM). This kind of defect does not play a major role for *c*-plane GaN but impacts the growth morphology of *m*-plane surfaces. For more information the reader is referred to [45].

The last major type of defects are 3D defects, such as V-pits [46] or trenches [47]. These macro defects can be seen by atomic force microscopy (AFM) or scanning electron microscopy (SEM), as exemplified in Fig. 1.8. They are not strictly seen intrinsic defects as the are generally induced by threading dislocations. The center of the pit is usually a threading dislocation and its sidewalls are well-defined facets [46]. Such defects play no further role in the presented investigations, but it was proposed that the different facets of such a V-pit could affect the device structure grown on top (resulting in thinner layers on the sides of the pit) [46].

In general, crystal defects can be non-radiative recombination centers. While the relative defect-insensitivity (compared to other semiconductors) of InGaN-based devices is still a major question, defects still play an important role. Their number needs to be minimized to achieve the best device performance, although it was proposed that some kind of topological defects could help by screening non-radiative recombination centers [46]. As a consequence, high performance devices, such as LDs, are normally grown on FS GaN substrates with a low dislocation density ($< 10^7 \mathrm{cm}^{-2}$).

1.2.3 Alloy disorder

One important point to mention here is the homogeneity of a ternary alloy. The distribution of the different atoms in the alloy leads to statistical fluctuations. In addition, for the case of InGaN, miscibility gap is often mentioned as a source of problems [48]. Instead of a homogeneous indium distribution, composition fluctuations are often observed in InGaN alloys. The formation of InN-rich clusters observed in InGaN LEDs was proposed by O'Donnell *et al.* to be responsible for the high efficiency of the LEDs [49]. Indeed, 3D atom probe maps of the indium distribution in *c*-plane InGaN quantum wells have confirmed such fluctuations over a large composition range [50, 51, 52]. Fluctuations were also observed by HR-TEM and well-separated sharp emission lines appear in micro photoluminescence spectra [53], indicating different emission centers, in agreement with the carrier localization in potential fluctuations. Furthermore, it was recently discussed that local variation in the surface morphology can affect the local indium incorporation as well [54].

Together, these effects indicate that the indium distribution in a ternary alloy can not be assumed to be homogeneous, but should often exhibit local variations and indium-rich clusters. Note that holes could be bound to local In-N-In chain structures [55].

1.2.4 Interfaces, heterostructures and their applications

Heterostructures exhibit interfaces and their properties strongly affect the whole structure. InGaN LEDs and LDs are based on a sandwich-type structure made of GaN/InGaN/GaN layers, where the difference in bandgap creates a quantum well (QW) structure, the so-called InGaN QW. The smaller bandgap of the InGaN layer leads to a trapping of the holes and electrons from the valence and conduction band, respectively; the recombination of the excitons (electron-hole pairs) takes place in the InGaN QWs, as schematically displayed in Fig. 1.9 (a). The confinement leads to the quantification of the energy states in the QW. Usually the recombination occurs between the ground state in the QW conduction band and the heavy hole in the valence band. As changing the QW thickness affects this confinement,

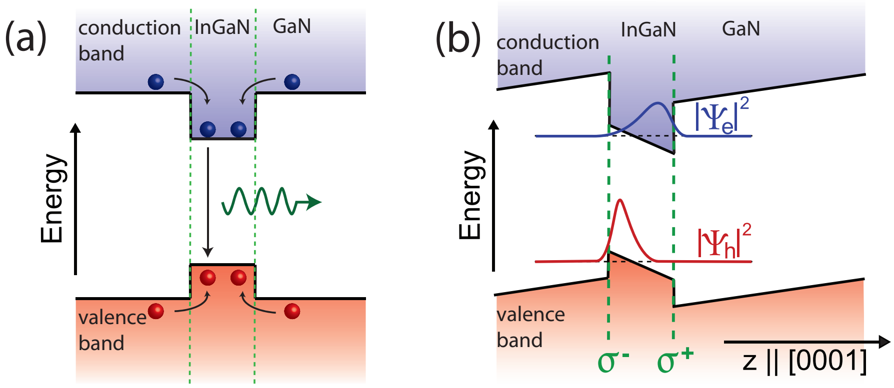

Figure 1.9: Schematics of a single InGaN quantum well structure (a) without and (b) with of the effect of the internal electric field.

the emission wavelength changes. On the other side, the above mentioned piezoelectric and spontaneous polarizations are important for polar structures. Indeed, the polarization discontinuity at the interfaces leads to building of surface charges, which create an electric field in the QWs. This results in a band-bending, which is thickness dependent and leads to a red-shift of the emission wavelength, but also to a strong reduction in the overlap of the electron and hole wavefunctions (see Fig. 1.9 (b)). The reduced overlap strongly lowers the radiative-recombination probability and thus strongly affects the efficiency. While the red-shift allows one to reach longer wavelength with a lower indium content, the reduced efficiency is detrimental to device performance. For efficient polar devices, only thin QWs should thus be used.

Another important characteristic of interfaces is their morphology, *i.e.* “rough” or “smooth”, “sharp” or “graded”. It is worth to mention that qualifying an interface as “smooth” or “rough” depends on the length-scale of the observation: an interface can be rough on a large scale while simultaneously smooth on a small scale. The definition of “rough” interfaces is actually quite complex. It also depends on the exciton Bohr radius and wavelength extension [56]. In fact, smooth interfaces and indium composition homogeneity are especially important for LDs to avoid gain dilution. However, QW thickness variations can have other implications: while it was proposed that holes could be localized on In-N-In bounds, it was also pointed out that electrons could be localized due to QW thickness variations (in thicker areas) [55]. Such phenomena have been proposed as the main mechanism responsible for the high efficiency of LEDs despite the large defect density.

1.3 Experimental techniques

III-nitride based heterostructures are commonly grown by two main epitaxial growth techniques. Metal organic vapor phase epitaxy (MOVPE) is used both in research and industry, as it allows a reliable fabrication of high efficiency optoelectronic devices. The second technique, molecular beam epitaxy (MBE), is mainly used for research. Optoelectronic devices fabricated by MBE have not reached the performance demonstrated by their MOVPE counterparts yet. However, promising results have been published recently [57, 58]. Other techniques are used to grow III-nitrides, notably hydride vapor phase epitaxy (HVPE), which is commonly used to make bulk layers, but also sputtering or bulk crystal growth techniques (e.g. ammonothermal growth [59]). These techniques will not be treated here, as all the layers or devices presented in the thesis were fabricated by MOVPE or MBE.

1.3.1 Metal organic vapor phase epitaxy

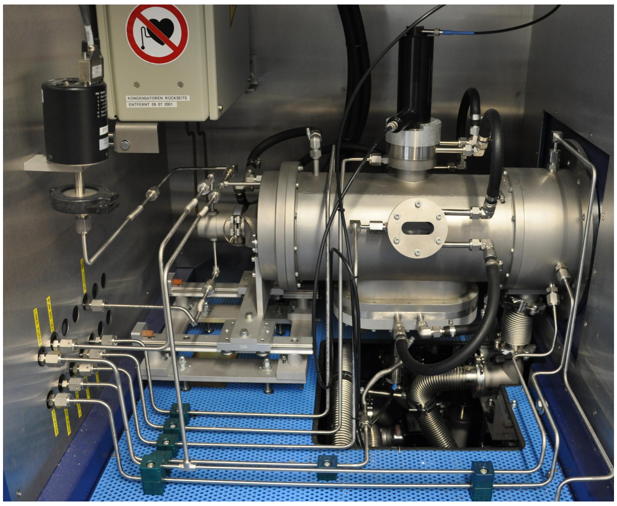

Figure 1.10: Photo of the horizontal Aixtron 200 MOVPE reactor used in this work.

MOVPE is the tool of choice for the production of nitride based devices. The horizontal Aixtron reactor, displayed in Fig. 1.10, was used for most investigated samples. It allows growth of one 2" wafer at a time. While enough for research, larger production reactors can handle over 90 x 2" wafers at a time.

MOVPE is a chemical vapor deposition process (frequently called metal organic chemical vapor deposition (MOCVD) too). Gases are injected into the reactor, where the deposition takes place on a heated substrate. Two kinds of gases are used: i) carrier gases to transport the reaction gases to the reaction zone and provide the environment (e.g. pressure) in the reactor. Usually, hydrogen (H_2), nitrogen (N_2) or a mixture of both is used; ii) the reaction gases or reagents, which can be divided into two groups: ammonia (NH_3) decomposes at the growth front to provide nitrogen, and group-III elements are supplied in form of metalorganics. Trimethylindium (TMIn - $In(CH_3)_3$) for indium, trimethylaluminum (TMAl - $Al(CH_3)_3$) for aluminum and for gallium either trimethylgallium (TMGa - $Ga(CH_3)_3$) or triethylgallium (TEGa - $Ga(C_2H_5)_3$) are used. Dopants or other group-III elements are provided similarly. Those metalorganics are transported with the carrier gases into the reaction chamber. To make it simple, there are three different zones in the reaction chamber: the area far away from the crystal surface, the surface of the crystal and a boundary region where reactions and mass-transport of the reagents plays an important role, as schematically displayed in Fig. 1.11.

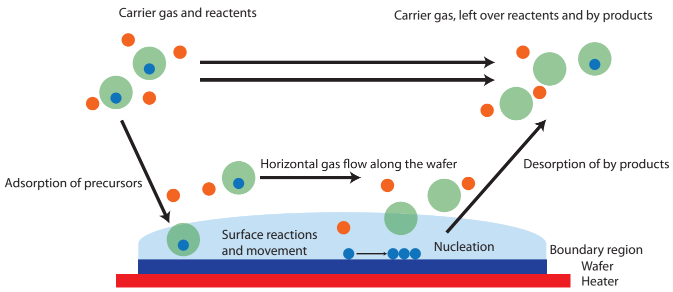

Figure 1.11: Schematic representation of the effects that play a role at the growth front for MOVPE, with a focus on gas reactions.

Table 1.3: standard MOVPE growth conditions used in this work.

Layer	T_{gr}	Carrier gas	Metalorganic(s)	V/III ratio
Buffer layer	1050° C	H_2	TMGa	560
LT GaN	840° C	N_2	TEGa	4400
QW	between 725° C and 840° C	N_2	TEGa and TMIn	1170-7531

The standard MOVPE growth conditions that will be used for this work are presented in Tab. 1.3; if a layer is grown under different parameters, the changes will be mentioned in the text. Note that below each investigated layer or structure, grown on FS GaN or on sapphire, a GaN buffer layer of at least one micron thickness is deposited. The low temperature (LT) GaN studied in the second chapter is grown under barrier conditions with nitrogen. Indeed, hydrogen must be discarded to achieve high In content InGaN alloys.

1.3.2 Molecular beam epitaxy

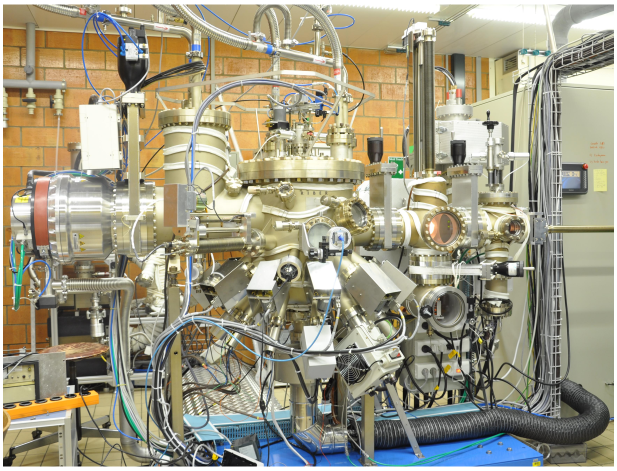

Figure 1.12: Photo of the Riber compact 21 MBE reactor used in this work.

MBE is a physical deposition process that takes place in ultra-high vacuum, which is suitable

Table 1.4: Standard MBE growth conditions used in the work.

Layer	T_{gr}	N source	Flux	Mode
Buffer layer	800° C	NH_3	100 sccm	N-rich
HT PAMBE GaN	790° C	N-plasma	≈1 sccm (400W)	N-rich
InGaN QW	550° C	NH_3	490 sccm	N-limited
InGaN QW	550° C	NH_3 + N-plasma	300 sccm + 1 sccm (360W)	N-rich

to avoid impurity incorporation. Molecular beams of group-III elements and dopants are shot from Knudsen cells towards the substrate heated at the growth temperature (T_{gr}). Two nitrogen sources are commonly used: ammonia (NH_3-MBE), or, alternatively, a radio-frequency plasma that cracks nitrogen molecules (N_2) directly. The latter is called plasma-assisted MBE (PAMBE). The MBE system used in this study is a Riber compact 21, equipped with both nitrogen sources, NH_3 and N-plasma (Fig. 1.12). A schematic of an MBE system is displayed in Fig. 1.13. As for MOVPE, *in situ* laser reflectivity is used routinely to monitor in real-time the growth rate of the layers. Additionally, the ultra high vacuum environment allows the use of both reflection high-energy electron diffraction (RHEED) and quadrupole mass spectroscopy (QMS). These techniques will be described in the following part.

The different nitrogen sources have implications on the growth. First, while NH_3-MBE implies nitrogen-rich conditions, the standard conditions for PAMBE are metal-rich. In fact, PAMBE usually requires a bilayer of metal at the growth front to achieve 2D *c*-plane GaN layers [60]. Second, the growth rate is higher for NH_3-MBE than for PAMBE (about 1 μm/h compared to about 0.3 μm/h). Third, the cracking of NH_3 provides hydrogen for NH_3-MBE growth (NH_3 is split into (active) nitrogen and hydrogen), which can help with defect passivation [61]. Fourth, NH_3-MBE allows to grow good *p*-type layers at relatively low growth temperature [62, 63]. The standard growth conditions used for MBE samples in this work are presented in Tab 1.4; deviations from these parameters will be mentioned in the text.

One thing to note is that although MBE is very common in the classical III-V semiconductor technology, it is less used for the III-nitrides, which are mainly grown by MOVPE. There are different key features between MOVPE and MBE, but pressure should be especially mentioned here as it directly affects the net desorption rate of the materials. This is especially true for In.

1.3.3 *In situ* characterization tools

Three *in situ* tools have been used to investigate growing layers: reflectivity, RHEED and QMS. Because it relies on the reflection of a laser beam, reflectivity can be easily implemented in both MOVPE and MBE. The interference of the reflections from the different interfaces (the top surface and e.g. the sapphire-GaN interface) leads to oscillations of the laser intensity, as it depends on the optical path difference. As an example, a typical reflectivity measurement recorded during MBE growth of GaN is presented in Fig. 1.14. With the red laser used in the MBE setup, one period corresponds to 142 nm of GaN growth, and a growth rate of about 585

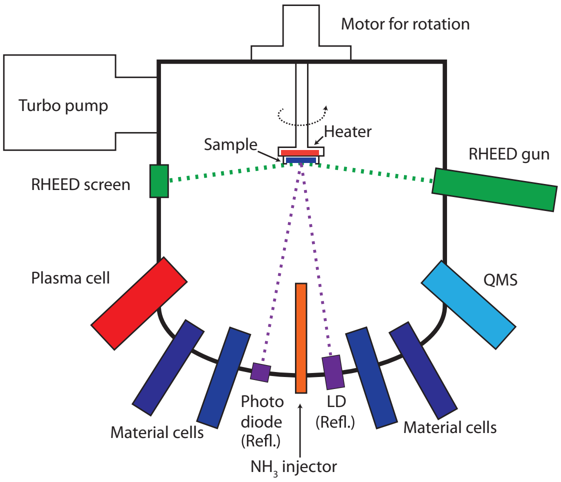

Figure 1.13: Schematic representation of a MBE reactor.

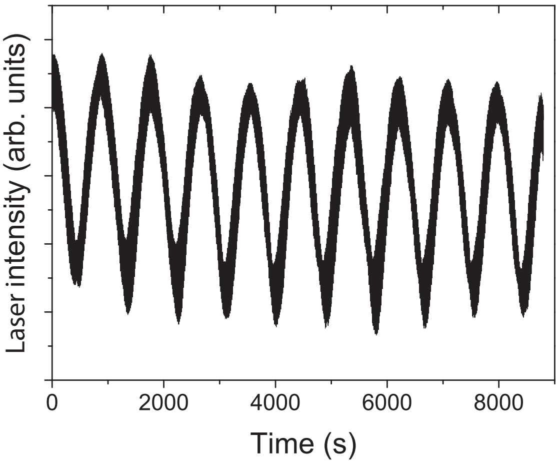

Figure 1.14: Reflectivity measurements during MBE growth of GaN. One oscillation corresponds to a layer thickness of 142 nm.

nm/h is obtained from Fig. 1.14. This means that this technique is very useful to measure the thickness of thick layers, but can not be properly applied for thin layers. Nevertheless, it is the standard tool to measure *in situ* the growth rate for MOVPE and NH_3-MBE.

The second *in situ* tool is RHEED. The setup consists of an electron gun and a fluorescence screen. The electrons from the source hit the sample surface at a grazing incidence angle, where they are diffracted and reflected. As it is based on an electron beam, RHEED requires high vacuum and therefore can not be used in an MOVPE environment. It is a very useful tool for MBE, as it allows information about the growth mode, relaxation, growth rate, and alloy composition. The RHEED pattern itself indicates if the growth is 2D (smooth streaks) or 3D (spotty pattern), as displayed in Fig. 1.15. Measuring the evolution of the intensity of the specular beam over time allows one to determine the growth rate very precisely. Oscillations reveal a layer-by-layer growth mode, where each maximum corresponds to a complete monolayer

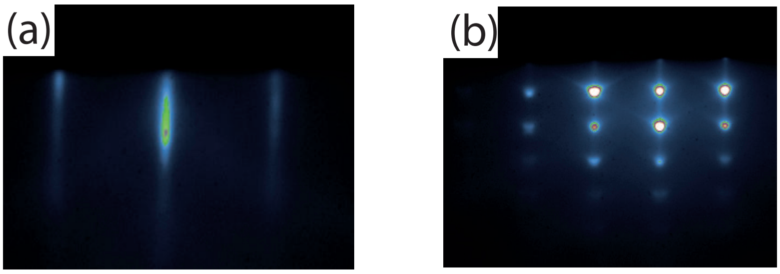

Figure 1.15: RHEED patterns of a GaN layer grown at 800°C. (a) streaks indicate smooth 2D growth, and (b) a spotty pattern indicates 3D growth.

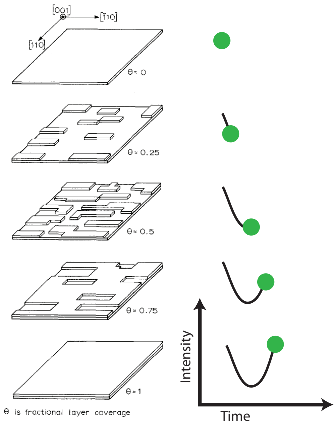

Figure 1.16: Schematic representation of RHEED specular beam intensity oscillation principle: The intensity of the reflected beam depends on the smoothness of the layer; it is maximal for complete layers and minimal for half coverage. The diagram has been adapted from Neave *et al.* [64].

(ML) [64], as schematically displayed in Fig. 1.16. Typical RHEED oscillations recorded for GaN are displayed in Fig. 1.17. This can be used to control the thickness of a thin layer with a very high precision. For ternary alloys, it is also possible to extract the alloy composition by comparing V_{gr} of one of the two binary compounds to the one of the ternary, while keeping the same individual metal fluxes. Note that this holds true as long as the sticking coefficient is 1.

A last *in situ* tool that also requires vacuum and is thus only used in MBE is QMS. While mass spectrometry is common to analyze the composition of a given material, it is useful to measure the background impurity levels in MBE. It can also probe the particles deflected or desorbed from the sample and will be used to study the growth window for In-rich InGaN in part 3.3.1.

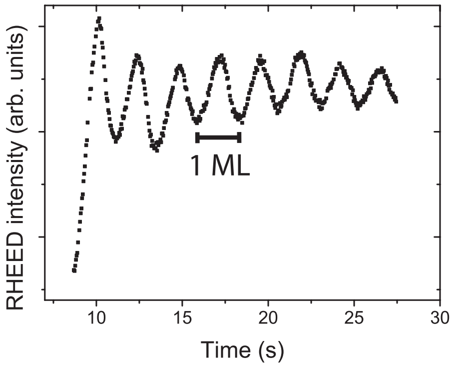

Figure 1.17: RHEED intensity oscillations for GaN. Each oscillation refers to one monolayer growth.

1.3.4 *Ex situ* characterization tools

Ex situ tools were used to study the surface morphology, and the structural and optical properties of the fabricated structures.

The surface morphology was investigated by AFM. For AFM measurements, an ultra-sharp tip is scanning the surface. Height changes are read out by position changes of a reflected laser spot. In this work, a Digital Instruments Nanoscope has been used in tapping mode, meaning the changes on the oscillation of the cantilever on which the tip is located are probed. Note that AFM is well known for its precise height measurements and allows to determine the root mean square (rms) surface roughness. Nevertheless, in the images shown in this work, a height bar is not displayed, as it is not necessary for the desired information (and keeping the same height scale even can be misleading in some cases). Instead, the displayed height range is adjusted to display the relevant surface morphology features.

The structural quality of the samples has been measured by X-ray diffraction (XRD), which also allows to extract the material composition, as well as its structural quality. In addition, XRD allows to measure the QW and barrier thickness. For more information about the XRD technique and its application to the III-nitrides, the reader is referred to the review by Moram *et al.* [65].

To investigate thin QWs in more detail, electron microscopy was carried out. SEM was available at the Institute, while HR-TEM was carried out by Francesco Ivaldi and Dr. Slawomir Kret of IFPAN, Warsaw (Poland) in the framework of the FP7 ITN Rainbow project. All HR-TEM images shown in this work are by their courtesy, unless noted otherwise. At IFPAN, a spherical aberration-corrected TEM (a FEI-titan) with a resolution down to 70 pm allowed both high-resolution images of the QW region as well as electron energy loss spectroscopy (EELS). The indium distribution in the QW, the QW interfaces and strain were then thoroughly investigated (see [66] for more details on the technique).

The structural information about the QWs might be particularly meaningful if cross-checked with their optical properties. Photoluminescence (PL) was used as the main tool to characterize

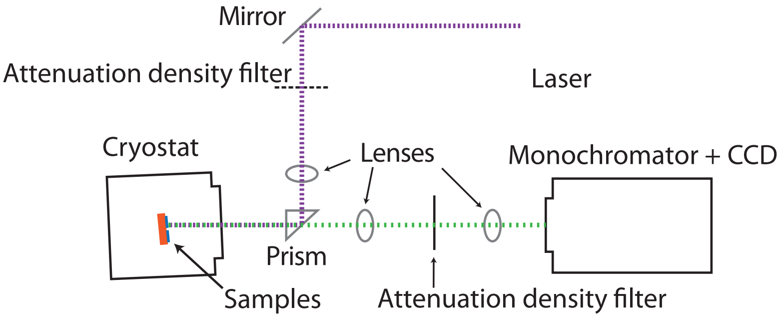

Figure 1.18: Schematic representation of the PL setup. Note that calibrated attenuation density filers on the detection side have been utilized to avoid saturating the charge-coupled device.

the emission from the QWs, while electroluminescence (EL) was used for LED characterization. A schematic representation of the PL setup is shown in Fig. 1.18. PL usually excites charge carriers in both the InGaN QW and the GaN barriers. It is also possible to probe only the QWs when the excitation energy is lower than the GaN bandgap. In the latter case, the absorption volume is limited to the QW and thus is very small. As a consequence, an excitation energy above the GaN bandgap is used throughout this work, unless specified otherwise. Different excitation powers have been utilized. This was achieved by either filters or for very high excitation power by the use of a microscope objective which allows to focus the beam-radius down to a less than 1 μm^2. This is the so-called micro-PL. In this work, temperature-dependent PL was carried out between 10 K and 300 K, as it allows to study the influence of non-radiative recombination centers. At RT, non-radiative channels play a major role, while at 10K, radiative recombination dominates. This is linked to the different lifetimes of the recombination processes. Time-resolved PL (TRPL) was also performed to gain additional information, using a frequency-doubled picosecond-pulsed Ti:sapphire laser with a pulse picker and a streak camera. These measurements were performed with Bernard Gil and Thierry Guillet in the Laboratoire Charles Coulomb in Montpellier. Note that apart from the TRPL, all presented measurements were performed with a continuous wave laser: most measurements were done with a HeCd laser emitting at 325 nm (with a low excitation power of about 2 mW). To excite below the GaN bandgap, a laser diode emitting at 375 nm was used, while a frequency-doubled Ar laser (emitting at 244 nm) was used in combination with a microscope objective for very high excitation power measurements (allowing power densities of over 10^5 W cm^{-2}). To gain more information about the lateral emission characteristics, fluorescence measurements were performed at RT.

2 The kinetic growth regime of GaN

GaN and other III-nitrides are commonly grown on vicinal surfaces, where steps-edges provide preferential nucleation sites. The growth parameters of GaN have been optimized to achieve step-flow growth growth mode, which leads to smooth surface morphologies. However, this growth mode may become unstable in the presence of an Ehrlich-Schwöbel barrier (ESB). Especially under *out of equilibrium* conditions, which is usually the case for the active region of the devices (e.g. for indium-rich InGaN layers and the barriers surrounding them), kinetic effects govern the growth morphology. This may lead to various surface morphologies which can strongly affect the light emission characteristic of the devices.

In this chapter, the theory of the ESB and its effect on the surface morphology is presented first. Based on other materials systems, it is adapted to the nitride materials. Then, the surface features observed for GaN grown under kinetic conditions by both MOVPE and MBE will be described and correlated to an uphill masscurrent induced by the ESB. After discussing the origin of the surface morphology features, the parameters that control the surface kinetics are investigated. Finally, the effect of the surface morphology on device performance will be analyzed.

2.1 The classical step flow growth mode

The growth on vicinal offcut surfaces was first described by Burton, Cabrera and Frank in the 50's [41]. First, the terms that will be used more in the following are briefly defined, as different authors use them differently (and the one adapted here is different from the terrace-step-kink terminology used by Burton *et al.* [41]): a step (or terrace) is the flat surface part of a staircase morphology (on vicinal offcut surface); the edge between two steps is called step-edge (Burton *et al.* calls this the step). Along a step-edge a kink can be found. An overview of the surface processes at the growth front is displayed in Fig. 2.1. Instead of completing a full layer, a preferred nucleation takes place at the step-edges. To be more precise, particles adsorbed on the surface (A) diffuse on the steps (B) and attach to the step-edges (C). There, they may diffuse along the step-edge (D) and incorporate at a kink (E). In this process, the step-edges grow

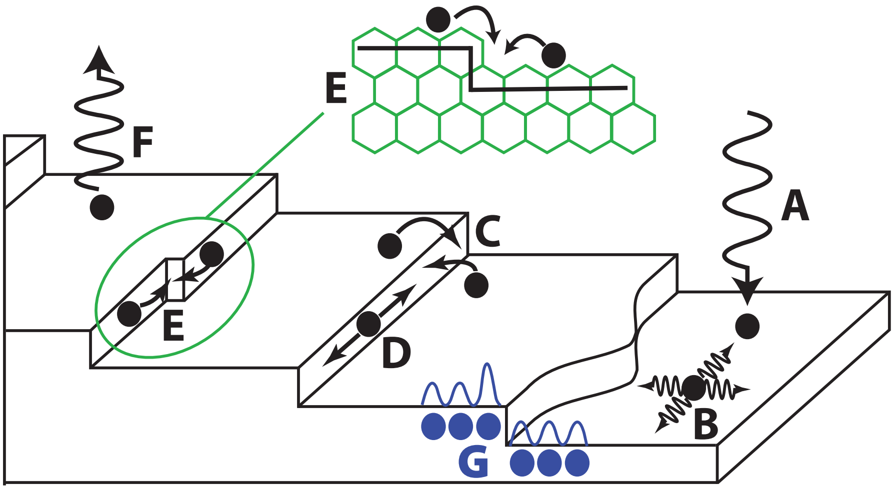

Figure 2.1: Processes at the growth front with adsorption (A), diffusion on a step (B), attachment to a step-edge (C), diffusion along the step-edge (D), attachment to a kink on the step-edge (E) and desorption (F). (G) displays the asymmetric barrier at the step-edge.

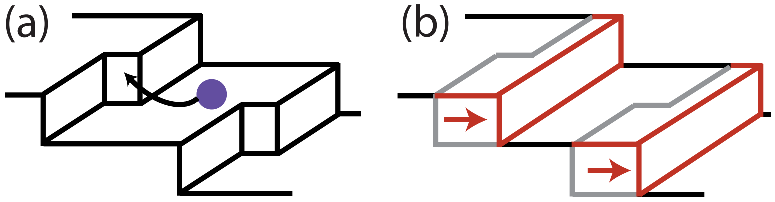

Figure 2.2: Step flow growth mode with (a) incorporation at step-edges and kinks, which lead to (b) a smooth growth which conserves the staircase step morphology.

outwards, leading to the formation of a smooth layer while conserving the step-morphology, as schematically described in Fig. 2.2. For this growth mode, the diffusion length necessary for all particles to reach the step-edges is half the step width (when no ESB is present). Fig. 2.3 shows the typical surface of GaN grown in this step-flow mode. GaN layers deposited by MOVPE above 1000°C with H_2 as carrier gas usually exhibit a staircase morphology that is typical for step-flow growth. The offcut angle of both substrates used in this work is between 0.3° - 0.6° towards *a* or *m* direction. In Fig. 2.3, the influence of the substrate (FS GaN *vs* sapphire), and hence the effect of dislocations on the growth mode, is compared. The surface morphology of the high temperature (HT) GaN grown on FS GaN is much more homogeneous and regular than for the sample grown on sapphire, where the steps are more disordered. This is a consequence of a higher dislocation density. Regarding the offcut angle and direction, it should be mentioned that for the FS GaN substrate, the offcut was prepared on purpose *ex situ* by surface polishing. It is thus homogeneous and well-oriented along a certain direction. This produces a well ordered surface with constant step-edge spacing (Fig. 2.3 (a) and (b)). On the other hand, GaN grown on sapphire exhibit a similar but less regular staircase morphology (Fig. 2.3 (c) and (d)).

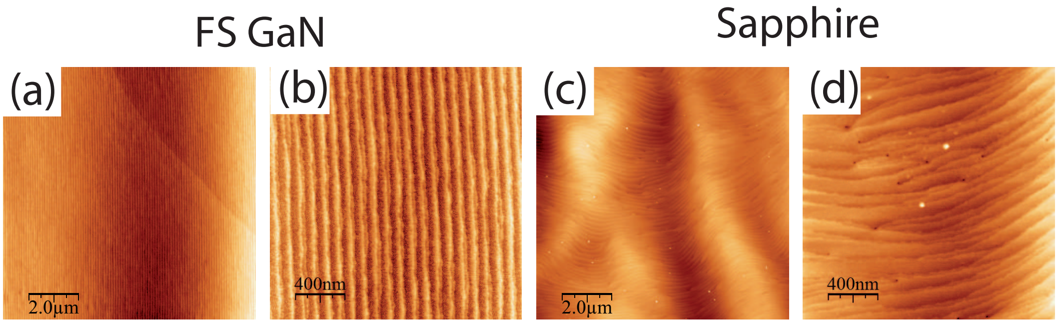

Figure 2.3: 10 x 10 and 2 x 2 μm^2 AFM images of normal HT GaN grown on (a)-(b) FS GaN and (c)-(d) sapphire.

The role of the dislocations on the step-flow mode needs to be discussed in more detail. Indeed, as Frank suggested [43], a pinned step will form when a threading dislocation with a screw component intersects the surface: the pinning of the step causes a surface displacement equal to the Burger vector normal to the surface, which manifests in steps connecting two dislocations of opposite sign. Thus, dislocation pinning affects the evolution of the steps during growth. One of the effects can be the emergence of spiral growth. When the radius of the curvature of the pinned step is small, a spiral can wind up around the screw dislocation [43]. Both, spirals and pinned steps can be observed in GaN grown on sapphire [44]. Because of their very low dislocation density ($< 10^7$ cm^{-2}) FS GaN substrates are good candidates to obtain surface morphologies free of dislocation pinning.

2.2 The Ehrlich-Schwöbel barrier

In this part, the theoretical impact of a step-edge barrier energy asymmetry on the growth modes is reviewed and its effect on the micro- and macrostructure of a crystal discussed. As only the details relevant for interpreting the following investigation of GaN are treated in detail, the reader is referred to the review of Misbah *et al.* (Crystal surfaces in and out of equilibrium: A modern view) [67] for a more general overview about growth theory.

2.2.1 Basics of the Ehrlich-Schwöbel barrier and its impact on the surface morphology

In the description of the classical step-flow growth mode, it is assumed that the growth rate of each step-edge is identical and that the probabilities of attachment to a step-edge from the upper or the lower step are equal. However, this classical model needs to be modified to account for an asymmetric probability of attachment from the upper with respect to the lower step. This is the so-called Ehrlich-Schwöbel barrier (ES barrier or ESB) or step-edge barrier. This asymmetry was first observed by Ehrlich and Hudda for tungsten [68] and theoretically treated by Schwöbel and Shipsey in 1966 [69].

From a microscopic point of view, the ESB corresponds to the case of adatoms, that arrive at a step-edge from the upper step, have to overcome a barrier to attach to the step-edge, as schematically presented in Fig. 2.4. Ehrlich and Hudda observed that atoms were preferentially reflected back on a (downwards) step-edge and explained this by a decrease in binding energy originating from reduced neighbor atoms at the step-edge [68]. A similar model was described by Schwöbel and Shipsey at the same time [69, 70]. This situation is of course different for adatoms arriving to the step-edge from the lower step. Thus the probability of attachment is asymmetric. In general, the ESB can be referred to this kind of asymmetry, and since the configuration of the dangling bonds should also play a role, its strength should depend on the crystallographic orientation. This asymmetry should exist for most materials systems, but should impact the growth only if the barrier height is large enough to create a profound asymmetry in the attachment probability. This of course should depend on the strength of the ESB and the growth conditions used, as for very high T_{gr} adatoms can have enough energy to easily pass over the ESB. There are thus two factors that should be taken into account: the ESB itself (meaning the different probability of attachment), and the growth conditions.

From a macroscopic point of view, the presence of an ESB has a major impact on the growth regimes and the observed morphologies. At elevated temperatures (as used for the GaN layer displayed in Fig. 2.3), the relative strength of the ESB is weak compared to the energy of the adatoms and one does therefore not expect nor observe a strong impact of the ESB. However, while its effects can be avoided at high temperatures, most materials systems are affected by the ESB effects when they are grown at lower temperatures. This needs to be explained in more detail:

Per se, the presence of an ESB changes the conditions of the step-flow regime. Assuming a high ESB for which the probability of attachment from the upper step can be neglected, the diffusion length needed for all adsorbed adatoms to reach a step-edge is the step width. Without an ESB the necessary diffusion length is half the step width (and for a non-infinitely high ESB, this statistical value lays between the two extrema). This means that the change from a 1D nucleation (step-flow growth) to a 2D one (e.g. layer-by-layer or island growth) happens at a higher diffusion length over step width ratio in the presence of an ESB, as schematically displayed in Fig. 2.5.

This is however only a partial view of the effect of the ESB on the surface morphology and on the growth mode. The major effect is this: the presence of an ESB makes the growth unstable against any kind of (temporary/local) perturbation [67]. Local variations enhance themselves and get stabilized, which leads to a modification of the starting surface. The growth mode becomes unstable and macroscopic surface features appear. There are three types of ESB-induced surface morphologies that have been observed in other materials systems during homoepitaxy: hillocks, fingers (or step-meandering), and step-bunching [67].

The case of the hillocks was first described by Villain [71], who argued that the growth morphology becomes unstable with an ESB. Hillock growth takes place for flat surfaces or surfaces

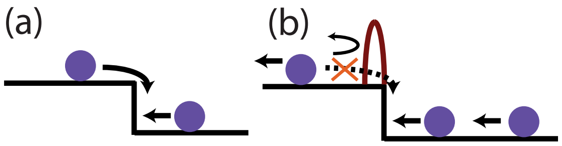

Figure 2.4: Attachment to step-edges (a) without and (b) with an ESB.

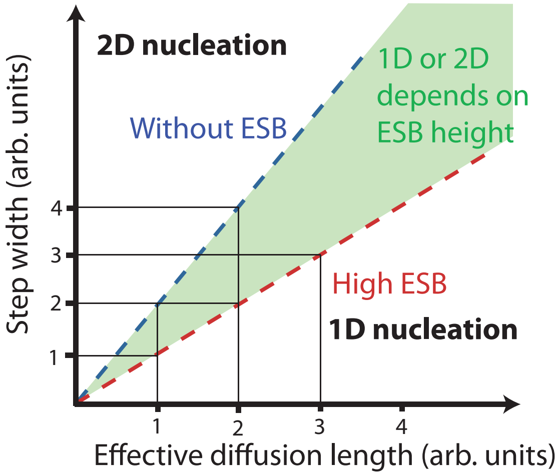

Figure 2.5: The effect of the ESB on the 1D to 2D growth mode transition is displayed in the diffusion length over step-width plot.

with a low offcut angle. As displayed schematically in Fig. 2.6, 2D island nucleate first due to random fluctuations. When an ESB is present, the material is incorporated on the upper step-edge, which has two implications: first, the islands grow outwards until a new nucleation can take place on top. When this happens, the newly nucleated islands then grow outwards again until a new island can nucleate on top (and this process continues). Second, as no down-diffusion takes place, only the material that arrives between the islands can feed the lowest step-edge and only the material that arrives on a step can grow the step-edge above. As a consequence, closing the gap between islands and completing a layer is difficult, so layer-by-layer growth can no longer be maintained. Instead, islands appear: as the amount of material arriving to a step-edge depends on the size the step below, the width of a step is not necessary maintained during growth. In fact, larger steps lead to faster lateral growth rates of the upper step-edge and thus shrink if the step below is smaller. At the same time, the width of the step above is increased. As the lowest steps are limited strongly in size (due to having only

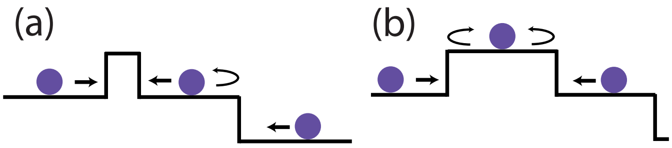

Figure 2.6: (a) A small island acts as nucleation core which (b) evolves by attachment from the lower steps until a new nucleation takes place on the top.

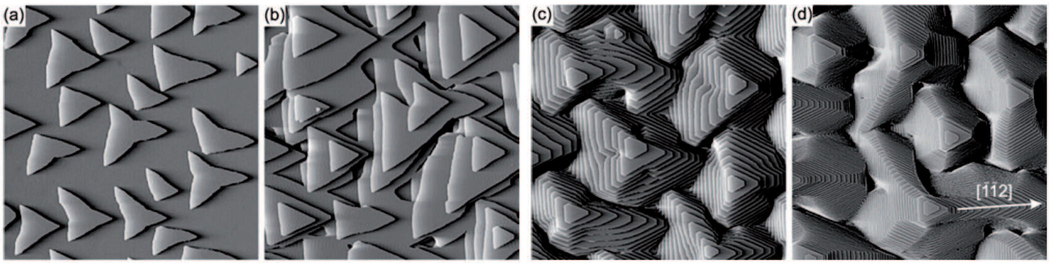

Figure 2.7: STM images of the early growth stages of Pt(111), taken from Krug [76].

a small amount of material), the outwards (i.e. lower) steps shrink and the ones on top grow during the layer growth. Thus the step size and the growth rate of the step-edge are transfered upwards. This process was interpreted by Villain as an uphill masscurrent [71]. Effectively, the lower and more outwards steps grow slower, causing the hill to grow [67, 71, 72, 73]. As a result, it leads to the formation of a landscape of self-assembled islands, where the distance between the islands is related to the effective diffusion length. Such a morphology is likely to be found on flat surfaces. It can also appear for rather large steps (low offcut), where the presence of an ESB shifts the 1D to 2D transition (see Fig. 2.5), thus enabling island nucleation and subsequently hillock formation, as described above. This kind of morphology can be observed for many materials systems, e.g. for low temperature Ge [74] or Si [75]. An example of such a morphology is given in Fig. 2.7, which displays scanning tunneling microscopy (STM) scans of Pt(111) [76].

It should be pointed out here that in a real system, eventually a layer will coalesce where the most outwards steps of the islands meet. However, as the downwards diffusion is limited, it is possible that defects may form at these borders due to diffusion issues. Furthermore, another point to consider is faceting, which has been neglected so far. It is possible that the downwards diffusion could be changed when a certain facet is reached at the edge of the islands. Such a facet could potentially stabilize or even lead to a different incorporation (e.g. of impurities).

To understand the hillock formation in more detail, and to distinguish the other ESB-induced morphologies, the formalism from Krug is introduced [76]. Following his notations, the net masscurrent is defined as $\mathbf{j}(\nabla h)$, with ∇h the local slope. Assuming that $\mathbf{j}(\nabla h)$ is isotropic in the reference plane, the current can be expressed as

$$\mathbf{j}(\nabla h) = f(|\nabla h|^2)\nabla h. \tag{2.1}$$

If f > 0, the current points uphill. The average height is deposited at growth rate $\mathbf{F}$; the current $\mathbf{j}$ modulates the growth surface without changing the volume of the layer, redistributing the mass. This implies a conservation type of the continuum equation:

$$\frac{\partial h}{\partial t} = -\nabla \cdot \mathbf{j} + \mathbf{F} \tag{2.2}$$

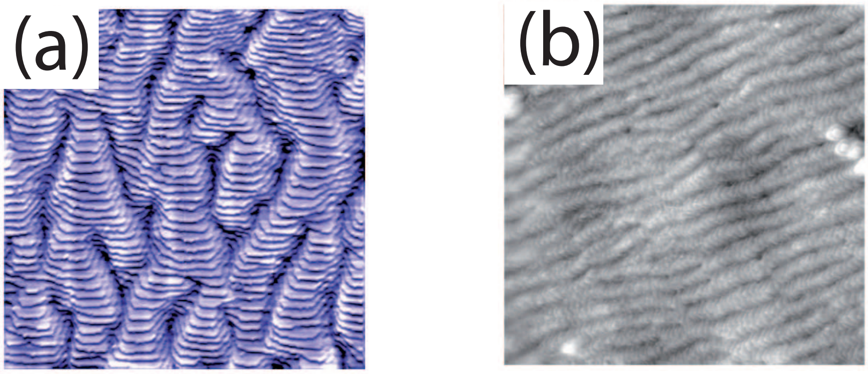

Figure 2.8: STM images of step-meandering on (a) Cu(1,1,17) and (b) Cu(0,2,24) surfaces, taken from Maroutian *et al.* [77].

Assuming a flat surface, the ansatz $h(\mathbf{r},t) = \mathbf{F}t + \epsilon(\mathbf{r},t)$ gives

$$\frac{\partial \epsilon}{\partial t} = -f(0)\nabla^2 \epsilon, \tag{2.3}$$

with $-f(0)$ the diffusion coefficient. The partial differential equation can be solved by a Fourier transformation. Putting a perturbation of wavevector $\mathbf{q}$, given by

$$\epsilon(\mathbf{r},t) = \epsilon_0 \exp^{i\mathbf{q}\cdot\mathbf{r}+\omega(\mathbf{q}t)} \tag{2.4}$$

into Eq. 2.3 yields the growth rate of the perturbation $\omega(\mathbf{q}) = f(0)\left|\mathbf{q}\right|^2$. This indicates that the flat morphology is unstable, as the perturbation grows when $f(0) > 0$. In turn, this shows that an uphill current, caused by the ESB, induces the formation of mounds on the growing surface. More detailed information on the background and the mathematical treatment can be found in the reviews from Misbah *et al.* [67] or Politi *et al.* [73], or in the book chapter from Krug [76].

Considering a vicinal surface, not only hillocks or mounds can be observed for low offcut angles, but also a finger-like morphology (often called step-meandering). This morphology appears for surfaces with smaller steps compared to the hillocks. Many materials systems exhibit such a pattern, especially metals, e.g. Cu [77] (see Fig. 2.8), Si [78, 79, 80], but also $SrRuO_3$ on $SrTiO_3$ [81].

Step-meandering was first predicted by Bales and Zangwill [82] and while it is sometimes called Bales-Zangwill instability, more recent investigations hint that the origin of the finger-like pattern observed for Cu is due to a slightly different mechanism, which will be described later in part 2.2.2. Consequently, the more descriptive terms step-meandering or finger formation will be used in this work. Coming back to the notation proposed by Krug [76], Eq. 2.3 can be generalized for a tilt $\mathbf{m}$ along the x-axis (with $\mathbf{m} = (m, 0)$):

$$\frac{\partial \epsilon}{\partial t} = \nu_{\parallel}\frac{\partial^2 \epsilon}{\partial x^2} + \nu_{\perp}\frac{\partial^2 \epsilon}{\partial y^2}, \tag{2.5}$$

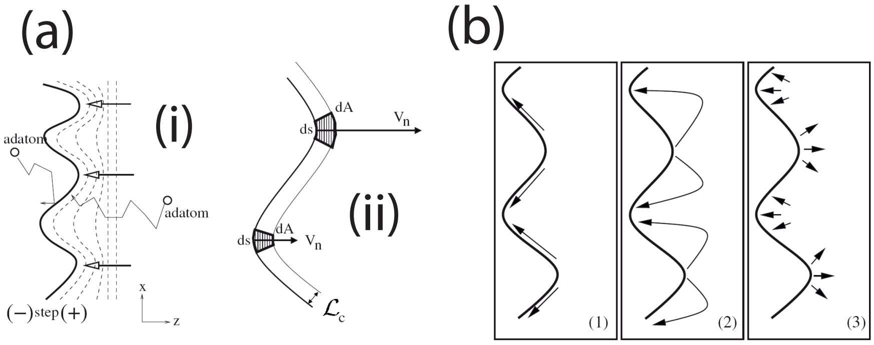

Figure 2.9: Two schematics for an ESB induced morphology displaying the top view of a step. (a) Mass transport to a step-edge which leads to variation in the local growth rate between the valleys and the hills and thus to step-meandering: (i) for single adatoms and (ii) generalized for a strip feeding an element on the step-edge. (b) Options for mass transport at an step-edge: (1) along the step-edge, (2) *via* the step and (3) *via* desorption and adsorption. Both schematics have been taken from Misbah *et al.* [67].

where the coefficients parallel and perpendicular to the offcut direction are given by [76]:

$$\nu_{\parallel} = -[f(m^2) + 2f'(m^2)m^2] = -dj/dm \qquad \nu_{\perp} = -f(m^2) = -j(m)/m, \tag{2.6}$$

with j(m) the 1D version of Eq. 2.1. The growth rate of the perturbation is now $\omega(\mathbf{q}) = -\nu_{\parallel} q_x^2 - \nu_{\perp} q_y^2$. When the perturbation perpendicular to the step becomes amplified ($\nu_{\perp} < 0$), the steps become wavy and undergo a growth instability leading to meandering. As the steps cannot cross, the meander need to be deformed in phase with each other. The arriving mass flow thus further feeds the meander with a different lateral growth rate of the step-edge [76, 67]. This is indicated in the schematics in Fig. 2.9 [67], which displays the transport at an step-edge and the mass transport to the step-edge.

Finally, the third feature induced by the ESB is the formation of step-bunching, also observed in many materials systems. In that case, the uniform width of the initial steps becomes modulated and the surface separates into regions with a high step density (bunches) and wide steps (macro steps). This effect is likely to happen if the perturbation parallel to the steps is amplified, *i.e.* $\nu_{\parallel} < 0$. While step-bunching will not be discussed here, further information can be found in the above mentioned book chapter [76] and review [67]. A schematical overview taken from Misbah *et al.* [67] shows the different mass transport regimes that lead to the three observed kinetic morphologies (Fig. 2.10).

It needs to be pointed out that there can also be stabilizing processes that can counter the uphill masscurrent induced by an ESB, and thus reduce the effect of the ESB on the morphology. There are basically two possibilities: the asymmetry of attachment itself can be alleviated, e.g. by providing a second diffusion channel where adatoms do not encounter an ESB (see part 2.5.2), or the ESB-induced uphill masscurrent can be reduced. The latter needs to be discussed in more detail. In Fig. 2.9 (b) the mass transport options at a step-edge were presented. The

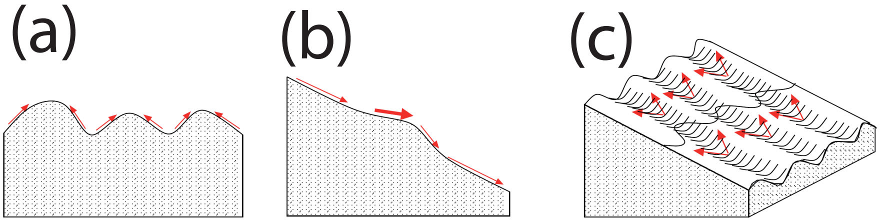

Figure 2.10: Three schematics for an ESB induced morphology displaying the surface mass fluxes which destabilize a surface (lateral view): (a) mound formation by uphill massflow, (b) step-bunching by slope-dependent variations in mass flux, and (c) step-meandering induced by an 2D uphill mass flow. The schematics have been taken from Misbah *et al.* [67].

massflow is intendedly facing “downhill” (an ESB-induced one would be “uphill”), as it will be used to highlight mass transport that counteracts the one induced by the ESB. Different possibilities exist for adatoms to move from one position on the step-edge to another. In Fig. 2.9 (b(1)) the mass transport along a step-edge *via* step-edge diffusion is displayed. In Fig. 2.9 (b(2)) the mass transport takes place *via* the step. In Fig. 2.9 (b3) the mass transport proceeds *via* desorption and adsorption. Such a “downhill” diffusion as shown in Fig. 2.9 (b) can be induced by line tension [67], sublimating atoms from the step-edge and leading to a straight step-edge. More information can be found in reference [67][p. 991 *et seq.*]. The desorption can be also higher for atoms on a step-edge part with a higher curvature, leading to a similar result. Both processes have in common that they should be enhanced for higher temperature and that they should play a stronger role when the impinging flux (and thus the growth rate) is low: at a high V_{gr} their contribution can probably be neglected; however, if they are present, the uphill masscurrent induced by an ESB could be canceled at low V_{gr}, which could lead to a vanishing of the kinetic morphologies despite the presence of the asymmetry.

2.2.2 Growth rate dependency and kink *vs* step effect

Meanders will appear on a vicinal surface in the presence of a perturbation (e.g. step width or massflow variation) and if the strength of the ESB is high in regard to the energy of the diffusing particles. Step-meandering thus takes place if the growth is still in an unstable 1D growth regime. If the diffusion length is too low, a transition to a 2D regime occurs and hillocks form. Indeed, if the particles encounter other adatoms before they can reach the step-edge, they can start to form an island, which acts as nucleation point for hillock or finger formation. Therefore, the width of the steps needs to be small compared to the island spacing on a flat surface to avoid mound formation. Note that the ESB-induced morphology is V_{gr} dependent, which will be discussed in more detail later on.

Here, it should be pointed out that there are two types of ESBs: the case described so far is called step Ehrlich-Schwöbel effect (SESE). This is a 2D effect, as the asymmetry is at a step-edge. The other is the 1D kink Ehrlich-Schwöbel effect (KESE), where the ESB is at a kink: the particles attached to a step-edge diffuse along it until they find a kink to incorporate. 1D

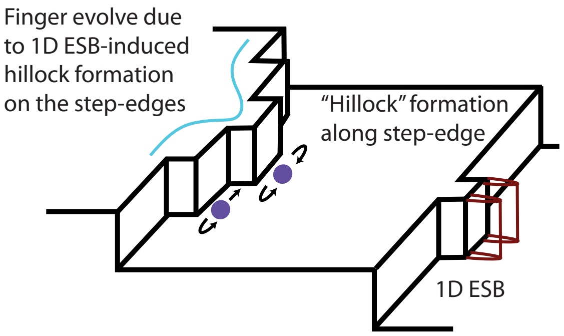

Figure 2.11: The effect of a 1D ESB (KESE) on the morphology: mound formation along a step-edge finally results in a finger morphology.

bumps or hillocks along the step-edge can lead to a mound formation if an ESB exists there - a 1D case of the hillock formation described by Villain (see the inset of Fig. 2.1) - which will result also in a step-meandering morphology, as schematically displayed in Fig. 2.11. Note that higher V_{gr} can also lead to an enhanced 1D island formation on the step-edges, similar to the 2D case. Most of the time, both ESBs should be present. However, simulations suggest that in this case, the KESE should be dominant unless the SESE barrier height is very high [83, 84, 85, 67]. It should be mentioned that some authors also distinguish a 3D ESB [86, 87]. A 3D ESB has been defined as an ESB at a macro step with a step height of 4 ML or more. However, in this work, macro steps are discarded and the focus will be on normal steps (where the step-edges are of single or double ML height), as GaN can exhibit both single and double step-edges. The single and double step-edges difference plays a role when screening the ESB (see part 2.5.2).

Nevertheless, there is a difference between the 1D and the 2D ESBs: while both, the SESE and the KESE, can lead to the same morphologies, the scaling of the lateral feature size (the periodicity) λ with the growth rate V_{gr} is expected to be different between the two. The scaling of the periodicity is given by the following equation:

$$\lambda \propto {V_{gr}}^{-\beta}, \tag{2.7}$$

with β the scaling factor. In the case of a SESE, β is expected to be ~ 0.5 [83, 88], while for a KESE, β should be ~ 0.25 [83, 89]. These values have been obtained by simulations for step-meandering in cubic systems. Thus a comparison of the scaling factors with V_{gr} should allow to distinguish which of the two possibilities is more likely to be responsible for the observed step-meandering features. As mentioned above, the finger morphology of Cu has been attributed to a KESE [83, 76].

Several groups have performed simulations for the evolution of the morphology in the presence of an ESB [67, 90, 91]. In particular, Vladimirova *et al.* carried out kinetic Monte Carlo simulation (KMC) for growth of a cubic material with an ESB and for a broad range of conditions [91]. The calculated growth diagram is displayed in Fig. 2.12. It can be seen that the

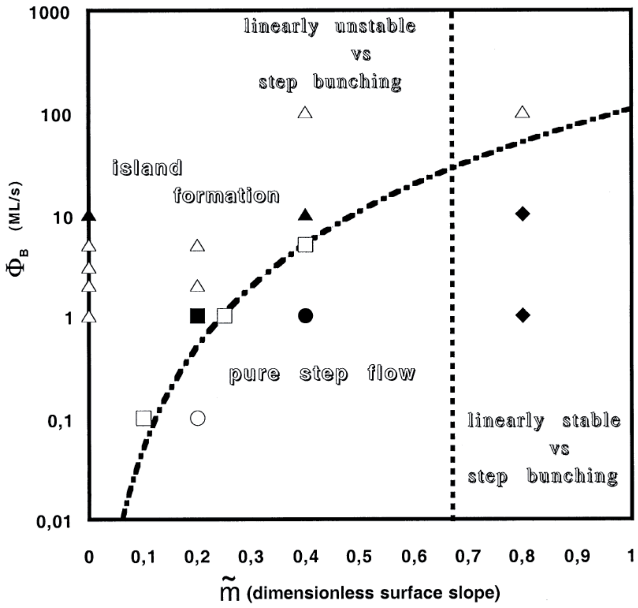

Figure 2.12: Growth diagram from simulation of the growth of a cubic material with an ESB (taken from Vladimirova *et al.* [91]). The x-axis displays the diffusion length over step-width ratio, ranging from flat morphology to a morphology where the diffusion length is equal to the step-width. The y-axis corresponds the arriving mass flux and thus the V_{gr} on a logarithmical scale. Triangles stand for mounding, squares for step-bunching followed by mounding, circles for step-bunching, and diamonds for step-meandering.

type of morphology (hillocks, finger or step-bunching) depends strongly on both V_{gr} and the ratio of the diffusion length over the step width. When the diffusion length is increased (e.g. by increasing the growth temperature), a transition from mound (or hillock) morphology to finger regime is expected. In addition, a transition to the classical step-flow mode should take place for high T_{gr}. A similar transition is also expected when reducing V_{gr}, as the effective diffusion length is enhanced, and smoothening effects could occur [67]. The suggested scaling factors and transitions will be compared to the experimental results in part 2.5 and to KMC simulations applied for an hexagonal system in part 2.4. A diagram of the experimental growth regime will be presented later (part 2.5.1). Note that in the III-nitride system, most of the growth conditions are at the right hand side of the growth diagram displayed in Fig. 2.12.

Finally, while the ESB height depends on the bonding strength at the surface, it has to be compared to the energy of the adsorbed particles. Especially at elevated temperatures, the particles have enough energy to be only slightly affected by the ESB. Lowering the temperature, the probability of attachment to the lower step-edge starts reducing, with respect to the upper step-edge. It eventually blocks the downwards diffusion at very low T_{gr}. Note that the relative strength of the ESB is materials system dependent (Ge exhibits an ESB-induced hillock formation when grown below 170°C [74, 92, 93]) and can be expected to be high for the III-nitrides, as they are generally grown at high temperature.

2.3 The different kinetic morphologies of GaN

Recently, an ESB has been evidenced for GaN by STM investigation of a sub-monolayer growth at very low T_{gr} [94]. However, the authors studied only the changes in nucleation and microstructure and did not follow up on the implications of the ESB on the morphology. In the following, the GaN morphology grown under kinetic conditions with all three growth techniques, MOVPE, NH_3-MBE, and PAMBE, will be addressed.

The GaN morphology on vicinal surfaces results from four regimes. Those four regimes are: the classical step-flow regime and the kinetic dominated hillock, step-meandering, and step-bunching regimes. They can be observed for layers grown by both MOVPE and MBE for certain growth conditions. Indeed, it will be shown here that the different morphologies previously reported for the different growth techniques are mainly due to their standard growth windows. It should be mentioned that in principle there is also the 2D layer-by-layer growth, which will be always dominated by the ESB-induced hillocks.

First, the case of ESB-induced hillock growth is presented. Then the focus will be on the step-meandering regime. The third regime, step-bunching, will be only treated briefly before the effects of the kinetic growth conditions on the material quality are analyzed. At the end of this part, a quick outlook of the morphologies observed for other III-nitrides will be given.

2.3.1 Hillock or mound morphology

Hexagonal hillock morphology is the surface morphology commonly reported for NH_3-MBE GaN [95, 96, 97]. A typical example of such a morphology is displayed in Fig. 2.13. This morphology is observed for a broad range of NH_3 and Ga fluxes. Vezian *et al.* attributed the hillocks to kinetic roughening [95]. However, it needs to be mentioned that they referred to kinetic roughening as described by Johnson *et al.*[98], who attributed the mound formation to an ESB as discussed by Villain [71], without including the formation of meanders. Very recently, Corrion *et al.* suggested that this morphology might be due to an ESB [96]. In case of an ESB-induced hillock formation, one should observe a transition to a finger regime and finally to classical step-flow mode while increasing the temperature (for a vicinal offcut surface). Corrion *et al.* did not observe this but a degradation of the material quality with an increasing pit density with T_{gr} [96].

Both interpretations rely on a kinetic origin of the surface features. First, they seem to be rather insensitive to dislocations. The hillock morphology appears independent of the substrate, e.g. sapphire, Si, or FS GaN [97]. Second, nearly all of the hillocks terminate in a triangular monolayer without visible defects and exhibit closed loop steps, which is in good agreement with the predicted ESB-induced mound morphology [67, 71, 73, 91, 99], as well as with kinetic roughening [97, 98]. This indicates that screw dislocation induced growth spirals, which are common for MOVPE grown GaN [44], are likely not the main driving force behind the hillock formation in NH_3-MBE GaN. It should be mentioned though that from time to time such a growth spiral can be observed: they have a dislocation in the center and are also always a bit

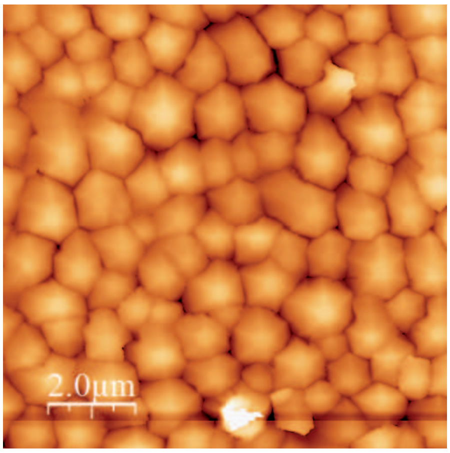

Figure 2.13: 10 x 10 μm^2 AFM image of GaN grown by NH_3-MBE in the hillock regime at 800°C with 100 sccm NH_3. The rms roughness is 9 nm.

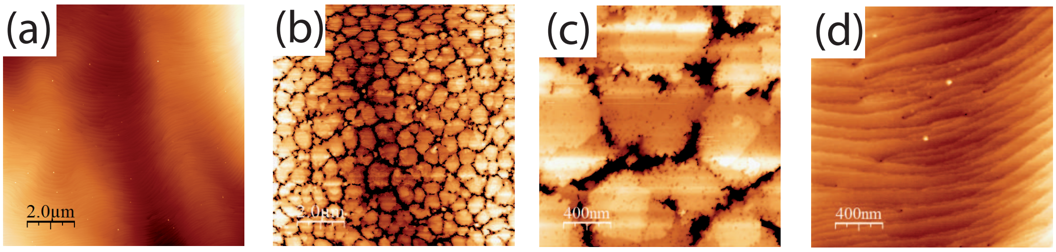

Figure 2.14: 10 x 10 μm^2 and 2 x 2 μm^2 AFM images of MOVPE grown GaN: (a) and (d) show the as-grown HT GaN reference, while (b) and (c) display the sample after 10 min of annealing in the MBE reactor at 850 °C under 200 sccm NH_3 flow.

higher than the other hillocks. Third, the hillock morphology turns to a classical step-flow morphology upon thermal annealing (TA) [95], showing clearly that the surface is not thermally stable.

PAMBE is usually grown at lower T_{gr} (around or below 740°C) than NH_3-MBE and utilizes metal-rich conditions (which will be discussed later in part 2.5.2). Indeed, growing nitrogen-rich PAMBE at these temperatures leads to 3D growth with hexagonal hillocks. An example of such hillocks can be seen in reference [100]. Note that those hillocks are similar to the ones observed for NH_3-MBE GaN.

One interesting fact to note is that an *in situ* annealing of a smooth MOVPE GaN layer can lead to the appearance of mounds. Fig. 2.14 displays MOVPE GaN layers as-grown and after 10 minutes *in situ* annealing in MBE system (at 850 °C under a high NH_3 flow). In this case, the temperature is high enough to allow for a rearrangement of the surface, while the high NH_3 flow (200 sccm) limits the desorption.

Finally, the case of hillocks in MOVPE grown GaN is more complicated to understand. First, the standard growth conditions for MOVPE GaN are at much higher T_{gr} than for MBE GaN.

This means that the diffusion length is high and the relative height of the ESB low compared to the thermal activation energy of adatoms. With such growth conditions, a step-flow growth regime should take place. However, the presence of screw dislocations in the GaN layers grown on sapphire leads to the formation of growth spirals and therefore to long scale roughness. This surface morphology has nothing to do with the hillocks observed on MBE samples. To really observe an ESB-induced mount, only truly dislocation free substrates should be used.

So mound formation has been observed for GaN grown on nominal or vicinal surfaces at low T_{gr}. This mound formation thus originates from a kinetic effect. If the mounds are due to an ESB-induced uphill current (2D growth regime), they should transform into a finger morphology (or step-bunching) at higher diffusion length (or higher offcut angle), when the 2D to 1D growth transition takes place. As reported recently by Sarzynski *et al.* [101], a flat surface can lead to mound formation, which can be suppressed by increasing the offcut angle, reducing thereby the step width. This behavior would be expected for ESB-induced mounds. However, to clearly attribute the hillocks to an ESB, finger morphology (or step-bunching) needs to be observed. On the other hand, if the mounds come from kinetic roughening as described by Vezian *et al.* [95], no step-meander should be obtained.

As seen in the following part, finger formation is indeed observed when increasing T_{gr}, confirming the assumption that the hillocks are due to an ESB-induced uphill masscurrent.

2.3.2 Step-meandering or finger morphology

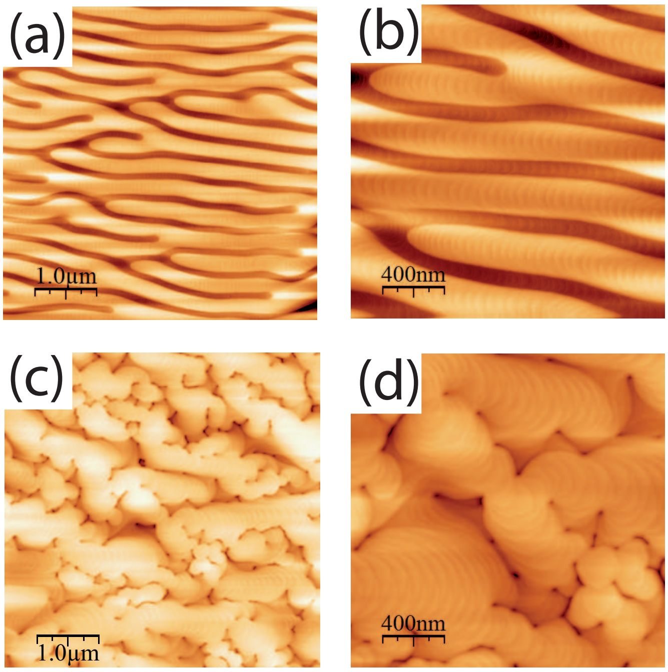

Figure 2.15: AFM images of 100 nm LT GaN grown at 840°C: 5 x 5 and 2 x 2 μm^2 grown on (a)-(b) FS GaN and (c)-(d) sapphire.

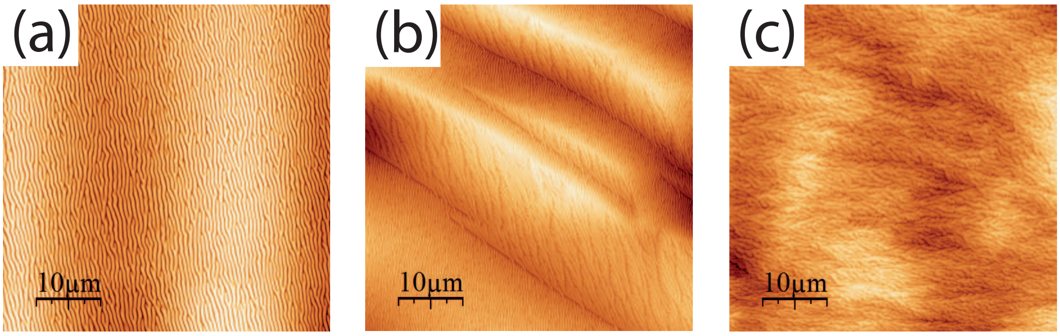

Figure 2.16: 50 x 50 μm^2 AFM images of 100 nm LT GaN grown at 840°C on FS GaN: (a) with a homogeneous offcut and (b) with local offcut variations. In (c), a corresponding sample grown on sapphire is displayed. Note that the different size of the finger originate from different growth conditions, which will be discussed in part 2.5.1.

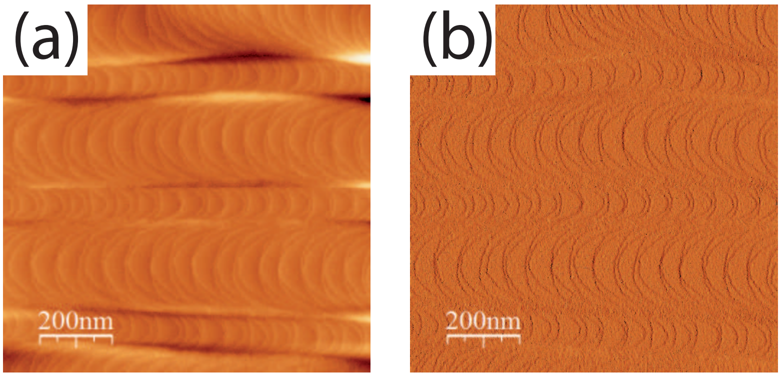

Figure 2.17: AFM images of 100 nm LT GaN grown at 840°C on FS GaN: (a) 2 x 2 μm^2 image of the finger region with well resolved steps and (b) its derivative.

On a vicinal offcut surface, the ESB can induce a finger or step-meandering morphology when the diffusion length is high enough to enable a 1D growth regime. This morphology appears for MOVPE grown GaN when T$_{gr}$ is reduced compared to standard growth conditions. While smooth step-flow morphologies are obtained for HT GaN grown by MOVPE above 1000°C the same offcut leads to finger morphology when the growth is performed under conditions used for QW barrier (N_2 as carrier gas, 840°C). 100 nm thick GaN layers grown at such LT conditions by MOVPE on both FS GaN and sapphire are displayed in Fig. 2.15. Note that this LT GaN is deposited on a HT GaN buffer exhibiting a smooth step-flow morphology. A periodic array of fingers that follow the offcut direction can be observed for the sample grown on FS GaN (Fig. 2.15 (a) and (b)). When the substrate has a homogeneous offcut, this array of fingers is visible on a large scale (Fig. 2.16 (a)). In some circumstances, e.g. an inhomogeneous offcut of the substrate, a local change in finger orientation (and diameter) can be observed (Fig. 2.16 (b)). On a small scale (Fig. 2.17), the atomic steps on each finger can even be clearly resolved. However, for the sample grown on sapphire, the finger morphology is altered (Fig.2.15 (c) and (d)). Although clearly visible on a large scale (Fig. 2.16 (c)), it is far less homogeneous than any

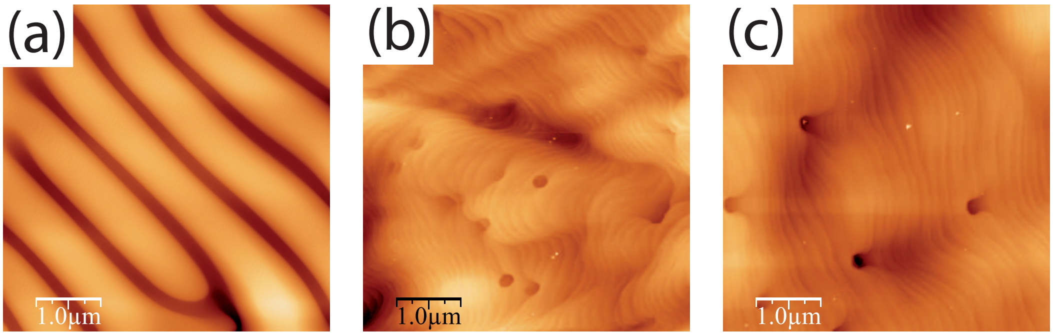

Figure 2.18: 10 x 10 μm^2 AFM images of 700 nm LT GaN grown on FS GaN (a) as grown, and annealed at 1000°C for (b) 15 minutes and (c) 30 minutes.

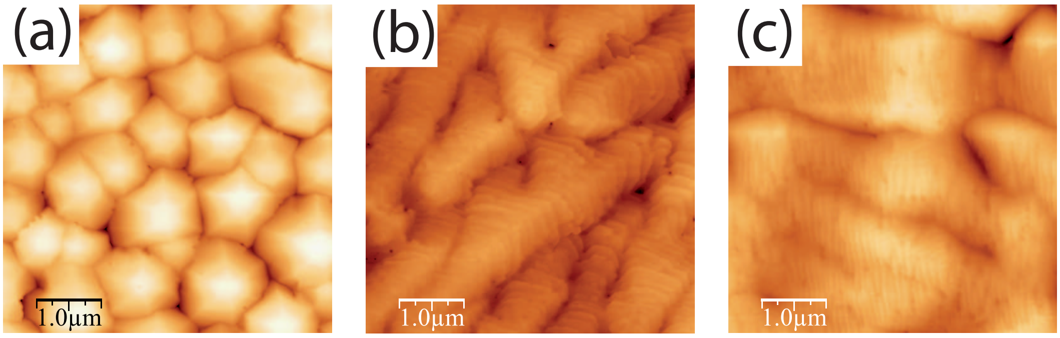

Figure 2.19: 10 x 10 μm^2 AFM images of a NH_3-MBE GaN grown at (a) 800°C with 100 sccm NH_3, (b) 865°C with 300 sccm NH_3 and (c) 920°C with 400 sccm NH_3. The corresponding rms surface roughnesses are 6.1 nm, 1.9 nm and 1.1 nm respectively.

of the FS GaN samples. On a small scale, the morphology is perturbated and distorted by the presence of pinned dislocations (Fig. 2.15 (c) and (d)). While the effect of dislocations on the meandering morphology will be discussed in more detail in part 2.6.1, it can be concluded that the finger morphology is independent of dislocations, but is strongly affected when they are present. This is in contrast with some earlier interpretation by Sadler *et al.* [102], who attributed the appearance of the finger morphology to the presence of dislocations. In another earlier report, Sonderegger *et al.* ascribed this finger morphology to originate from an underlying InGaN layer [103]. In our case, the LT GaN layer is grown on FS GaN substrates (with a low dislocation density), which excludes the effect of strain or the impact of dislocations.

The finger morphology observed for GaN is in good agreement with the morphology which has been found and simulated for other materials systems taking into account an ESB [67]. This was shown for instance for Cu (Fig. 2.8) in the previous part. Assuming that the observed finger morphology is indeed originating from an ESB, the pattern should not be stable under TA. Annealing should allow to recover the classical step-flow morphology, provided it is performed at high temperature (which means a high diffusion length) and under NH_3 atmosphere to avoid desorption, similar to what was observed for the hillocks [95]. In this case, surface migration and reattachment at energetically favored positions leads to a filling of the valleys

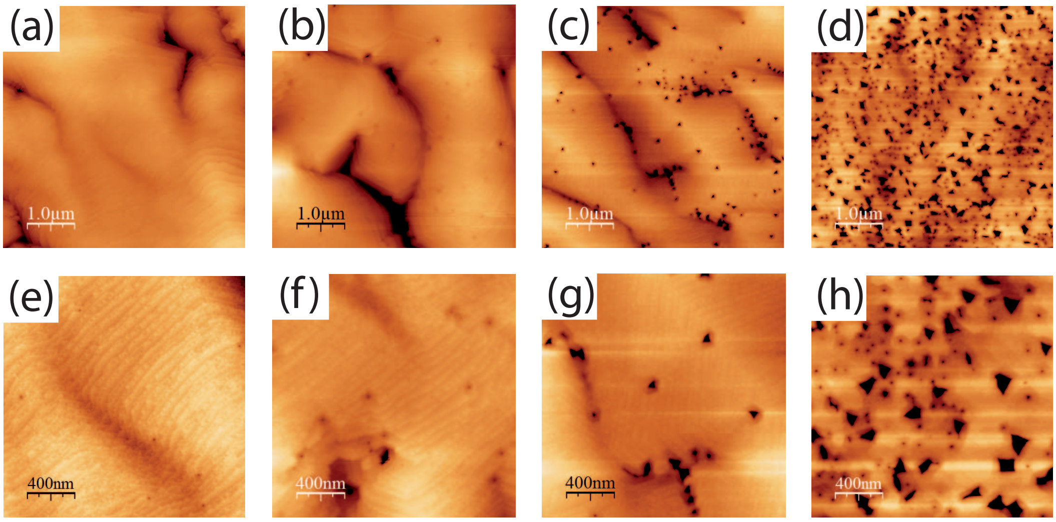

Figure 2.20: AFM images of a NH_3-MBE GaN grown at 865°C: 5 x 5 μm^2 for (a) 400 sccm NH_3, (b) 300 sccm NH_3, (c) 200 sccm NH_3 and (d) 150 sccm NH_3. The corresponding 2 x 2 μm^2 are displayed in (e)-(h). When lowering the amount of NH_3, the pit-density increases.

and a smoothening of the morphology. Indeed, annealing the GaN finger morphology at 1000°C for 30 minutes allows recovering of the classical step-flow morphology, as displayed in Fig. 2.18 (c). Note that this is a gradual process and an intermediate stage is reported in Fig. 2.18 (b).

A similar finger morphology can be also obtained by NH_3-MBE or PAMBE (under nitrogen-rich conditions). The growth conditions necessary to achieve such a morphology are straightforward. While NH_3-MBE and nitrogen-rich PAMBE usually grow in the hillock regime, it is possible to switch to a 1D growth regime by growing at elevated temperatures. The evolution of the surface morphology with T_{gr} is displayed in Fig. 2.19 for NH_3-MBE: a clear transition from the mound to the finger regime is observed. This change in the growth regime is accompanied by a reduction in the surface roughness, from 6.1 nm to 1.1 nm for a 5 x 5 μm^2 area. Note that the NH_3 flux was increased with the temperature to counterbalance the enhanced Ga desorption. As a result, the V_{gr} was slightly reduced due to NH_3 flux screening of the molecular beam [104]. However, the same growth regime exists for a broad range of NH_3 fluxes (and V_{gr}), as shown in Fig. 2.20.

It should be also mentioned that the finger regime appears to be more sensitive to defects. In this regime, defects lead to the appearance of screw-dislocation-induced hillocks, which intersect and block the fingers from time to time, as presented in Fig. 2.21 (hillocks regime is also shown for the sake of comparison). An interesting fact to note is that the surface morphology changes rather quickly. Fig. 2.22 (b) - (d) displays the surface morphology of a sample consisting of 30 nm of HT GaN grown at 865°C on top of 500 nm of GaN grown at 800°C in hillock mode (Fig. 2.22 (a)). A transition to a finger morphology is clearly observed.

GaN grown by PAMBE under nitrogen-rich conditions can also exhibit finger morphology.

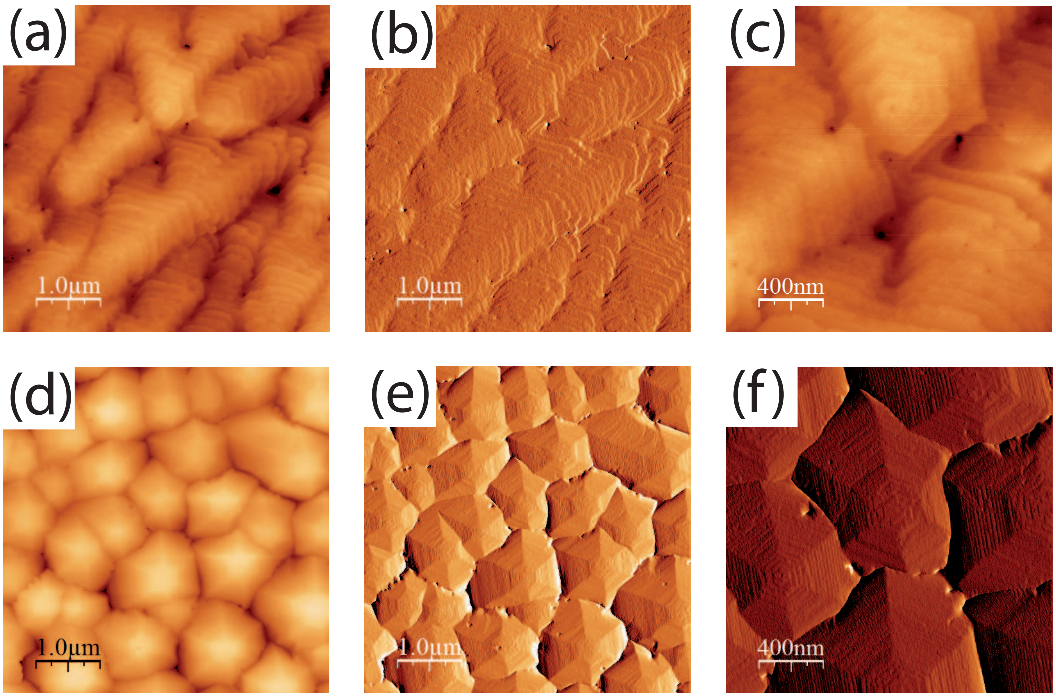

Figure 2.21: AFM images of a NH_3-MBE GaN grown at 865°C with 300 sccm NH_3: (a) a 5 x 5 μm^2 (b) its derivative and (c) a 2 x 2 μm^2 image. GaN grown at 800°C with 100 sccm NH_3 is displayed: (d) a 5 x 5 μm^2, (e) its derivative and (f) a 2 x 2 μm^2 derivative image.

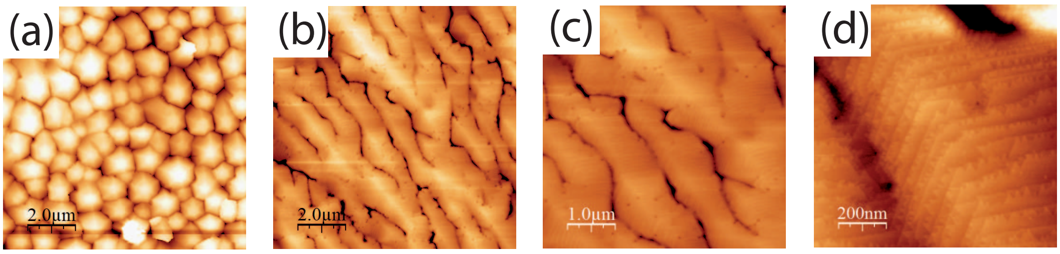

Figure 2.22: AFM images of a NH_3-MBE GaN. (a) shows a 10 x 10 μm^2 image of a reference grown at 800°C. In (b)-(d) AFM images of 500 nm of GaN at 800°C overgrown with 30 nm of GaN at 865°C with 300 sccm NH_3 are shown, the displayed areas are 10 x 10 μm^2, 5 x 5 μm^2 and 1 x 1 μm^2.

This happens for a nitrogen-rich growth window at a high temperature range (close to the ones used for NH_3-MBE), which was proposed by Koblmüller *et al.* [105, 106]. A sample was thus grown under nitrogen-rich conditions by PAMBE at T_{gr} of 790°C on FS GaN. A clear switch from the pyramidal to the finger morphology can be seen in Fig. 2.23. This indicates that nitrogen-rich PAMBE is similar to NH_3-MBE. The ESB-induced hillock growth can be shifted to a finger morphology by increasing the temperature. The same effect could be achieved by increasing the offcut. Finally, MOVPE grown GaN shows the same finger morphology when T_{gr} is low (QW barrier conditions), indicating that the morphology is indeed independent of

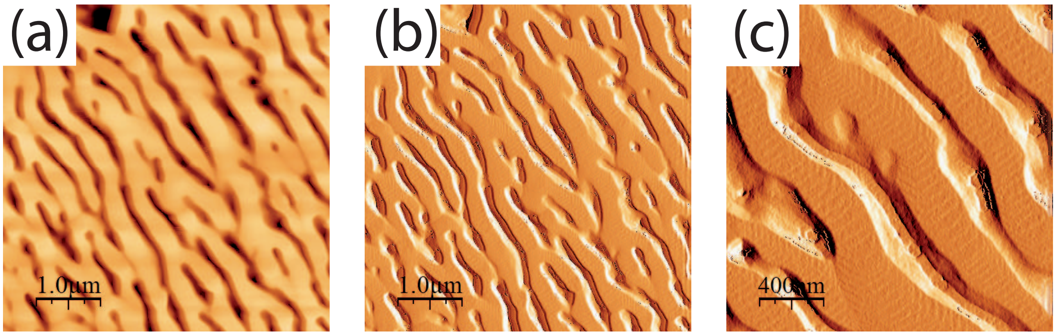

Figure 2.23: AFM images of 700nm GaN grown under nitrogen-rich conditions at 790°C by PAMBE on FS GaN: (a) 5 x 5 μm^2 image, (b) its derivative and (c) a derivative of a 2 x 2 μm^2 image where atomic steps on top of the fingers can be distinguished.

the growth technique but depends on the surface kinetics. Note that metal-rich PAMBE will be discussed later (part 2.5.2), together with the influence of the carrier gas for MOVPE.

2.3.3 Step-bunching

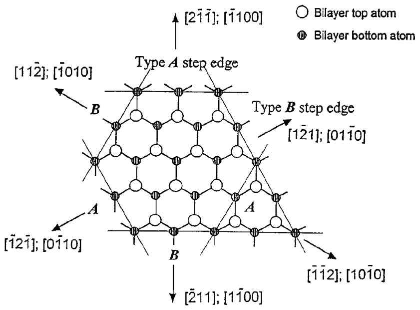

Figure 2.24: step-edge configurations for the A and B layers, taken from Xie *et al.* [107].

The last ESB-induced surface morphology on a vicinal substrate is step-bunching, as described briefly in part 2.2.1. An intrinsic step-bunching-like feature takes place for GaN grown by MOVPE in the classical step-flow regime. The surface usually exhibits step-edges of double monolayer height for HT GaN growth conditions, unless it is disturbed by a perturbation (e.g. a dislocation). NH_3-MBE GaN is different: a smooth step-edge of one ML height is followed by a “zig-zag” or saw-tooth pattern for the next ML (see e.g. Fig. 2.22 (d)), as described by Xie *et al.* [107]. This is due to different V_{gr} of the step-edges, combined with the 30° rotation between the A and B layer. A schematic of the step-edge configuration is presented in Fig. 2.24. For MBE, the twisted step-edges do not catch up with the step-edge below, leading to the triangular pattern of single step height. In the case of MOVPE, the double steps are controlled by V_{gr} of the slower growing step-edge. While the surface features could be interpreted as step-bunching, it will not be treated as such in this work, as the origin is due to different atomic configurations of the step-edge induced by the wurtzite stacking order.

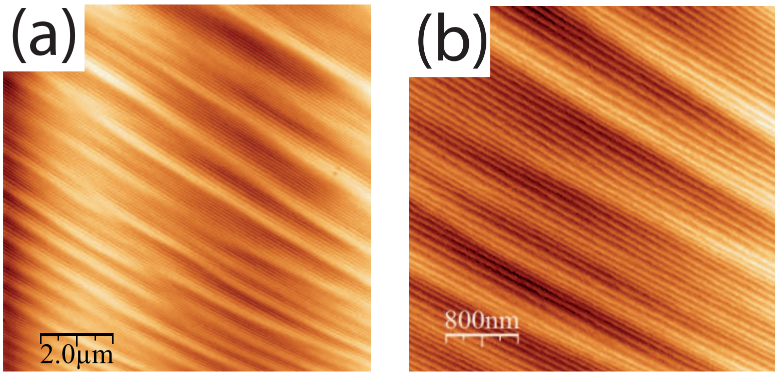

Figure 2.25: AFM images of a GaN structure grown on FS GaN which exhibits step-bunching: A) 10x10 μm^2 and B) 2x2 μm^2. The images are by courtesy of G. Cosendey (LASPE-EPFL).

Nevertheless, step-bunching can be observed for some conditions in GaN [108]. An example for a MOVPE grown structure is displayed in Fig. 2.25. This step-bunching would also be strongly affected by the presence of dislocations, and thus a clear step-bunching can only be expected for structures grown on FS GaN. Additional information about step-bunching can be found in the review from Misbah *et al.* [67]. For a future work, it would be interesting to investigate the parameters that influence step-bunching in more detail.

2.3.4 Characterization of GaN grown under kinetic conditions

The material quality of LT GaN epilayers was probed with the following characterization tools: XRD, PL and PAS. Three 700 nm thick samples were prepared on FS GaN. Two finger morphology samples were grown by MOVPE (840°C, N_2 as carrier gas) and PAMBE (790°C, nitrogen-rich conditions), and one hillock sample was synthesized by NH_3-MBE (800°C, 100 sccm NH_3). Investigating those 700nm thick LT GaN layers in more depth reveals a high structural quality: the (002) XRD rocking curve exhibits a narrow full width at half maximum (FWHM) of 275-300 arcsec, which is within the range of the FS GaN template used for this work (Fig. 2.26). This indicates no sign of a degradation in crystalline quality due to the low growth temperature. In addition, low temperature PL shows well-resolved exciton peaks for the three LT GaN layers (Fig. 2.27). The peaks of the free excitons as well as the donor and acceptor bound excitons are clearly resolved. Note that the acceptor bound exciton peak is rather intense for the MOPVE grown layer, possibly due to significant carbon or magnesium incorporation. This might be due to incomplete organometallic decomposition (C) or memory effects (Mg). Finally, Christian Rauch from the group of Filip Tuomisto from Aalto University, Finland, performed PAS, a technique that is sensitive to negative charged point defects [109, 110]. The level of Ga vacancies was at the detection limit of the system, indicating no visible degradation in crystalline quality compared to the FS GaN template.

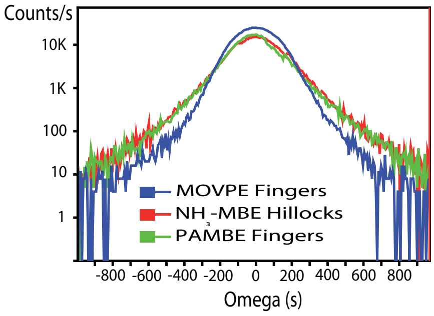

Figure 2.26: The XRD rocking curves of 700nm GaN on FS GaN in the finger regime (MOVPE, PAMBE) and hillock regime (NH_3-MBE.

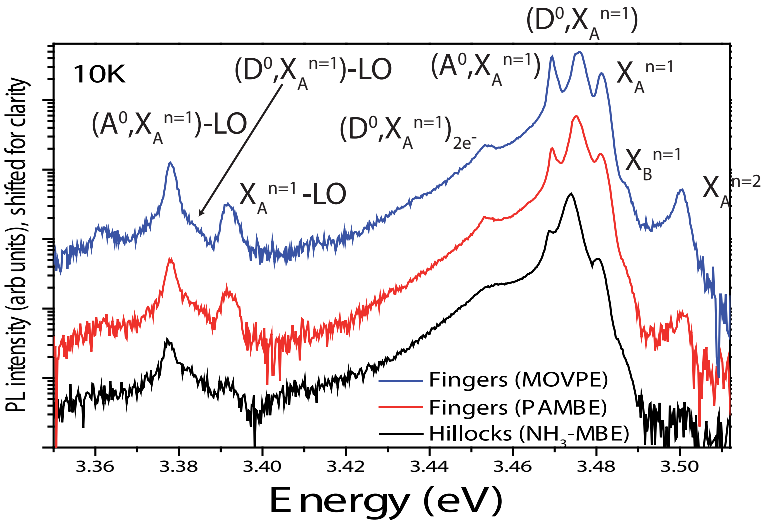

Figure 2.27: PL measurements of a HT GaN buffer on FS GaN and of 700nm thick GaN layers in the finger regime (MOVPE, PAMBE) and hillock regime (NH_3-MBE). The exciton peaks and the LO phonon replicas are indicated.

In conclusion, a deterioration of the crystalline quality was not observed for the growth conditions used here. However, this does not exclude possible higher point defect densities. Also, the signature of acceptor bound excitons on the PL spectra indicate a higher residual concentration of impurities, which is likely when decreasing the growth temperature.

Nevertheless, kinetics can be applied to control and play with the surface morphology. This may have beneficial effects, e.g. by using a finger pattern to increase carrier localization in InGaN QWs grown on top, as shown in the end of this chapter.

2.3.5 Overview of the morphology for other III-nitrides

While the basics of growth kinetics were studied on homoepitaxial GaN, the LT growth conditions investigated here are commonly used for the active region of optoelectronic devices. Fundamentally, the presence of an ESB in GaN means that an ESB is likely to exist in other III-nitrides. While InGaN QWs will be treated later (without discussing the ESB), there have been some reports of surface features which appear to be ESB-induced.

As already reported [103], a finger morphology has been observed for a 10 nm MOVPE grown InGaN layer (15% In, T_{gr} = 740° C), as seen in Fig. 2.28 (a). In addition, round InGaN mounds have been reported for thick InGaN layers grown on a substrate with a low offcut angle (Fig. 2.28 (b)) [101]. This morphology changes to a classical step-flow morphology as well as to step-bunching at higher offcut angles [101]. Uncapped InGaN QWs grown at low temperature also exhibit hillocks with a similar scaling (see part 2.5.1) as predicted for ESB [111]. In Fig. 2.28 (c), a finger-morphology is demonstrated for AlGaN (with 15% of Al) grown by NH_3-MBE on a FS-GaN template. For higher Al content and a higher V_{gr} and on an AlN template, an $Al_{0.3}Ga_{0.7}N$ sample (Fig. 2.28 (d)) exhibits a hillock morphology, showing that both ESB-induced morphologies can be obtained for AlGaN as well. Such hillocks can also be observed for AlN grown by NH_3-MBE on both sapphire and Si (Fig. 2.28 (e) and (f)). Other groups have reported a similar morphology [112] and hillocks have been observed for InN too [113].

There is another ternary alloy, InAlN, that is investigated in more depth in our group and which is of great interest for the III-nitrides, as it can be grown lattice matched to GaN with around 17% In [35]. This allows in principle to achieve a very high structural quality when grown on FS GaN substrates. However, the growth temperature is strongly limited due to indium desorption, which in turn hinders the surface diffusion length of aluminum. As a consequence, it will be seen that surface kinetics play a major role and have detrimental effects on the material quality. Under optimized conditions and on FS GaN, the lattice-matched InAlN surface morphology consists of regular round mounds which are aligned to the underlaying GaN step-morphology. Such mounds agree very well with ESB-induced mounds, especially as they are very flat (the height is below 1 nm) and still aligned to the GaN steps after even 50 nm of InAlN growth. Fig. 2.29 displays the evolution of the morphology of the lattice-matched InAlN for different growth thicknesses. Here, two issues need to be discussed: first, while the mounds are well-aligned to the steps, it can not be distinguished whether the mounds originate from the center of a GaN step or more closely towards the downwards step-edge (the latter would clearly indicate an ESB as the origin). Second, as the samples are grown on FS GaN, no dislocations perturbate the morphology, at least for thin layers. On the other hand, several pits (or voids) appear at higher thickness. Apart from normal hillocks, higher mounds with pits in the center appear. In comparison, a LT NH_3-MBE-grown GaN sample (grown at 660 °C on GaN-on-sapphire) exhibits a similar morphology (Fig. 2.29 (e)). The InAlN pit formation is followed by the formation of columns and phase separation into regions with different In contents (Fig. 2.30 (a) - (c)). This change happens after a critical thickness, even for strain-free InAlN grown on FS GaN. The pit formation and change in growth regime

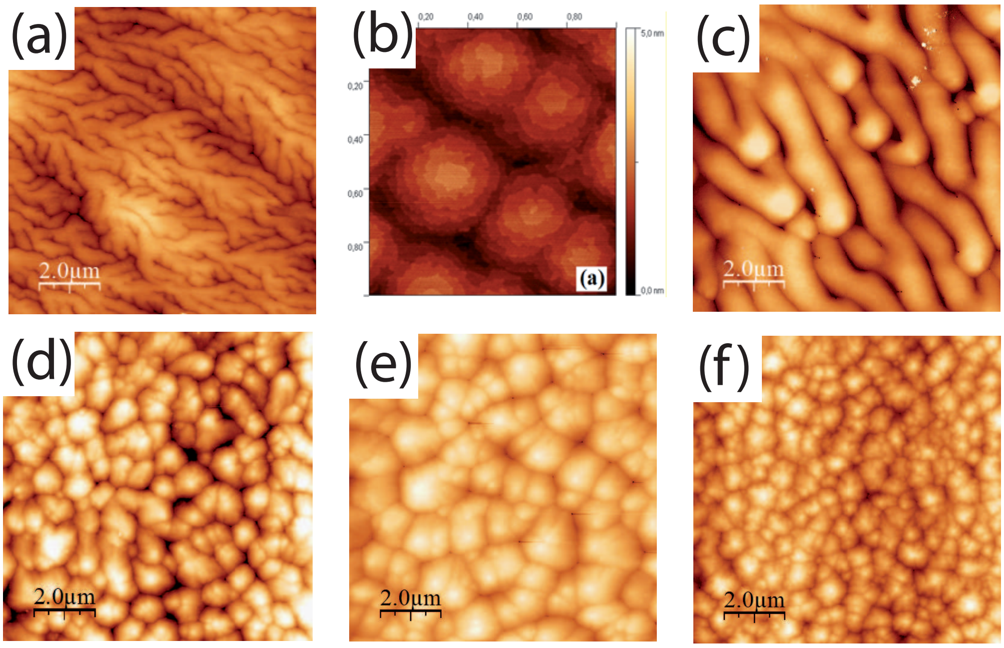

Figure 2.28: AFM images of InGaN (a) and (b), AlGaN (c) and (d) and AlN (e) and (f) at different growth regimes. All but (b) (which is taken from Sarzynski *et al.* [101]) display a 10 x 10 μm^2 area. (a) is by courtesy of S. Sonderegger (EPFL); the AlGaN and AlN samples are by courtesy of E. Giraud (LASPE-EPFL). A finger morphology is displayed for InGaN and AlGaN, while a mound morphology is shown for InGaN, AlGaN and AlN.

after a critical thickness are probably due to limited surface kinetics similar to the case of homoepitaxial LT Ge growth. In the case of homoepitaxial Ge [74], ESB-induced cubic hillocks form when Ge is grown at too low temperature. After a T_{gr}-dependent critical thickness h_1, stacking faults and faceting occur at the border between ESB-induced hillocks, due to diffusion limited surface processes. From those seeds, a zig-zag-kind of pattern evolves at the interface (Fig. 2.30 (h)) with a defect-rich regime which exhibits a columnar structure. Finally, after a second T_{gr}-dependent critical thickness h_2, an epitaxial breakdown occurs and the Ge growth becomes amorphous (Fig. 2.30 (e) - (h), taken from Bratland *et al.* [74]). Note that the columnar structure originates from defects and is different from the one observed in InAlN; however, it shows that other mechanisms than phase separation can lead to defective and columnar-like structures.

Actually, the growth regime observed in Ge grown at LT is very close to what happens in lattice-matched InAlN (Fig. 2.30 (d)). The formation of the pits (see Fig. 2.29 (f)) between the mounds may indicate a strongly ESB-limited surface diffusion length, which could be responsible for phase-separation (Fig. 2.30 (a) - (c)). Indeed, it has been proposed that different surface curvatures induce a different surface potential [114]. This results in local alloy composition variations and finally in phase-separation. A more in depth discussion of the phase-separation for lattice matched InAlN can be found in reference [115]. Assuming the formation of the InAlN zig-zag-interface between the homogeneous region and the region

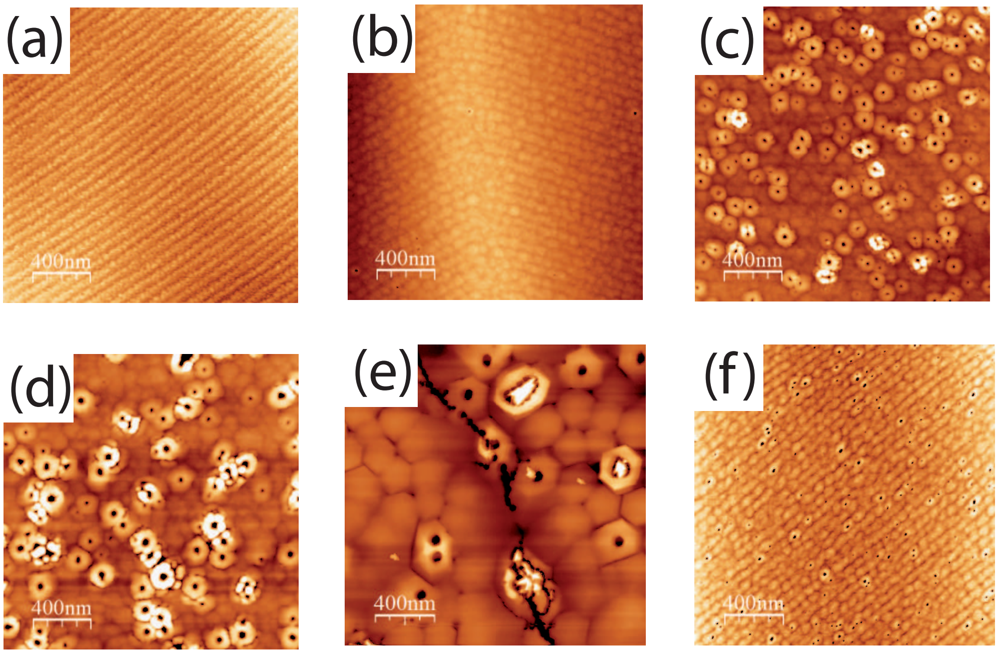

Figure 2.29: 2 x 2 μm^2 AFM images of MOVPE grown (a) 2 nm InAlN, (b) 50 nm InAlN, (c) 100nm InAlN and (d) 240 nm InAlN. In (e) 250 nm of LT MBE grown GaN (T_{gr} = 660°C) grown on sapphire is shown as comparison. In (f) 50 nm of InAlN grown with a lower In flux (but same In content) is displayed. All InAlN layers shown are lattice-matched to GaN and grown on FS-GaN (by courtesy of G. Cosendey (LASPE-EPFL)). Note that the average peak-to-valley ratio for (b) or (f) is below 1 nm.

with the phase separation (see Fig. 2.30 (a) - (c)) to originate from ESB-limited diffusion, three changes could help to prevent the change in material quality: first, T_{gr} could be increased and V_{gr} be reduced. However, due to indium desorption, this might not be feasible. Second, a strong increase of the offcut angle could allow to switch from the mound to the finger regime. This might help to prevent phase separation if the peak-to-valley ratio remains low. This needs to be investigated in more detail, as a pronounced finger-formation will also provide local offcut variations, and thus different indium incorporation, as discussed in more detail in part 2.6.1. Finally, adatoms that enhance the diffusion length could delay the phase separation, as already observed for Ge [92, 93]. Interestingly, the smoothest InAlN layers were obtained with a very high indium flux [116], while keeping lattice-matched condition (the excess In is not incorporated at the growth conditions used). As a consequence, the pit formation is delayed (Fig. 2.29 (b) - (f)). Notice that the effect of adatoms on kinetic growth is discussed in more detail in part 2.5.2.

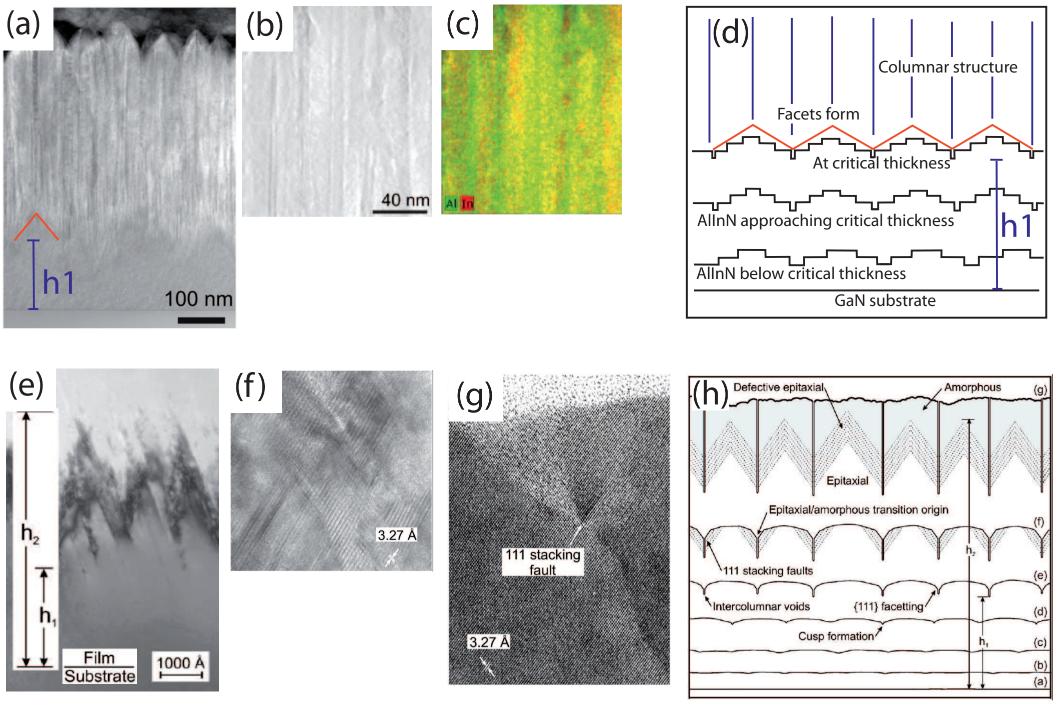

Figure 2.30: (a) shows a HR-TEM image of InAlN grown lattice-matched on FS-GaN, displaying the change from a homogeneous layer to a columnar structure with phase separation above the critical thickness (h_1). (b) a smaller section above h_1 is displayed. (c) the corresponding elemental map, showing In- and Al-rich stripes. (d) a schematic drawing of the evolution of the InAlN morphology below and above the critical thickness is presented. The HR-TEM images of InAlN ((a) - (c)) are by courtesy of G. Perillat-Merceroz (LASPE-EPFL).
To compare, (e) shows a Ge cross-section TEM image, with two critical heights. The magnifications (f) and (g) provide enlarged images of the defect region (between h_1 and h_2). (e)-(h) are taken from Bratland *et al.* [74].

2.4 Kinetic Monte Carlo simulation for the III-nitrides

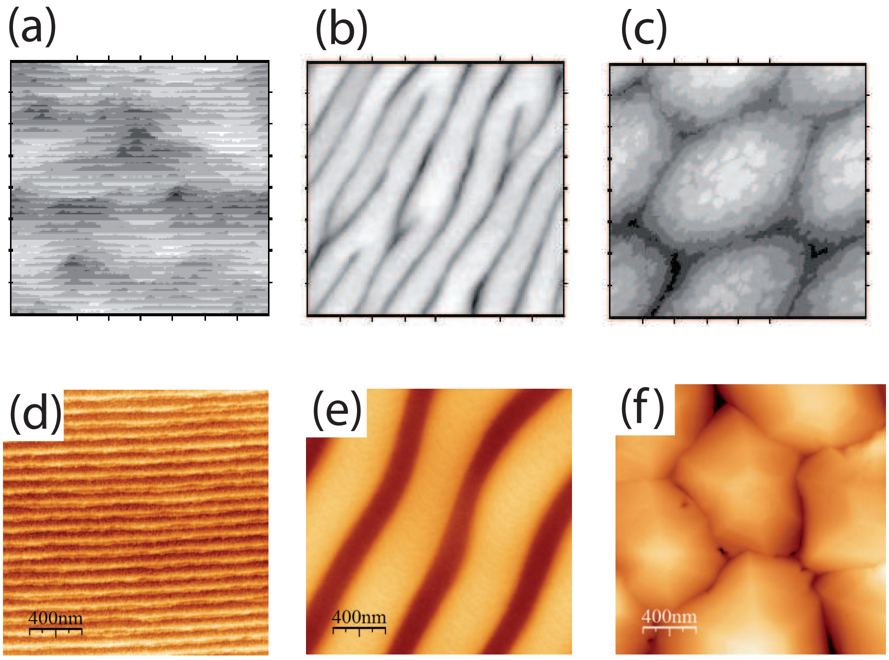

Figure 2.31: KMC simulations for growth of a wurtzite crystal on a hexagonal lattice compared to experimental data. (a) step-flow growth, (b) finger regime and (c) mound regime. (d)-(f) display corresponding 2 x 2 μm^2 AFM images of samples grown in the presented study. (a)-(c) are by courtesy of Dr. B. Hourahine (Strathclyde University).

While first theoretical simulations about step-meandering and other instabilities for the III-nitrides have appeared recently from Zaluska-Kotur *et al.* [117, 118, 119, 120], these authors do not discuss the different ESB-induced growth regimes and regime changes. To investigate the effect of an ESB on a hexagonal system and to compare it to our experimental results, a kinetic Monte Carlo (KMC) simulation has been performed by Dr. Benjamin Hourahine from Strathclyde University, UK. His work is based on the simulation of Vladimirova *et al.* [91] and on a work on step-bunching for a hexagonal lattice [121].

While the refinement of the KMC model is still going on, the first results agree well with our experimental observations (Fig. 2.31). Note that the absolute scale of the simulation is not the same as observed experimentally yet, but the scaling behavior is (see the next part). Adjusting the parameter to fit the experimental scaling is in progress. However, the trends are the same: the step-flow regime (Fig. 2.31 (a)) changes to a finger regime (Fig. 2.31 (b)) when the value of the ESB is increased. When the step width is strongly increased (and V_{gr} as well) the simulated finger regime changes to a hillock one (Fig. 2.31 (c)). The KMC simulations of growth under the presence of an ESB are thus in good agreement with the observed morphologies. This gives additional support to the ESB-related origin of the GaN morphologies. Further information can be gained by looking at the scaling behavior of the feature size with the V_{gr} and comparing it to earlier works.

2.5 Control of the morphology

In this part, the effect of V_{gr} will be first studied in detail in the framework of transitions between the different regimes and the scaling of the periodicity (the lateral feature size) with V_{gr}. In a second part, the screening of the ESB will be discussed. The role of an adlayer and the impact of the carrier gas will be treated for PAMBE and MOVPE, respectively.

2.5.1 Scaling of the morphology: growth rate and layer thickness dependencies

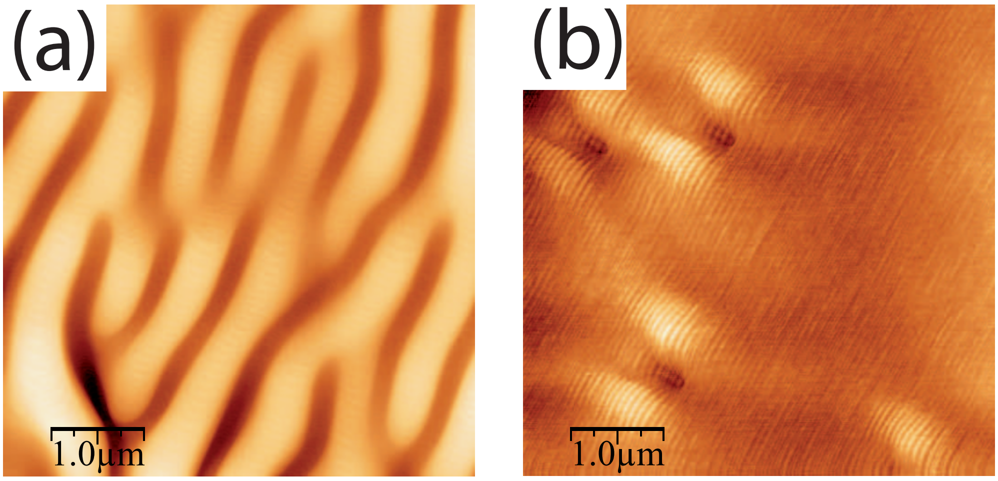

Figure 2.32: 5 x 5 μm^2 AFM images of 100 nm LT GaN grown by MOVPE at (a) 140 nm/h and (b) 70 nm/h.

The transitions from one regime to another for different T_{gr} (see Fig. 2.19) follow the trends expected from the theory [67, 91] and the KMC simulations (Fig. 2.31). Additionally, the theory suggests that the same regime change can also be observed by changing the step width (by adjusting the offcut angle, as seen for InGaN [101]), or by altering V_{gr} [67, 91]. A high V_{gr} reduces the effective diffusion length and thus affects the formation of new islands. In turn, a low V_{gr} can allow smoothening effects to play a larger role. Fig. 2.32 displays AFM images of 100 nm thick LT GaN layer grown by MOVPE under the same conditions, except V_{gr}. One can see that the step-meandering morphology changes into a smooth classical step-flow morphology simply by lowering V_{gr}. This indicates that there is a smoothening effect that gets dominant at low V_{gr}, effectively reducing the uphill masscurrent induced by the ESB (see part 2.2.1). Without a countering massflow, such a transition to a stable step-flow mode would not be expected for if an ESB is present. One explanation could be that desorption produces a downhill masscurrent that counters the uphill one induced by the ESB. However, it should be noted that although most of the surface consists of perfect smooth steps for the low V_{gr} sample, the onset of a few isolated finger can still be observed occasionally, which might be due to local variations.

A similar transition takes also place for the hillock regime in NH_3-MBE when V_{gr} is strongly

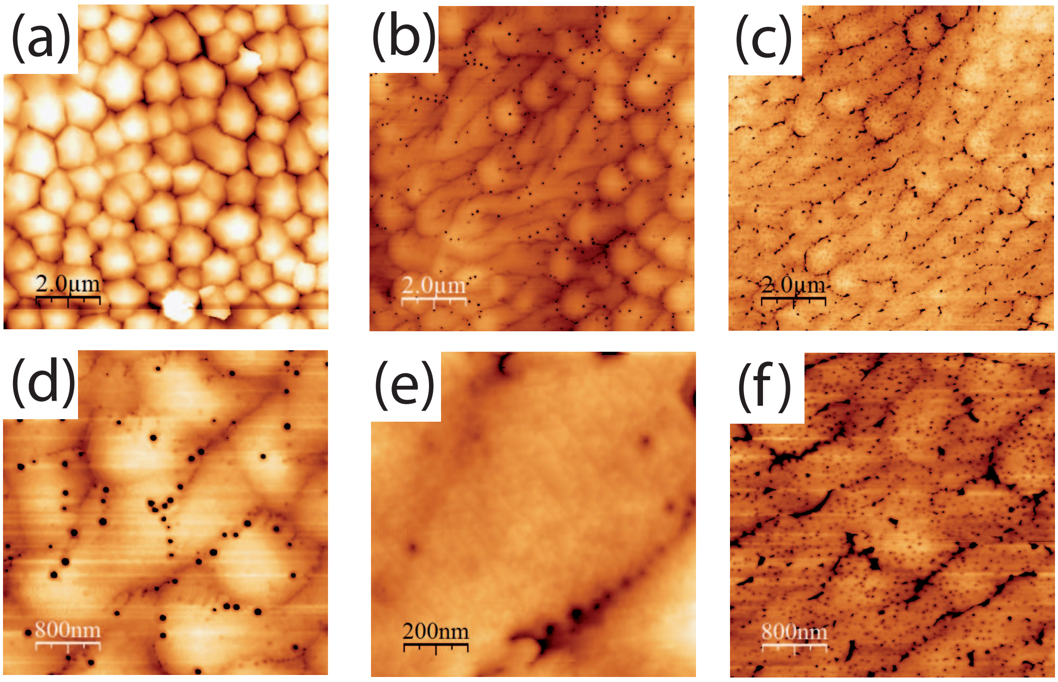

Figure 2.33: 10 x 10 μm^2 AFM images of GaN grown by MBE at 800°C at (a) 450 nm/h, (b) 110 nm/h. and (c) 60 nm/h. In (d) and (e) 5 x 5 μm^2 and 2 x 2 μm^2 of the sample grown at 110 nm/h are displayed, while a 5 x 5 μm^2 of the sample grown at 60 nm/h is shown in (f). While a transition to a smoother finger regime is observed, the density of pits is strongly enhanced for low T_{gr}.

lowered (Fig. 2.33). However, in that case the change in the morphology regime is accompanied by a deterioration of the surface morphology due to the formation of pits (local etching at dislocations is likely). However, note that this regime change does not necessary require a smoothening effect, but can be explained simply by an enhanced diffusion length at lower V_{gr}.

To briefly summarize the influence of the growth conditions discussed so far, two diagrams illustrating the domains of the different growth regimes have been constructed. In Fig. 2.34 (a), the plot of the V_{gr} over T_{gr} shows the experimentally observed transitions between the different regimes (for samples with a fixed offcut). In addition, Fig. 2.34 (b) displays the effect of the offcut on the 2D to 1D growth mode transition for two ESB with different heights (ESB 1 < ESB 2). A smoothing effect, such as experimentally observed in Fig. 2.32, effectively reduces the mass flow induced by the ESB and can thus reduce the effect of the asymmetry of attachment. As a consequence, classical step-flow can be realized despite the presence of an ESB (for low V_{gr}). The growth regime diagram follows quite well the predictions of Vladimirova *et al.* [91] for a high diffusion length (corresponding to the right hand part of Fig. 2.12).

To conclude, the energy of the adsorbed particles is temperature dependent, so increasing T_{gr} has three effects: it enhances the diffusion length and thereby reduces simultaneously the asymmetry of attachment, as the ESB height itself does not depend on the temperature

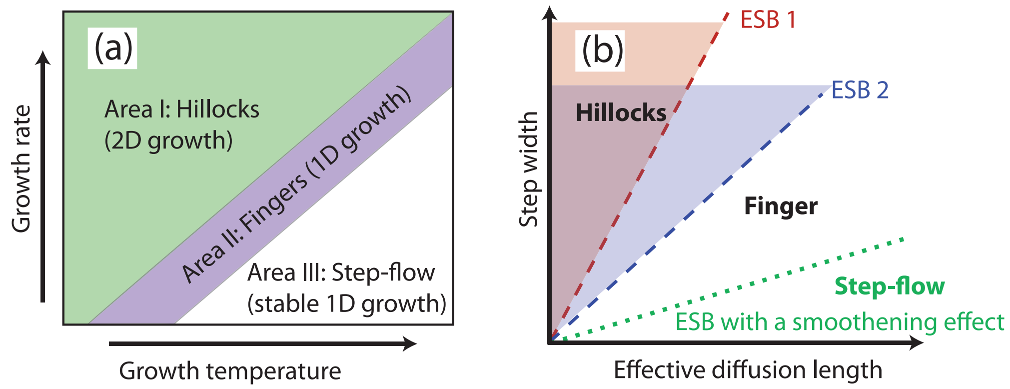

Figure 2.34: (a) Kinetic growth diagram for the three different GaN morphology classes observed on a vicinal offcut surface under conditions where an ESB is dominant (assuming a constant V/III ratio). (b) The strength of the ESB (ESB 1 < ESB 2) affects the step-width over diffusion length related transition between a 2D and 1D growth regime. In addition, the case of a smoothening effect which can counter an ESB-induced massflow is indicated.

and the probability of particles passing over the step-edge barrier is increased. At the same time, the increased diffusion length can switch the nucleation from 2D to 1D, causing a growth regime change (hillocks or layer-by-layer to finger or step-flow growth). This depends on the offcut angle. In addition, smoothening effects can also be temperature dependent. In this case, the downhill massflow which counteracts the ESB-induced uphill massflow can be increased with temperature.

Effect of the growth thickness

ESB-induced growth has some implications. The height of the surface feature (given by the peak-to-valley ratio) is *per se* independent of the growth rate: the modulation of the height (Eq. 2.1), which is responsible for the peak-to-valley ratio, should be constant while changing V_{gr}. Furthermore, the modulation should grow only slowly with the growth thickness, meaning that a large increase in thickness only leads to a small increase in the peak-to-valley ratio. This agrees well with the experimental observations. The measured peak-to-valley ratio is only about 40 nm for a few microns grown in the hillock regime (not shown), and the step-meander regime behaves similarly. It is thus possible to control the height of both surface features, hillocks and fingers, by choosing the layer thickness. However, for thin layers, only small modulations can be achieved. There are a few important points to add here. First, there is probably a maximum peak-to-valley ratio that depends on a lateral feature size. As observed for Ge, when the mounds reach a certain slope (or facet), dislocations are introduced at the islands coalescence and a phase-transition takes place, leading to a deterioration and finally to an epitaxial breakdown [74]. Thus it is likely that a maximum slope exists also for ESB-induced mounds or fingers in III-nitrides. However, such a point was not reached for the thickest layers (a few μm) investigated under the growth conditions used in this work, so a similar behavior

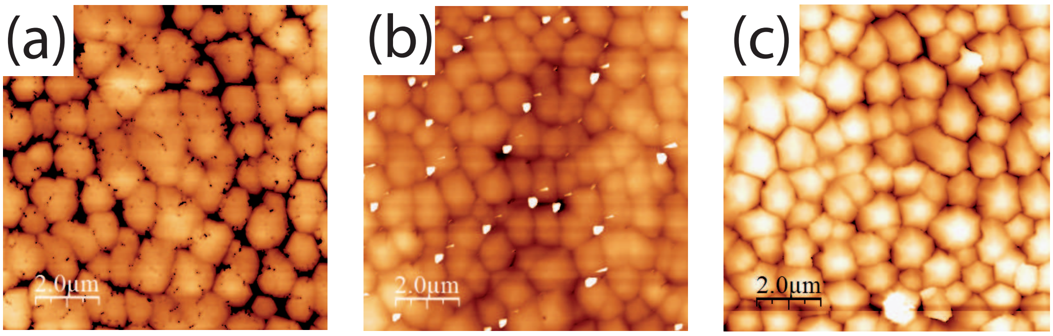

Figure 2.35: 10 x 10 μm^2 AFM images of GaN grown by MBE at 800°C: (a) 30 nm thick, (b) 600 nm thick and (c) over 2.5 μm thick. The corresponding rms surface roughnesses are 3.6 nm, 3.2 nm and 9 nm.

for GaN cannot be confirmed. Nevertheless, a phase transition was observed in InAlN and ascribed to mound formation due to ESB-limited kinetics.

Second, the lateral feature size - or periodicity - is independent on the growth thickness. That means that the height can be adjusted without affecting the lateral feature size. As shown in Fig. 2.35 for the case of MBE grown hillocks, no change in the lateral size of the mounds was observed over the thickness range under consideration (from 30 nm (Fig. 2.35 (a)) to a few μm (Fig. 2.35 (d))).

Third, the influence of other factors has been excluded so far. Especially the strain should however play an important role for the feature-size. In non-lattice-matched heteroepitaxy with plastic relaxation, the strain is highest close to the interface. It decreases with increasing layer thickness and vanishes after a complete relaxation of the layer. If the feature size is affected by the strain, it should thus change with increasing the layer thickness, and stabilize to its normal value when the layer is relaxed. Such a behavior has been reported for NH_3-MBE grown GaN hillocks on AlN [95]: with increasing film thickness, the lateral mound size increases, until is saturates and becomes independent of the thickness.

Effect of the growth rate: is a kink or a step effect dominant?

While the growth thickness does not influence the lateral feature size (without strain), the feature size is supposed to depend on V_{gr} as described by Eq. 2.7. Increasing V_{gr} (within one growth regime) leads to a reduction in feature size. The exact scaling, in form of the scaling factor β, further allows to investigate whether the observed morphology is more likely due to a KESE or a SESE. In the hillock regime, the scaling of GaN mounds with V_{gr} is displayed in Fig. 2.36, for GaN grown by NH_3-MBE at 800°C with three different V_{gr}. The fit allows to extract a scaling factor $\beta = 0.8$. In the case of step-meandering, the scaling factor is different. This is not surprising, as the uphill mass transport to the mounds comes from all directions. This process is in line with island nucleation on a flat surface. On the other hand, fingers do not correspond

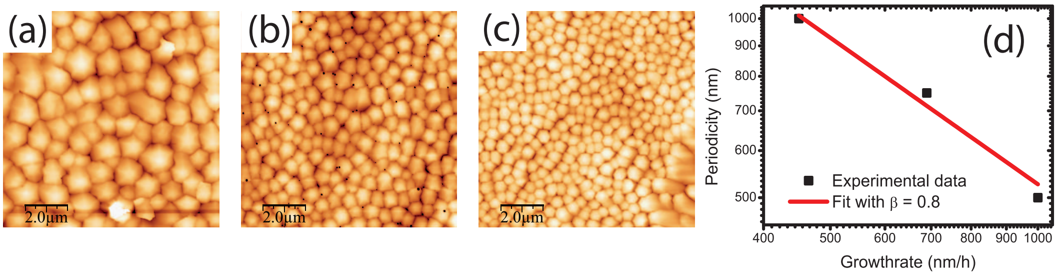

Figure 2.36: 10x10 μm^2 AFM images of GaN mounds grown by NH_3-MBE at 800°C with a V_{gr} of (a) 440 nm/h, (b) 690 nm/h and (c) 1000 nm/h. (d) The lateral feature size is plotted over the growth rate, the fit gives a scaling factor β of 0.8.

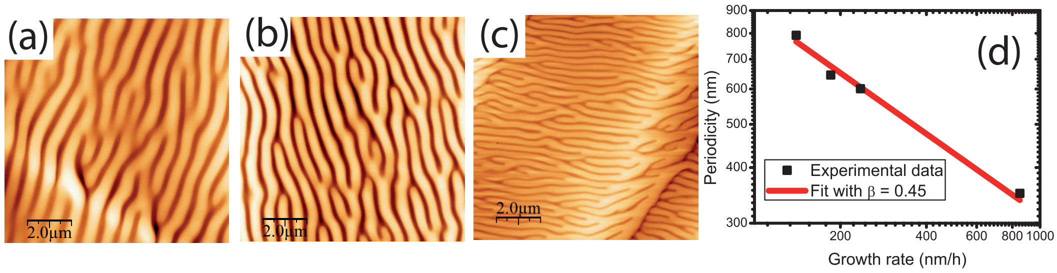

Figure 2.37: 10x10 μm^2 AFM images of GaN finger grown by MOVPE at 840°C with a V_{gr} of (a) 140 nm/h,(b) 235 nm/h and (c) 850 nm/h. (d) The lateral feature size is plotted over the growth rate, the fit gives a scaling factor β of 0.45. Note that the sample displayed in (c) was grown with a different Ga precursor (TMGa).

to a 2D but a 1D growth mode, and the mass transport to the fingers comes from the valleys (only along one direction), as indicated in the schematics displayed in the theory part 2.2.1 (Fig. 2.9 and Fig. 2.10). As a consequence of the massflow along two directions as compared to one, a larger scaling factor is expected for the hillocks. In fact, the scaling factor measured for the finger structures grown on FS GaN (Fig. 2.37) is roughly half of the one obtained for the hillocks: a scaling factor β of 0.45 is deduced for the step-meandering regime.

One the one side, this scaling factor is close to what has been predicted for step-meandering for a SESE in the cubic system ($\beta = 0.5$) [88, 83]. Contrary to that, a KESE seems less likely, for which a scaling factor of 0.25 was predicted (for a cubic system) [83, 89]. However, both values can vary depending on the model [67]. Consequently, this should only be taken as a weak indication of a dominant SESE, until further investigations (e.g. by STM) and simulations of a hexagonal system have been performed.

On the other hand, there are further indications which are consistent with a KESE. If the KESE is dominating, and thus mainly responsible for the morphology, the kink density and the crystallographic orientation of the offcut direction would be important. To the author's knowledge, no study of the kinetic morphology as a function of the offcut orientation has been published so far for GaN grown on *c*-plane. However, for *m*-plane GaN grown under nitrogen-rich conditions by PAMBE, a strong dependency of the morphology on the crystallographic orientation of the offcut has been observed [122]. In this case, it was possible to obtain a smooth classical step-flow morphology with an offcut that was 17° off from the c-direction. Otherwise, the surface was wavy. While the authors attribute this effect to a certain bond configuration at the step-edge [122], their results are in good agreement with a KESE. Without this special offcut orientation, a trilayer of Ga at the growth front is needed for achieving smooth surfaces [123]. For MOVPE an offcut angle of over 5° is required to achieve smooth steps for *m*-plane [124].

To briefly summarize the discussion between KESE and SESE, the scaling of the step-meander seems more in favor of a SESE, while the dependency observed for *m*-plane GaN hints that a KESE might also play a role. Further investigation is needed. This could be done by systematically growing on surfaces with different offcut orientations. However, as both barriers are likely to be present at the same time, the main question remains unanswered: which of the two is dominant (and under which conditions)?

2.5.2 Avoiding the ESB-induced instability

In most of the cases, the kinetic morphology should not only be controlled, but avoided, as it can lead to rough interfaces. There are two possible ways to keep a smooth surface in the presence of an ESB: the uphill masscurrent which result from the ESB could be countered, or the asymmetry of attachment could be circumvented by providing another diffusion channel over the step-edges.

Circumventing the ESB and the ESB-induced morphology

When growing at high T_{gr}, the energy of the particles on the surface is high compared to the ESB, hence they do not experience a strong asymmetry. This is the case for a high T_{gr}, where classical 2D layer-by-layer growth or 1D step-flow growth is possible. This corresponds to growing in the right hand part of Fig. 2.34 (area III). As an example from another materials system, it is possible to avoid hillock formation in Ge when growing above 170°C [74].

As discussed in the previous part, V_{gr} can have two effects: first, smoothening effects can become dominant at low V_{gr} and can lead to a vanishing of the ESB-induced morphology despite a pronounced asymmetry of attachment. This takes place by countering the uphill masscurrent induced by the ESB. A countering downhill massflow could originate from e.g. hydrogen etching or desorption, which could be higher for the convex parts of a step-edge. Note that the smoothening effects should depend on the temperature and might not be significant at low T_{gr}. Second, increasing V_{gr} can also reduce the effective diffusion length. A very high V_{gr} could lead to a transition between 1D and 2D nucleation.

Another parameter is the offcut. For a SESE, the offcut will affect the 2D to 1D transition. If no smooth step-flow growth can be maintained, then increasing the offcut could result in fingers and prevent hillock formation. It might be easier to smooth a 1D finger regime than the hillock regime. In the case that a KESE is dominant, the offcut orientation affects the density and configuration of kinks along the step-edges as well as the step-edge configuration. Step-meandering due to KESE should therefore also be controlled by the offcut orientation, which may allow getting rid of a kinetic morphology by adjusting the offcut.

Note that the effect of the V/III ratio was not investigated here. For NH_3-MBE grown layers, no strong impact of the NH_3 flux was observed, but it would be interesting to evaluate the effect of the V/III ratio in more detail in a further study, as it affects the surface chemistry. Another factor is the impact of the morphology of the underlying layer when growing on top of a different layer. The local offcut is no longer controlled by the offcut of the substrate, but depents on the morphology of the layer underneath. This issue will be discussed more detailed in part 2.6.1.

Screening of the ESB: effect of a metal adlayer

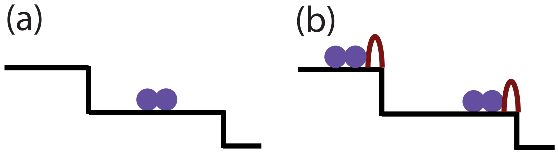

Figure 2.38: Nucleation at very low diffusion length (a) without an ESB and (b) with an ESB.

On the other hand, it is also possible to screen the ESB by avoiding the asymmetry. As a consequence, the step-flow growth mode is sustained, and the 2D to 1D growth mode transition does not occur earlier. This allows to broaden the range of growth parameters which can be used while keeping a classical step-flow morphology. A way to achieve this situation is to use another diffusion channel, where the particles do not experience the ESB and thus avoid the asymmetry.

A prominent example of such a diffusion channel is a metal adlayer. Such a metal adlayer is commonly used in PAMBE under metal-rich conditions and allows keeping a smooth morphology at very low T_{gr}. To be more precise, the best GaN surface morphology is obtained when a bilayer of metal is present at the growth front for *c*-plane orientation. To discuss this in more detail, the first report of an ESB in GaN should be mentioned again, as the study by Zheng *et al.* provides additional information here: Zheng *et al.* [94] grew a sub-monolayer of GaN at very low temperatures by PAMBE. A template with growth spirals was used to prepare a surface with step-edges of single and double layer height. T_{gr} was strongly reduced so that the diffusion length was not sufficient for step-flow growth anymore and island nucleation occurred on the steps. The position of the nuclei was then studied by *in situ* STM. First, the effect of an ESB on the island nucleation on such kind of steps needs to be explained: the step-edges act as preferential nucleation sites, *i.e.* all adsorbed particles that can reach those will nucleate there. Island formation will thus start in the region that is furthest away from an

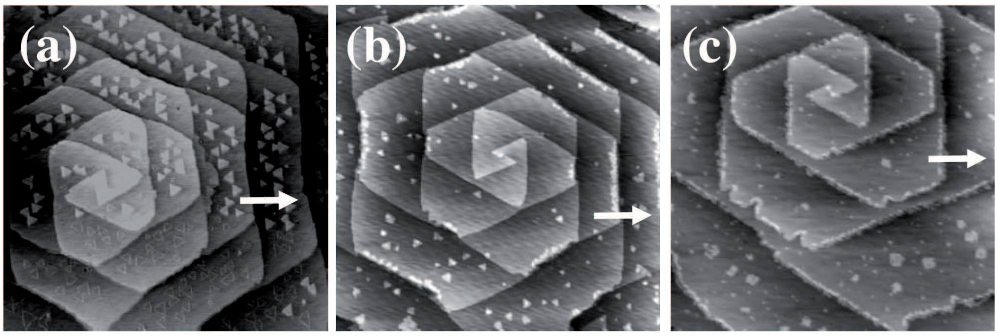

Figure 2.39: The original STM images for a sub-ML of GaN deposited on a spiral at very low T_{gr}, taken from Zheng *et al.* [94]. (a) With a bilayer of Ga at the growthfront, (b) with a single layer of Ga at the growth front and (c) without Ga at the growth front under nitrogen-rich conditions.

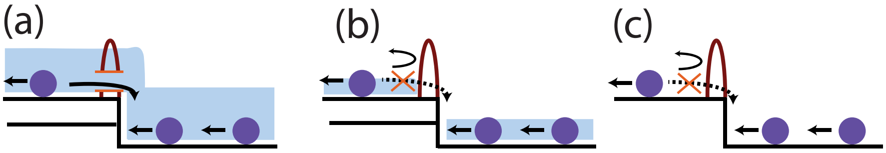

Figure 2.40: Schematics of the screening of the ESB by the presence of another diffusion channel: (a) the adlayer is high enough to allow a diffusion over the step-edge for a double layer step, (b) the adlayer is not high enough for a double layer (only for single layer), hence no additional diffusion channel for double layer, but surface diffusion might be affected, and (c) the case without an adlayer.

accessible step-edge. Without an ESB (or with a screened ESB), both step-edges are accessible and nucleation takes place in the center of a step (Fig. 2.38 (a)). When introducing an ESB, the nucleation position shifts (depending on the strength of the barrier) towards the lower step-edge, as illustrated in Fig. 2.38 b. As a consequence, the position of the nuclei with respect to the step-edges allows to probe the existence of an ESB. The original STM images from Zheng *et al.* [94] are shown in Fig. 2.39. Under metal-rich conditions with a bilayer of Ga at the surface, as seen on the left, the island nucleate in the center of the steps, hence no ESB is observed. On the other side, for nitrogen-rich conditions (no Ga adlayer), as displayed on the right, the nucleation takes place close to the downward step-edge, which is a clear evidence of an ESB.

However, the most interesting case is one in the middle, where both can be observed, depending on the step-height: a single ML of Ga screens the ESB for single steps only. It is not sufficient for double steps. This STM observation needs to be discussed in the context of the surface morphologies reported for metal-rich PAMBE growth. The best GaN morphology is obtained for a homogeneous Ga film surface-coverage. For *c*-plane GaN, the ideal film thickness is two ML and further Ga leads to droplet formation [60]. Note that for other crystallographic orientations, the optimum thickness can vary, e.g. three ML for *m*-plane GaN [124] and for cubic GaN a single ML seems optimal [125].

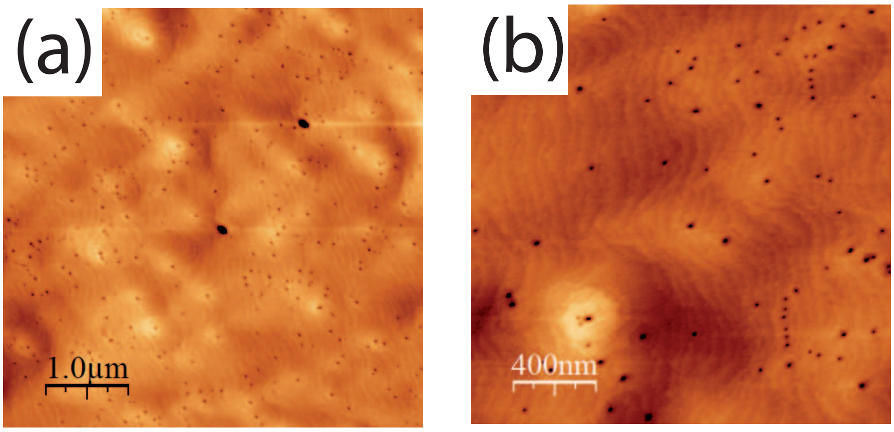

Figure 2.41: (a) 5 x 5 μm^2 and (b) 2 x 2 μm^2 AFM images of PAMBE GaN grown under metal-rich conditions at 740°C. No mounds but smooth steps are observed, and dislocations are easily visible. Note that only one ML of Ga was needed at the growth front, as the sample exhibits only step-edges of single layer height.

It has been postulated that such an adlayer reduces the diffusion barrier on the surface (thus enhances the diffusion length) and provides a preferential diffusion channel [126]. This diffusion channel should allow a downwards diffusion over a step-edge without experiencing an ESB if there is a continuous film. In the case of a single ML of Ga at the growth-front, the ESB is only screened for step-edges of single ML height. A bilayer of Ga is needed to screen the ESB for step-edges of double ML height for *c*-plane GaN [94]. This interpretation makes sense: the single ML of Ga does not provide a continuous film over the double step-edge, hence particles still experience the ESB there, as presented schematically in Fig. 2.40.

As GaN commonly forms step-edges of double ML height, this explains why the bilayer of Ga is needed to screen the ESB and thereby allows to realize smooth step-flow growth at the low temperatures used for PAMBE. This demonstrates that a metallic Ga film of the height of the step-edges is one possibility to screen the ESB. In turn, it allows to connect the origin of the smooth morphology of metal-rich PAMBE growth grown at low T_{gr} to the screening of the ESB on a microscopic level. To investigate this further, metal-rich GaN was grown using PAMBE at 740°C (Fig. 2.41). A smooth step morphology is obtained (the rms surface roughness is 0.8 nm for 5 x 5 μm^2). Note that only a single layer of Ga was present at the growth front, as the sample grown exhibits steps of single ML height.

Other adatoms are likely to provide a similar diffusion channel as well as positively affect the diffusion length [126]. In the case of Ge for instance, the ESB-induced breakdown of LT Ge film can be avoided by supplying a low level of Sn [92]. Similarly, GaN grown by NH_3-MBE at low temperature (660°C) normally exhibits a very rough surface morphology (Fig. 2.42 (d) - (f)), but it can be brought back to a high temperature morphology when additional indium is supplied during growth (Fig. 2.42). In the latter case, the In flux even allows to achieve a step-meandering growth on the sidewalls of the underlaying Ga mounds (Fig. 2.42 (g)-(l)), which self originate from an underneath GaN buffer grown at 800°C (Fig. 2.42 (a)-(c)).

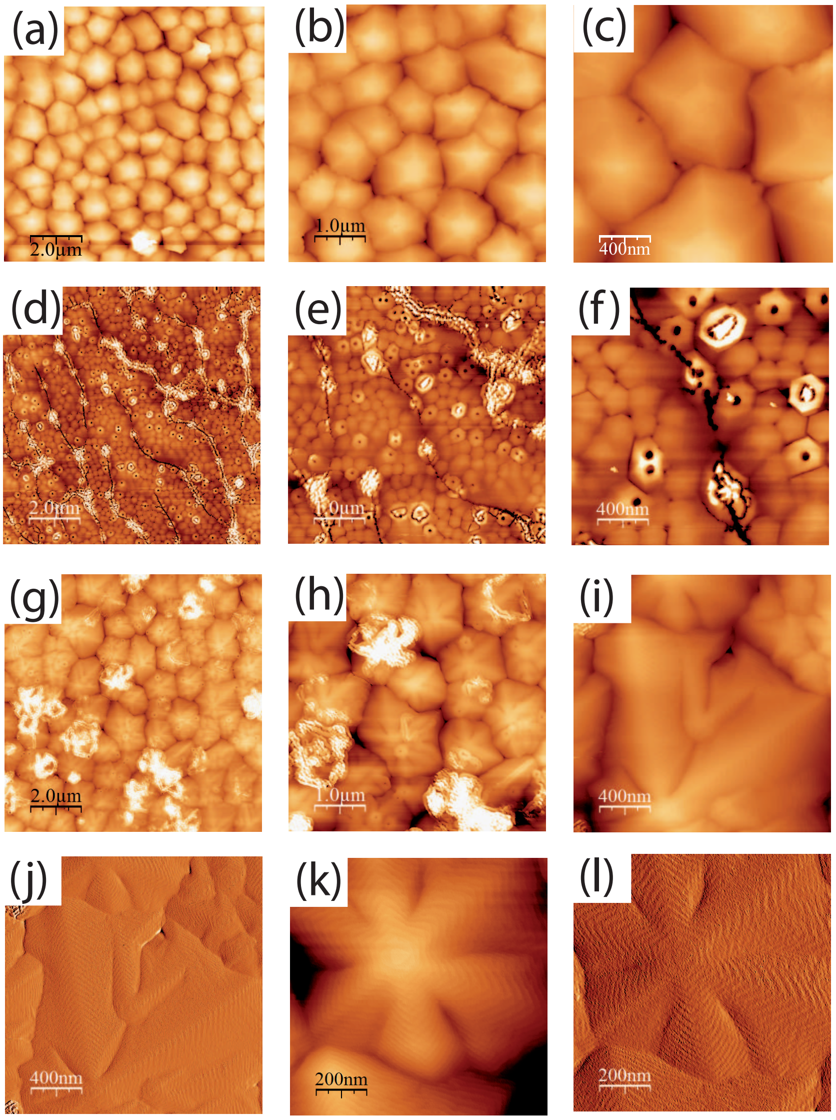

Figure 2.42: 10 x 10, 5 x 5 and 2 x 2 μm AFM images of GaN layer grown at (a)-(c) 800°C, (d)-(f) 660°C and (g)-(i) 660 °C with additional supply of In. In (j)-(l), a 2 x 2 μm AFM image and two derivatives of AFM images are displayed for additional information about the indium-surfactant effect.

Note that the same buffer was also used for the sample without In. The transition from rough to step-meandering can be interpreted as an In-enhanced diffusion, or a surfactant effect. One should point out that adatoms can not only enhance but also reduce the diffusion length [127]. This is the case of Mg as proved by a reduced finger size compared to an undoped reference sample (Fig. 2.43).

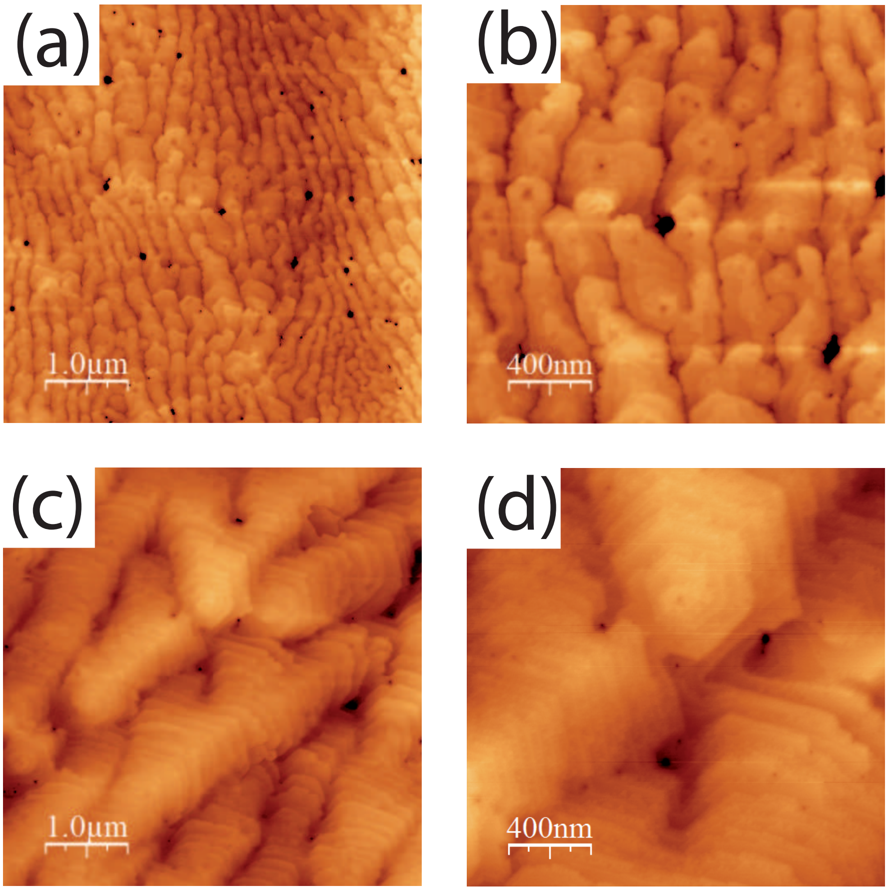

Figure 2.43: 5 x 5 and 2 x 2 μm AFM images of GaN grown at 865°C (a)-(b) with additional Mg and (c)-(d) without Mg. A strong reduction of the lateral feature size can be observed for the sample with the additional Mg flux.

Screening of the ESB: influence of the carrier gas

In the case of MOVPE, the composition of the carrier gas (either H_2, N_2 or a mixture of both) has a certain effect on the surface morphology. All the LT MOVPE GaN layers presented so far were grown under pure N_2 as carrier gas, which corresponds to growth conditions used for QWs and barriers in the active region of optoelectronic devices. Pure N_2 is especially important for indium-rich InGaN alloys, as H_2 strongly reduces the indium incorporation [128], and thus needs to be avoided. For high temperature GaN, as shown in Fig. 2.3, H_2 leads to the best growth conditions [129]. H_2 may affect the surface by etching it during growth, but this etching is supposed takes place only at high temperatures [130]. If etching occurs, it could provide a smoothening effect that counters the ESB-induced massflow.

However, it has been suggested that the presence of H_2 changes the local growth front composition from nitrogen- to more metal-rich conditions [130]. The processes at the growth front can be described by two equations. The first process is the adsorption of Ga, which can be described in form of a reversible process by

$$Ga + (ads) \Leftrightarrow Ga(ads), \tag{2.8}$$

with (ads) an adsorbance site and $Ga(ads)$ the Ga adsorbed at the surface. The adsorption process is strongly temperature dependent and rather slow. On the other hand, the interaction of the adsorbed Ga with NH_3 to form GaN given by

$$Ga(ads) + NH_3 \Leftrightarrow GaN + 1.5H_2, \tag{2.9}$$

is a very fast quasi-equilibrium process and changes only slowly with temperature. The latter equation (Eq. 2.9) describes the “bulk - adsorption layer” interaction [130]. For this process, the presence of additional H_2 shifts the balance of this (quasi-) equilibrium towards the left side, which means having a partial Ga adlayer at the growth front as long as H_2 is supplied: under the presence of H_2, a stable Ga coverage of around half a ML is expected from simulations for a broad range of temperatures [130]. If the theory is correct, using H_2 in the carrier gas could provide a partial metal-adlayer at the growth front, similarly to the metal-adlayer used in PAMBE. In Fig. 2.44 two LT GaN layers grown on FS GaN by MOVPE are presented. While a clear step-meandering morphology is observed when N_2 is used as carrier gas, a perfectly flat and regular step-flow morphology is visible in the case of H_2. This is a clear indication that the carrier gas has a strong effect on the ESB. While it does not prove the theoretical predictions, these observations support the general idea. There are further indications that the presence of H_2 enhances the lateral diffusion and makes the growth front more metal-rich. The case of MOVPE-grown N-polar nanowires (NW) also supports this interpretation: without H_2 in the carrier gas mixture, hexagonal hillocks form. H_2 is required for the NW formation [131, 132] and increasing the H_2/N_2 ratio strongly decreases the NW diameter until a plateau is reached (for a ratio of 1.25). This means that additional H_2 in the

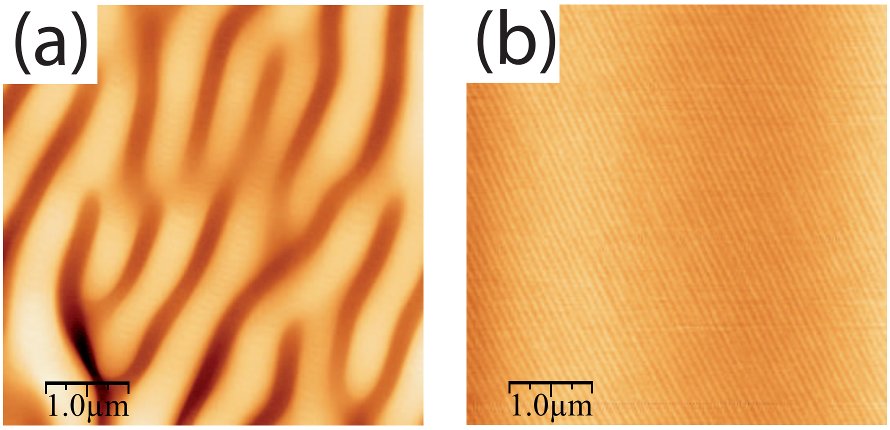

Figure 2.44: 5 x 5 μm AFM images of GaN grown by MOVPE at 840°C: (a) with N_2 as carrier gas and (b) with H_2 as carrier gas.

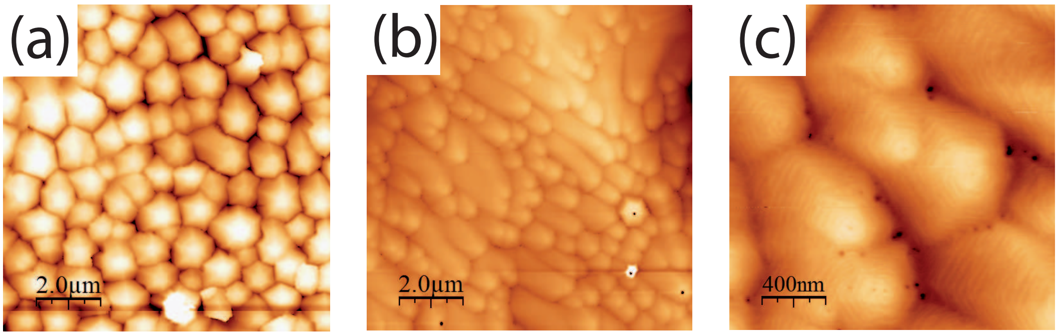

Figure 2.45: 10 x 10 μm AFM images of NH_3-MBE GaN grown at 800°C (a) without and (b) with the addition of a H_2 flux. A magnification of the sample with H_2 is shown in (c). Note that apart from the finger-like morphology, several hillocks are visible with H_2; those hillocks nearly all terminate with a (screw) dislocation.

carrier gas mixture does not further affect the lateral V_{gr}, indicating that H_2 might lead locally to metal-rich conditions.

For the sake of comparison, NH_3-MBE GaN has been grown while supplying additional H_2 *via* the plasma line (without a plasma). The surface morphology of such a sample and that of a reference sample (both grown at 800°C) are displayed in Fig. 2.45. While a transition from a hillock (Fig. 2.45 (a)) to a finger-like morphology (Fig. 2.45 (b)) can be observed, it is accompanied by the creation of mounds that disrupt the finger propagation and terminate in a dislocation. This indicates the presence of screw dislocations. The transition shows that H_2 seems to slightly enhance the diffusion length for MBE growth as well.

To briefly summarize, it seems that H_2 slightly enhances the diffusion and lowers or screens the ESB, possibly with a similar process as the complete metal adlayer does or by providing a downhill masscurrent due to etching that could counter the ESB-induced massflow.

2.5.3 Overview and outlook: how to control the morphology of GaN epilayers

Knowing the origin of the surface morphology features allows a precise control of the growth. The type of morphology - hillocks, step-meandering or step-flow - could in principle be selected by choosing appropriate growth conditions for all three growth techniques.

The type of feature can be controlled by the step width over diffusion length ratio, which determines if the growth is 2D (ESB-induced hillocks) or 1D (ESB-induced fingers). The lateral feature size can be controlled by the effective diffusion length (e.g. in form of T_{gr} or V_{gr}), while the peak-to-valley ratio (the surface height modulation) depends on the growth thickness. This means that both parameters are independent of each other.

Keeping in mind that this control is not always possible, the growth parameter will be limited by the intended structure and growth technique. For some applications, especially LDs, it is important to keep smooth interfaces, hence classical step-flow mode without ESB-induced instability must be preferred. This can be achieved either by growing in a specific growth window (Fig. 2.34) where the classical step-flow mode is maintained due to dominant smoothening effects, or by screening the ESB and thus avoiding the asymmetry of attachment. The latter can be done by a metal adlayer, which allows to extend the classical step-flow growth window to low T_{gr} or high V_{gr}.

On the other hand, the control of the kinetic morphology could be useful. For instance the step-meandering patterns may create an ordering along the offcut direction or a matrix to promote self-alignment of QDs. While aligned QDs commonly rely on *ex situ* nano-patterning, it is has been demonstrated that homoepitaxial grown meandering features can be used for alignment of Ge QDs on meandered Si [133]. The kinetic morphology can also be used to play on the properties of an InGaN overlayer. It will be shown hereafter that the local surface misorientation modifies the In incorporation and introduces thereby significant alloy disorder. In turn, this may enhance the carrier localization and therefore improve the efficiency of LEDs.

2.6 The effect of the ESB on devices

In this part, the effect of the ESB-induced morphology on the subsequent growth of an active region of a LED will be investigated. The correlation between local surface morphology, indium incorporation, and position of defects will be discussed. An improvement in quantum efficiency will be demonstrated on LEDs.

2.6.1 The effect of the ESB on the lateral emission characteristics

The ESB-induced step-meandering appears for common barrier growth conditions and should be found in many optoelectronic devices. This patterning causes local variation in step-width and step-orientation and it further creates local film-thickness variations. The latter can be especially relevant for very thin layers. Both can have a profound impact on devices. In

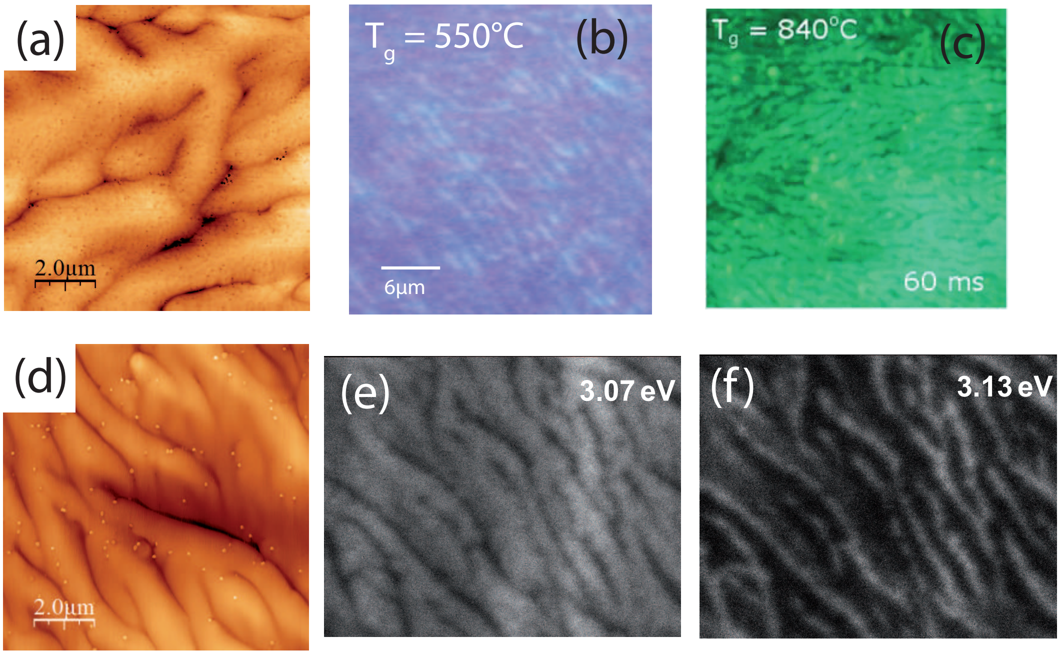

Figure 2.46: In (a) a 10 x 10 μm^2 AFM image of a NH$_3$-MBE InGaN QW grown on a HT GaN which exhibits a finger morphology is displayed. In (b) the fluorescence image of the same sample under high excitation power displays the finger structure related emission. In (c) the fluorescence image of a MOVPE grown MQW also displaying such a emission pattern is shown as a comparison, taken from Masui *et al.* [134]. In (d) a 10 x 10 μm^2 AFM image of a MOVPE grown DQW is displayed with the corresponding cathodoluminescence intensity maps for different emission energies shown in (e) and (f) indicating higher and lower indium contents. (d)-(f) are by courtesy of S. Sonderegger (EPFL).

particular, when the InGaN active region is grown on a finger-like structures, this morphology can be transferred to the lateral emission characteristics of the device, thus aligning the optical properties and the ESB-induced surface features.

To investigate this in more detail, a pronounced finger-morphology GaN buffer was grown by NH$_3$-MBE with an In-rich InGaN QW and a 30 nm GaN cap layer grown on top. The surface morphology of the sample is displayed in Fig. 2.46 (a). Investigating the sample by fluorescence measurements (Fig. 2.46 (b)), a clear stripe like structure can be resolved. In an earlier study, Sonderegger *et al.* [103] already showed by cathodoluminescence that the region between the finger (valleys) exhibits a blue-shifted emission compared to the region on top of the fingers for an MOVPE grown QW, as shown in Fig. 2.46 (d)-(f). The authors proposed that this change originates from thinner QW areas in the valleys [103]. However, it could also be that the local variation in the offcut angle around the valleys affects the indium incorporation. Indeed, it has been reported that local offcut variations cause variations in indium content and thus emission wavelength [54]. A more detailed study of the dependence of the indium incorporation on the offcut angle has been published recently for both MOVPE [101] and PAMBE [135]. Furthermore, this effect has already been demonstrated in a LD using

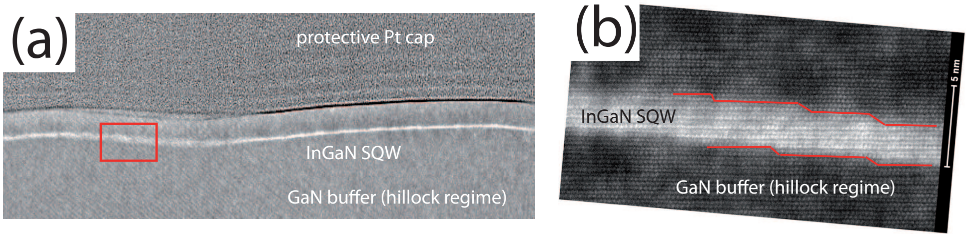

Figure 2.47: HR-TEM images of a single InGaN QW grown on a mound-regime buffer by NH_3-MBE: (a) The QW follows well the morphology of the underlaying GaN mounds. (b) magnification shows the steps of the underlaying GaN, which creates the local offcut experienced by the InGaN layer.

a prepatterned substrate: a shift in emission wavelength for LD stripes grown on different offcut regions on the same wafer was observed [101, 136], with the indium incorporation being higher for lower offcuts, which corresponds to the top regions on the finger structures. This agrees well with the emission energy observed by cathodoluminescence [103].

Furthermore, an optical pattern which resembles step-meandering morphology has also been seen by fluorescence spectroscopy for MOVPE grown MQWs [134], with a brighter emission observed for the fingers (Fig. 2.46 (c)). However in that study, the emission pattern of the MQW structure was not stable under TA. This is in good agreement with a slight homogenization of the indium content upon annealing, which will be discussed in more detail in the next chapter. Finally, an InGaN QW grown in a layer-by-layer mode on a hillock morphology has been studied by HR-TEM in this work (Fig. 2.47). Under these conditions, no variation in the QW thickness was observed. Therefore it is more likely that the variations in emission wavelength originate from a local offcut dependent indium incorporation, but this may depend on the growth mode of the QW itself. A flatter surface can correspond to an increased V_{gr} of the step-edges, and thus might reduce indium desorption.

Summarizing this part briefly, an alignment of the emission wavelength and intensity with the finger pattern can be observed. While this correlation has been previously attributed to variations in the QW thickness, it is more likely to originate from a slight dependence of the indium incorporation on the local surface misorientation.

The role of the buffer layer morphology for MBE grown QWs

The standard GaN buffer layer for NH_3-MBE is grown in the hillock regime. However, as demonstrated in part 2.3.2, it is also possible to obtain a smoother GaN buffer with finger morphology when T_{gr} is increased. A higher In content should be obtained for flatter finger morphology and the homogeneity of an subsequently grown InGaN layer should be improved, as it depends on the regularity of the misorientation. A reduction in the PL linewidth and a redshifted emission energy are therefore expected for QWs grown on a finger-like buffer layer. The surface morphologies and PL spectra of QWs grown with the same nominal In flux on

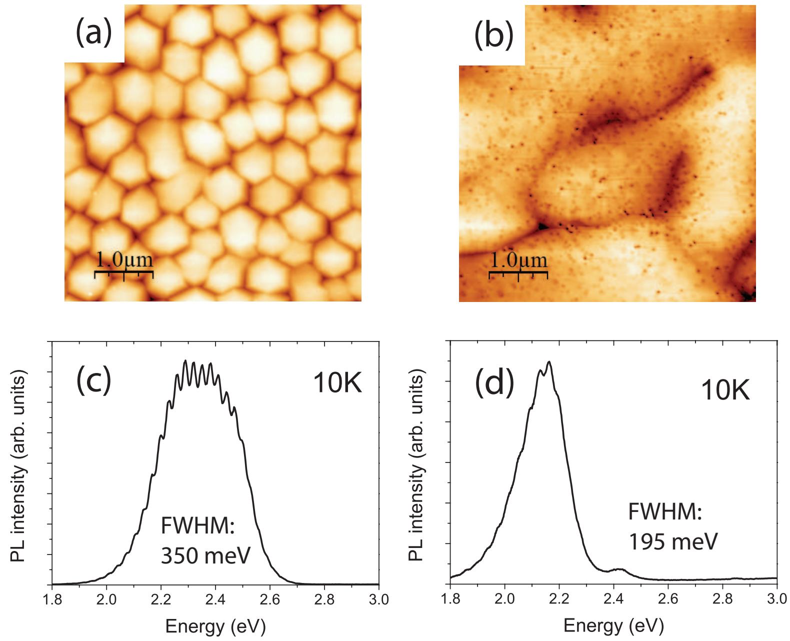

Figure 2.48: 5 x 5 μm^2 AFM images of QWs grown on (a) a hillock morphology GaN buffer and (b) a finger morphology GaN buffer. Their corresponding PL spectra are shown in (c) and (d).

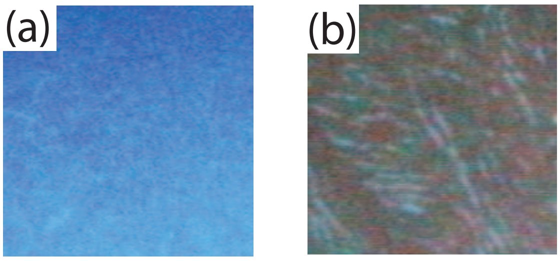

Figure 2.49: 30 x 30 μm^2 RT Fluorescence maps, recorded under high excitation power, of the InGaN QWs grown on top of (a) a hillock and (b) a finger morphology GaN buffer.

GaN buffer with the two different surface morphologies are displayed in Fig. 2.48. A hillock morphology is observed when the GaN buffer is grown at 800°C in (a) and a finger morphology for the GaN buffer grown at 865°C in (b). The corresponding 10K PL spectra are displayed in (c) and (d). The linewidth is reduced and the QW emission is at a lower energy for the sample grown on the smoother finger morphology. This agrees well with higher In incorporation and a more homogeneous In distribution. One particularity that should be mentioned is that there is a slight second peak visible at around 2.4 eV for the sample grown on the finger morphology, which vanishes quickly when the PL temperature is increased. This transition could possibly originate from the region between the fingers (the valleys and sidewalls) where the strong misorientation could locally lead to different indium incorporation. This sample exhibits a finger-like or dendritic pattern, different to the one grown on a standard hillock buffer. In Fig. 2.49, the RT fluorescence maps of both samples are compared: while no features can be observed for the sample grown on the hillock buffer, a clear correlation between the morphology and the QW emission pattern can be seen for the sample grown on finger morphology (as already shown in Fig. 2.46 (b)).

This supports the correlation between the misorientation and the indium incorporation. In addition, it indicates that the broad linewidth of high In content QWs grown by NH_3-MBE is partly due to the buffer layer morphology. Switching to a smoother buffer layer should therefore be beneficial.

Interaction between barrier and QW growth

Smooth buffer layers are especially important for LDs to avoid gain dilution. This is investigated further by studying the morphologies of GaN and subsequent InGaN QWs. Figure 2.50 displays AFM images of the surface morphologies of a smooth HT GaN layer (T_{gr} = 1050°C) grown on sapphire (Fig. 2.50 (a)) and of a 2.5 nm-thick uncapped InGaN QW grown at 840°C (Fig. 2.50 (b)) and at 780°C (Fig. 2.50 (c). The HT GaN morphology exhibits double steps, typical for GaN. The InGaN QW surfaces consist of steps with single ML height, meaning the step-density is twice as high. As the presence of indium at the growth front is known to enhance the diffusion length [137], it is not surprising that it could affect the growth rates of the different step-edges (which are at the origin of the double steps (part 2.3.3)). In addition, surface segregation of In could play a role as well. The double or single step nature should have an impact on the local QW thickness, as schematically described in Fig. 2.51. Note that it can not be excluded that a surface rearrangement during cooldown takes place and affects the measured surface morphology. However, ML fluctuations in the QW thickness have also been observed for capped QWs by atom probe tomography [138]: while a rather smooth lower interface was observed, the upper interface exhibited ML fluctuations, and it has been proposed that these well-width fluctuations affect the carrier localization. More information can be found in the article by Oliver *et al.* [55]. While the change from double to single steps could create such fluctuations in the QW thickness, it would also broaden the

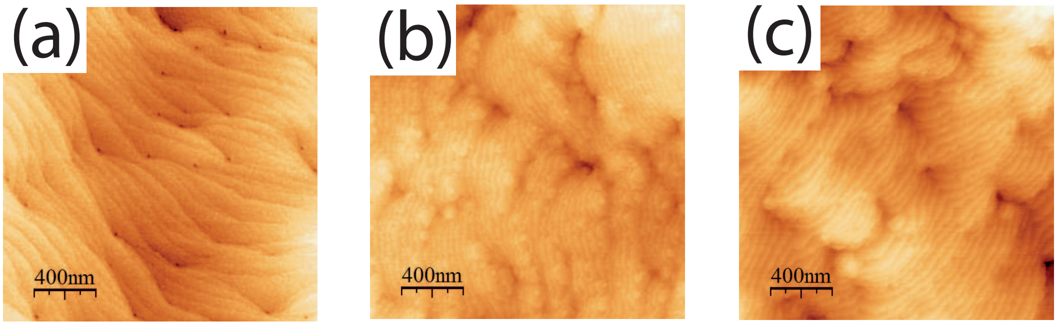

Figure 2.50: 2 x 2 μm^2 AFM images of (a) a typical HT GaN buffer layer and an uncapped QW grown (b) at 780°C and (c) at 840°C.

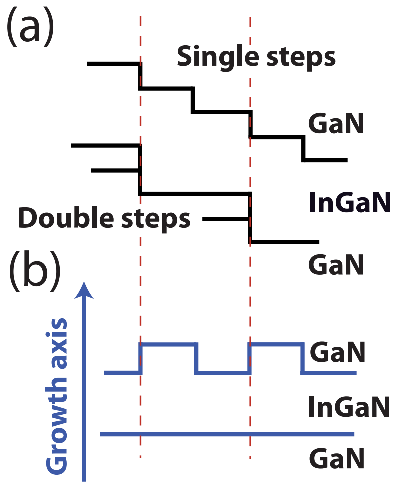

Figure 2.51: Schematics of the effect of different step height between the bottom GaN layer (double steps) and the InGaN layer on top (single steps) on the QW thickness. (a) Side view of the layer and (b) the corresponding QW thickness variation.

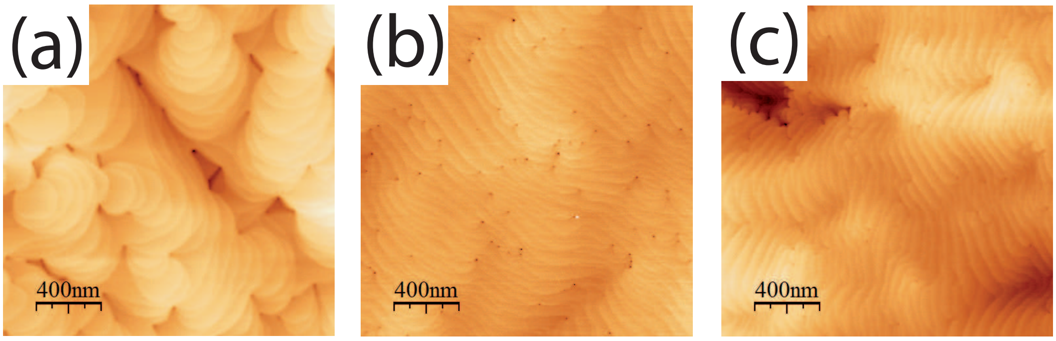

Figure 2.52: 2 x 2 μm^2 AFM images of 10 nm of LT GaN grown at 840°C) on (a) a HT GaN buffer layer and (b) on top of a QW grown at 840°C. (c) is a GaN layer grown at 780°C on top of a QW grown at 780°C.

linewidth slightly. Therefore it could be of interest to investigate the kinetics of the InGaN growth in more detail in a follow-up study.

Note that this investigation is not straightforward. Figure 2.52 compares the surface morphology of a 10 nm-thick GaN layer grown under barrier conditions on top of a smooth HT GaN layer or on top of the InGaN QWs from Fig. 2.50 (b) and (c), respectively. A pronounced meandering with strong dislocation pinning is observed for the sample grown on the HT GaN layer (Fig. 2.52(a)). In contrast, the layers grown under the same conditions with the QW underneath (Fig. 2.52 (b) and (c)) only exhibit a weak meandering and their morphology is far less influenced by the dislocations. This might be due to a combination of indium surface separation or due to a memory effect, as some indium might still be present in the reactor when growing on top of the QWs. A QW can thus be grown on three types of GaN morphology: a LT GaN buffer (Fig. 2.52 (a)), a HT GaN buffer (Fig. 2.50 (a)) or a LT GaN buffer itself already

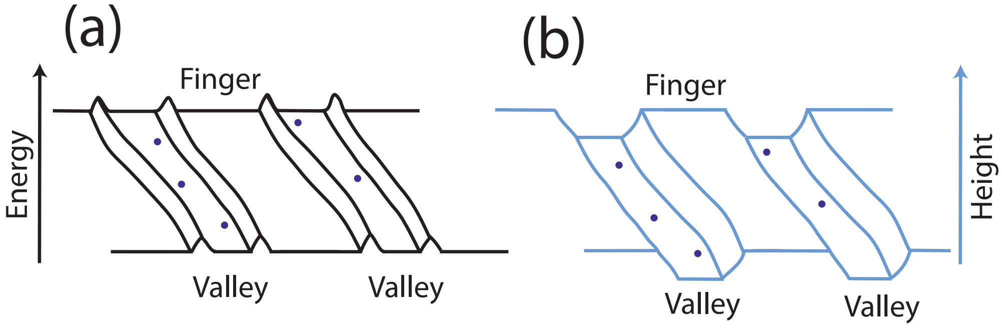

Figure 2.53: Comparison of the surface morphology with the energy profile for finger morphology. Dislocations are represented as dots. (a) the energy landscape (black) of the finger morphology; the valleys are surrounded by regions of higher energy (the slopes). (b) the surface morphology (blue) of the finger structure with the dislocations in the valleys.

on top of a QW (Fig. 2.52 (b) and (c)). This indicates that the morphology of a layer depends on the underlaying one. The influence of the surface morphology on a QW stack and the interaction of the QW growth conditions with the subsequent barriers would be an interesting topic for future investigations.

2.6.2 The effect of the ESB on device performance: self-screening effect

The last major point that should be addressed is how the ESB-induced morphology can affect optoelectronic device performance. As local variations in indium content tends to lead to a broadening of the emission wavelength, a smooth starting surface must be preferred for LDs. Note that TA seems to homogenize the indium distribution in the InGaN QW active region, leading to a vanishing of the finger-related emission pattern [134]. It means that for a complete device structure, the growth of the *p*-type layer might already anneal the active region and homogenize the InGaN alloy composition, and hence reduce the impact of the ESB-induced morphology on the final device. While beneficial for lasers, this actually may reduce the efficiency of LEDs. Indeed the local In composition variations may enhance carrier localization and thereby the internal quantum efficiency. Another important fact arises from the finger morphology: the evolution of the fingers leads not only to indium content variations, but the valleys automatically align to the defects. This alignment is due to the intrinsic nature of the ESB-induced instability: fingers form by a local enhancement of the step-edge growth rate, coming from a lateral uphill masscurrent. This causes this growth regime to be very sensitive to the presence of pinned dislocations, more than the classical step-flow one. The step-meandering finger can not evolve freely in the presence of dislocations: therefore, a pinned dislocation limits the step-edge growth rate in the area close to it, thus forcing the finger pattern to grow around it. As a consequence, the fingers are always between the dislocation terminations, *i.e.* dislocations are always located in the valleys. Combined with the dependence of the indium contents on the local surface misorientation (step-edge

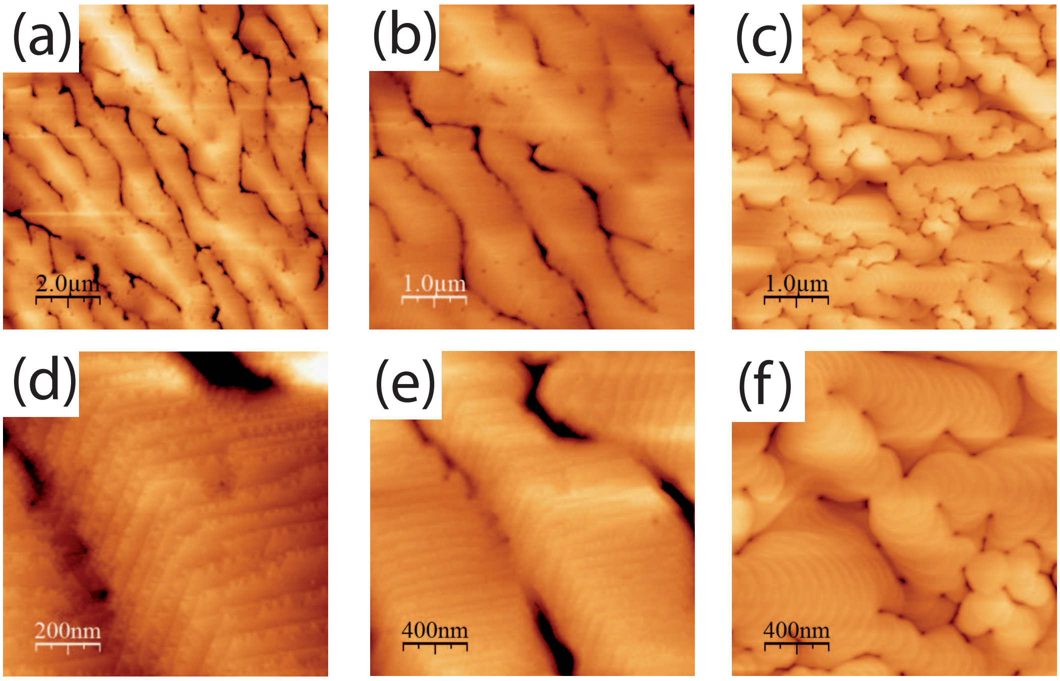

Figure 2.54: AFM images of GaN grown in the finger regime on GaN-on-sapphire templates with a similar dislocation density by MBE and MOVPE. In (a) and (b) a 10 x 10 μm^2 and 5 x 5 μm^2 image of MBE grown GaN is shown. The corresponding 5 x 5 μm^2 image for MOVPE grown GaN is displayed in (c). A clear difference between the interaction of the growth front with the dislocations can be seen. A higher magnification (2 x 2 μm^2 and 4 x 4 μm^2) for the MBE sample is shown in (d) and (e), while a 2 x 2 μm^2 one is shown for the MOVPE sample in (f).

density), this results in a larger bandgap around the dislocations (Fig. 2.53). Excitons are therefore protected by energy barriers, leading to a self-screening effect (SSE), similar to what was proposed for v-pits [46]. This effect is not present for smooth morphologies, where the dislocation are freely accessible. Consequently, non-radiative dislocations are suppressed by the SSE, hence an improved quantum efficiency is expected for a device grown on such a LT GaN buffer.

Before continuing to investigate this in more detail, one of the differences between MOVPE and MBE needs to be highlighted: while the alignment of the finger with the dislocations is pronounced for MOVPE, this is not the case for MBE, as shown in Fig. 2.54. It seems that MBE growth conditions make the growth quite insensitive to dislocation pinning. This could be the reason why it is possible to observe smooth meandering mounds on MBE samples with a high dislocation density, which seems to be difficult for MOVPE grown ones, where screw dislocation induced growth spirals would dominate. A tentative explanation could be a different surface chemistry between the two systems. Nevertheless, the result is that while the indium incorporation seems to be aligned to the morphology for both growth techniques (see Fig. 2.46), only MOVPE growth seems to further align the morphology (and thus the indium

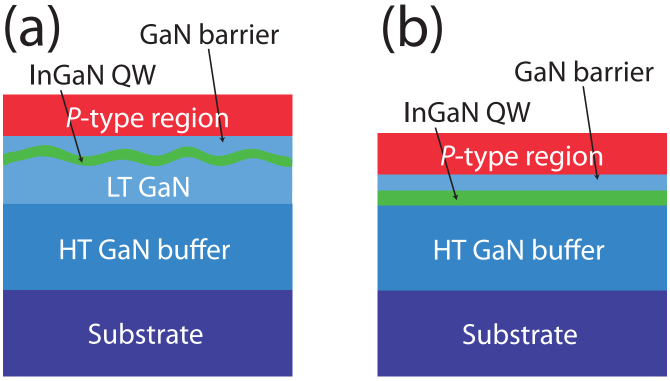

Figure 2.55: Schemata of the simple InGaN single QW LED structure with (a) and without (b) an 50nm LT GaN buffer.

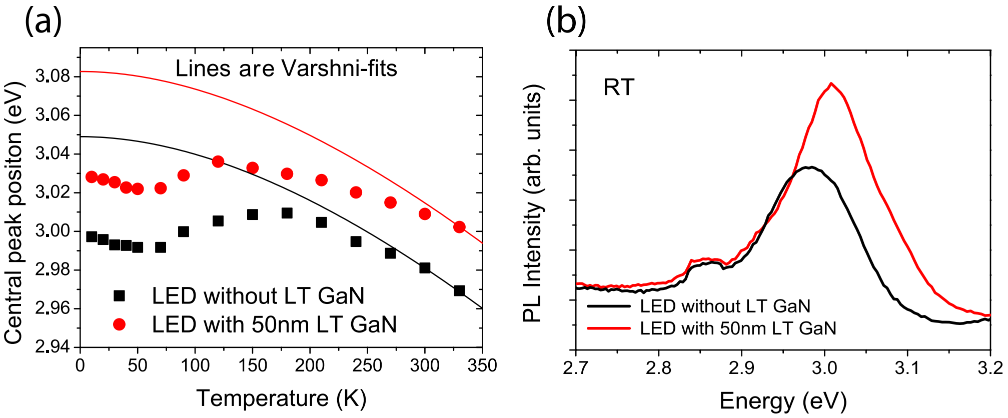

Figure 2.56: (a) The central PL peak position is plotted over the temperature for the LED with and without the LT GaN buffer. The deviation from the corresponding Varshni-fits allows to compare the localization. In (b) the spectra of both LEDs is shown at 330K. Note that a low excitation cw HeCd layer pumping into the GaN was used for these measurements.

distribution) to the dislocations. Thus the screening of dislocations (see Fig. 2.53) should mainly take place for MOVPE samples. To investigate the impact of the surface morphology on the device efficiency, a single QW InGaN LED structure has been grown by MOVPE on either a smooth HT GaN layer, or on a HT layer with a 50 nm-thick LT GaN layer (with finger pattern). A schematic drawing of the structures is displayed in Fig. 2.55. Sapphire was chosen as a substrate, as the dislocation density is high. The shift of the PL peak position for both LEDs displays no major difference in carrier localization between the two structures (Fig. 2.56 (a)). This is not unexpected, as the ESB-induced morphology should not affect the InGaN alloy properties at a local scale when grown on flat surfaces, which dominate the PL spectrum. When looking at the PL spectra of both devices at 300K (Fig. 2.56 (b)), a slight increase in the PL intensity is observed for the LED with the LT GaN buffer underneath. However, the external quantum efficiency, measured by EL, is more relevant for a device. It is enhanced on the LED with the LT GaN buffer layer (Fig. 2.57). This indicates that patterning of the GaN

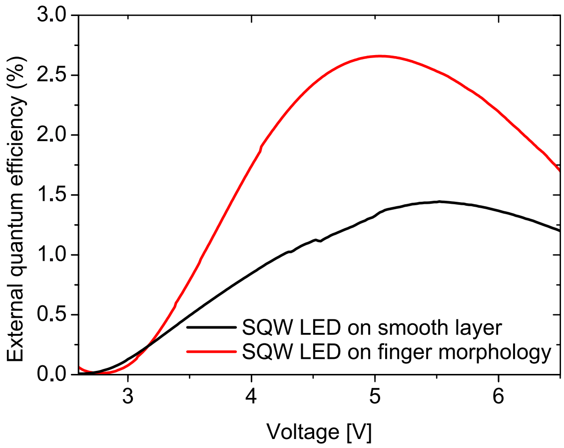

Figure 2.57: External quantum efficiency over voltage for single QW LED structures on a smooth (black) and on a finger structure (red), grown on sapphire. Note that this measurement was performed on-wafer with a calibrated Si photo diode.

buffer below the QW can lead to an improved performance. One may speculate that for some growth conditions the stack of QWs and LT barriers should automatically lead to such an improvement for the upper QWs.

2.6.3 Overview on the effect of the ESB on devices

The morphology introduced by the ESB at the conditions commonly used for the active region of indium-rich devices may have a strong impact on the emission characteristics of the device. The step-meandering morphology of the GaN can be transferred to the light emission pattern, where both a blueshift [103] and a reduction in intensity [134] is observed from the valley region between the finger. This can be explained by a local different indium incorporation. Another possibility for the origin of the different emission wavelength would be local variations in QW thickness. This seems less likely for the QW conditions investigated here. In both cases, the lateral emission characteristic is aligned with the fingers and the emission energy is lower on the finger region. This occurs for samples grown by both MOVPE and MBE.

A second alignment takes place, originating from the intrinsic nature of the step-meandering: the evolution of the fingers is locally limited around pinned dislocations. Therefore, the excitons from the finger region will be protected by SSE, increasing the EQE. There is one important point to make: the interaction of the dislocations with the morphology seems to depend on the growth mode; this is especially different for MOVPE and NH_3-MBE. The step-meandering that appears for MOVPE GaN at (QW) barrier conditions is strongly affected by the dislocations, leading to the alignment of the indium content variations with the dislocations and thus to a SSE. On the other hand, the mound morphology which is commonly observed for NH_3-MBE as well as the finger morphology seem to be independent of the defect density. Indeed, NH_3-MBE fingers interact more weakly with dislocations than MOVPE ones (see Fig.

2.54). As a consequence, SSE is not expected to take place in MBE grown samples. This might be partly responsible for the lower performance of NH_3-MBE grown devices. However, another major difference comes from the different growth conditions of the InGaN layer for the two systems, which gives rise to a difference in point defect density (see chapter 3). All of the presented investigation did not study the growth conditions of the InGaN itself. While InGaN QWs will be treated in the next chapter, the main focus will be on QWs grown in smooth-layer-conditions (in case of the NH_3-MBE samples, RHEED oscillations indicate layer-by-layer growth mode). Nevertheless, it would be very interesting to study both variations in the QW growth regime (such as major changes in T_{gr} or V_{gr}) as well as the effect of the ESB on the InGaN layers themselves in more detail. Together with studying the effects from the growth of subsequential layers (and a potential annealing), such an investigation should allow a deepening of the knowledge about the link between physics and device performance.

3 Indium-rich InGaN quantum wells

MOVPE grown InGaN-based LED devices grown on sapphire or Si can exhibit very high performance, with an internal quantum efficiency (IQE) exceeding 75 % for low indium content active regions [139]. However, as mentioned in the introduction, when the indium content is increased, to achieve green emission, the quantum efficiency drops strongly [13, 15]. Another way to reach green emission could be to take advantage of the internal electrical field in polar QWs: the larger the QW, the stronger the band bending effect and the larger the redshift of the QW emission [140]. However, the electron and hole wavefunction overlap is dramatically reduced, which greatly limits the radiative efficiency [16]. Therefore, thick polar QWs are not suitable for high efficient LEDs in the green range. Actually, the solution on polar surfaces is to keep the small well thickness and to increase the In incorporation. In Fig. 3.1, a simulation of the indium content necessary to obtain a certain wavelength for green LDs with different QW thickness is presented for both polar and nonpolar orientation (taken from Avramescu *et al.* [20]). Note that for non-polar QWs, an even higher indium content is required [20], as the electric field provides no redshift.

The amount of heat brought to a layer after it has been grown is called thermal budget. It depends on both the growth temperature and deposition time of the subsequent layers: the thicker the *p*-side, the higher the thermal budget onto the active region, since *p*-type layers are generally deposited at higher temperatures than those used for QW growth. This thermal budget can lead to degradation of the QWs and therefore to a decrease of the efficiency of the devices. Note that the growth of *p*-type layers is especially crucial for LD structures, since the claddings are thick. In that context, this chapter discusses the issues encountered when InGaN layers are exposed to a thermal budget. Their thermal stability and in particular the point defect formation will be studied in detail. In the first part, MOVPE-grown InGaN QWs are investigated. The second part will discuss the possibility of using NH_3-MBE for indium-rich InGaN QWs.

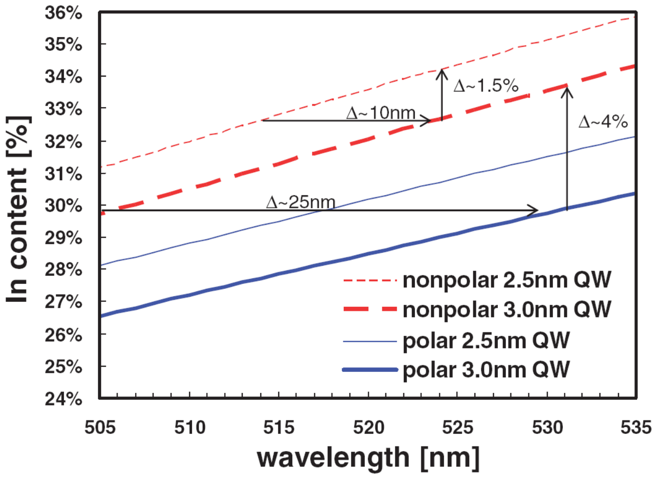

Figure 3.1: Simulation of the indium content and corresponding QW thickness needed for green LDs, taken from [20]. The arrows indicate the effect of thickness or indium content variation or the effect from switching between non-polar and polar orientation.

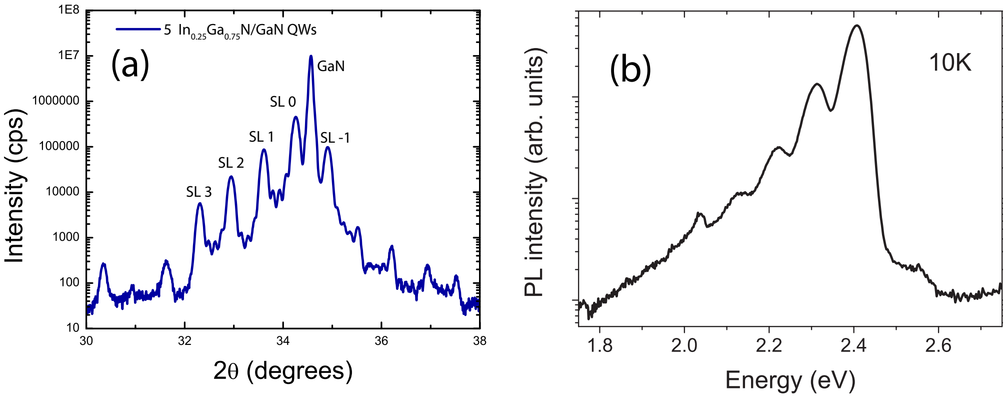

Figure 3.2: (a) XRD measurement of a 5 QW sample performed to extract the In content and the periodicity. (b) the 10K PL spectra of this sample.

3.1 High indium content InGaN QWs grown by MOVPE

3.1.1 Growth conditions for indium-rich QWs by MOVPE

For low indium contents, it is common to ramp the growth temperature of the barrier and use hydrogen, but for high In content, one has to be very careful, as the window to grow In-rich InGaN alloys is rather sharp and needs to be carefully analyzed. The growth temperature needs to be reduced to limit the indium desorption, and H_2 must be avoided, as it strongly reduces indium incorporation [128]. In addition, indium-rich InGaN layers are unstable at high temperatures and T_{gr} needs to be reduced for the barriers as well as for any subsequent layers.

Table 3.1: Parameters of the investigated MOVPE QWs. For series A the horizontal MOPVE reactor was used, while for series B and C a close coupled showerhead reactor was used.

Series	# QWs	T_{gr}	In content	QW thickness	cap layer	substrate
A	5	840° C	15%	2.5 nm	10 nm GaN	sapphire
A	2	770° C	25%	2.5 nm	20 nm GaN	sapphire
A	2	740° C	35%	2.5 nm	20 nm GaN	sapphire
B	2	725° C	40%	1.5 nm	5 nm GaN	sapphire
B	2	725° C	40%	2.5 nm	5 nm GaN	sapphire
B	2	725° C	40%	3.5 nm	5 nm GaN	sapphire
C	1	725° C	25%	2.5 nm	5 nm GaN	FS GaN
C	2	725° C	25%	2.5 nm	5 nm GaN	FS GaN
C	5	725° C	25%	2.5 nm	5 nm GaN	FS GaN

In the following, the InGaN QWs that will be investigated afterwards are presented (see Tab. 3.1). The InGaN layers are grown between 840°C for QWs with 15% In and 725°C for QWs with 40% In, using a V/III ratio of 1170 and 7530. The different V/III ratios originate from the fact that some of the QWs have been grown in the horizontal MOVPE reactor (series A), with a V/III ratio of 1170, and the others in a close coupled showerhead MOVPE reactor (series B and C) with a V/III ratio of 7530.

To analyze these samples, XRD, PL and HR-TEM were applied to probe the QW thickness, indium composition and material quality. For instance, in Fig. 3.2 (a) a typical XRD scan is shown for a MQW with 25% and 5 QWs. The XRD scan indicates a high crystalline quality for this sample with well-resolved superlattice peaks. With this type of measurement the indium content in the QWs and the thickness of QWs and barriers can be extracted. In good agreement with the XRD, the 10K PL spectrum (Fig. 3.2 (b)) shows a narrow linewidth with a FWHM of 51 meV, indicating a very good homogeneity of the indium distribution despite the high indium content and the number of QWs. In addition, LO-phonon replicas of the InGaN QW peak are clearly visible [141], a further indication of a high crystalline quality. QWs grown with similar conditions but with a lower indium content were used in LDs [142, 143] and the performance of these devices attest the material quality. In order to push the LDs further into the green, the thermal stability of the QWs is investigated in the following part.

3.2 Effect of a thermal budget on indium-rich InGaN layers grown by MOVPE

First, the effect of thermal degradation of QWs is treated and the parameters affecting this degradation are studied in order to provide a growth condition window for the layers on top of QWs. In the second part, the interplay between degradation and improvement is studied in more depth. Further insight on the improvement mechanisms will be presented in the study of annealed MBE QWs in part 3.4.

3.2.1 Thermal stability of indium-rich InGaN QWs

To study the effects of the thermal budget, three series of samples were grown:

Series A: 2.5 nm thick MQWs with 15%, 25% and 35% indium, grown on sapphire
Series B: MQWs with 40% indium, with a thickness of 1.5 nm, 2.5 nm and 3.5 nm, grown on sapphire
Series C: 1, 2 and 5 QWs with 25% indium with a thickness of 2.5 nm, grown on FS GaN

Series A allows to study the effect of a different indium content, series B of the QW thickness and series C of different number of QWs (see Tab. 3.1). In addition, comparing samples from series A and C allows to gain information about the effect of the substrate (sapphire and FS GaN, respectively). The growth conditions of the QWs are presented in Tab. 3.1. Note that the sample series B and C have been grown on another MOVPE reactor (a close coupled showerhead reactor), as compared to series A. As a consequence, the temperatures presented in Tab. 3.1 are measured slightly differently (from the backside of the susceptor for series A and from the top for series B and C), and can not be directly compared. The temperature of series A should be reduced by roughly 50°C to be comparable to series B and C. To simulate the growth of the *p*-type layers, the samples were annealed for 2h in an HVPE reactor, under NH_3 atmosphere. Five different annealing temperatures (T_a) were applied for each sample (800°C, 850°C, 880°C, 920°C and 975°C). The samples were investigated optically by low temperature PL, fluorescence and micro-PL measurements. For the low temperature PL measurements, a cw HeCd laser emitting at 325 nm with an excitation power of 2 mW was used, the fluorescence was performed using a pulsed Nd:Yag laser emitting at 355 nm, and for the micro-PL a frequency-doubled Ar laser emitting at 244 nm provided the excitation source. In addition, HR-TEM and XRD were also performed on a degraded sample.

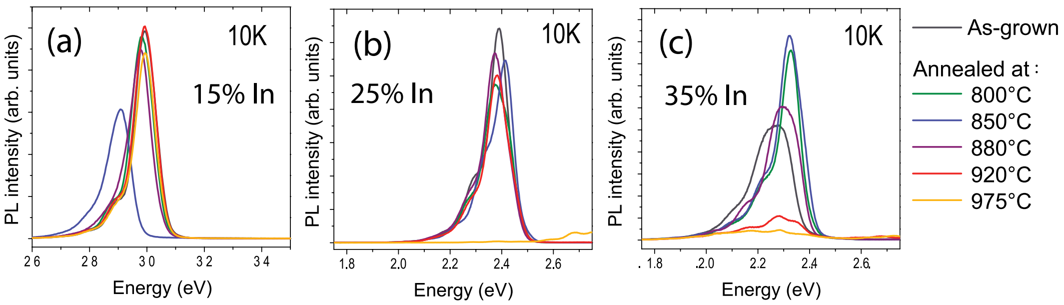

Figure 3.3: The 10K PL spectra of series A with (a) 15% In, (b) 25% In and (c) 35% In.

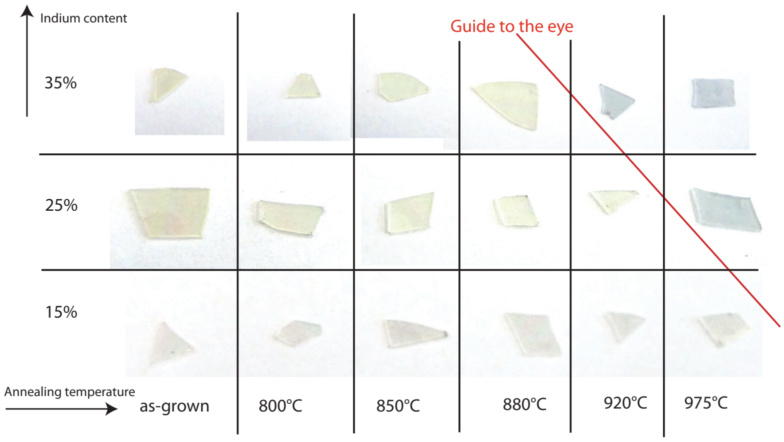

Figure 3.4: Pictures of the as-grown and annealed samples of series A. The as-grown sample with 35% In and the corresponding annealed samples for 800°C, 850°C, 880°C, 920°C and 975°C are shown on top. The same for the 25% In sample is shown in the middle and for the 15% sample at the bottom. A guide to the eye (red line) highlights the change in color, revealing the degraded samples.

Effect of the indium content

Series A was investigated to study the thermal stability against the indium content. First, the sample degradation is identified by the change in its low temperature PL intensity (at 10K). As displayed in Fig. 3.3 (c), for the sample with 35% In, very low PL emission is observed when annealed at 920°C and even less when annealed at 975°C. The sample with 25% In (Fig. 3.3 (b)) shows a strongly reduced PL emission only for T_a = 975°C, while the sample with 15% In (Fig. 3.3 (a)) exhibits no significant reduction in PL intensity for all T_a. Note that one sample with 15% In emitts at a different energy, which might be due to wafer inhomogeneity; this sample is excluded for further investigations. In addition, it should be mentioned that the annealing affects the PL linewith for the sample with 35% In, which will be discussed in more detail later. Apart from PL measurements, the degradation is also visible to the naked eye: the degraded samples appear metallic-like and dark, as can be observed in Fig. 3.4. This change in the sample color seems to go hand in hand with the reduction in the 10K PL signal of the QW

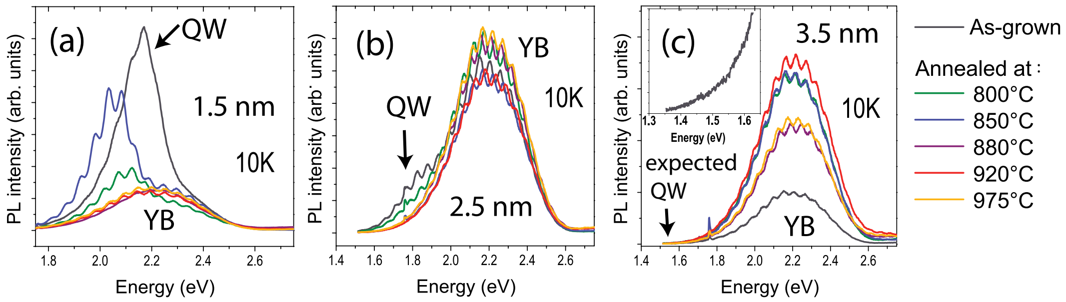

Figure 3.5: PL spectra of series B taken at 10K. (a) 1.5 nm thickness, (b) 2.5nm thickness and (c) 3.5 nm thickness. The inset in (c) shows the as-grown sample for a lower energy range.

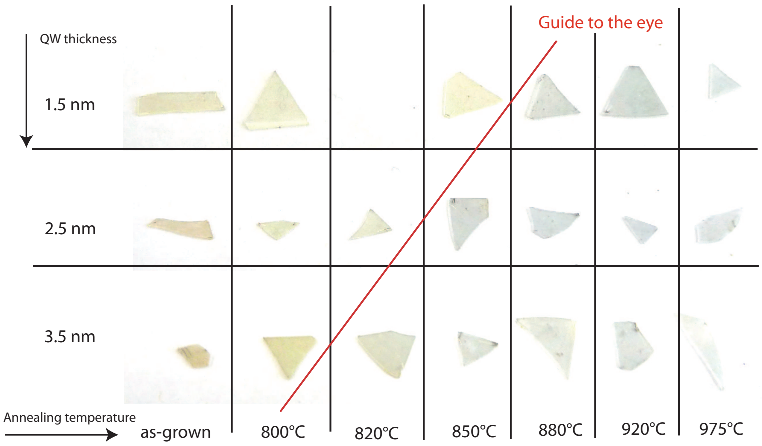

Figure 3.6: Pictures of the as-grown and annealed samples of series B. The as-grown sample with 1.5 nm thickness and the corresponding annealed samples for 800°C, 850°C, 880°C, 920°C and 975°C are shown on top. The same - plus an additional annealing temperature at 820°C - is shown for the 2.5 nm sample in the middle and for the 3.5 nm sample at the bottom. A guide to the eye (red line) highlights the color change, revealing the degraded samples.

emission (see Fig. 3.3). To briefly conclude, the QWs with the highest indium content degrade fastest, which is expected from simple binding energy considerations.

Effect of the QW thickness

To investigate the effect of the QW thickness on the thermal stability, samples with a high indium content (series B) were chosen, as the degradation appears faster. Fig. 3.5 presents the PL spectra of these samples, recorded at 10K. It should be noted that there are two different emissions visible in Fig. 3.5: the intrinsic QW emission (indicated by an arrow) and a broad yellow band around 2.2 eV, which is the so-called yellow band (YB). It is commonly found in GaN and is related to defects in the GaN [144, 145]. The QW emission is shifting towards lower energy with increasing QW thickness (Fig. 3.5 (a) and (b)) due to the quantum-confined Stark effect. For this series B, the yellow band luminescence is strong, and the QW emission, falling within the same energy range, is rather weak. It is only distinguishable for the 1.5-nm-thick sample and faintly for the 2.5 nm one. For the 3.5 nm sample, the QWs should emit at even lower energy; however, no luminescence is observed (see the inset of Fig. 3.5 c). The loss of 10K PL intensity can thus only be evaluated for the 1.5-nm- and 2.5-nm-thick QWs: the PL emission exists until 850°C for the thinner sample and until 800°C for the 2.5 nm thick one. As for series A, a correlation between the degradation and the change in the visual appearance of the QWs is clearly observed. The visual change agrees well with the observations from the 10K PL intensity: thicker QWs degrade faster. This could be due to a larger amount of indium atoms in the QW or due to an increase in the elastic energy, which depends on both the indium content (difference in lattice parameter) and layer thickness.

Effect of the number of QWs

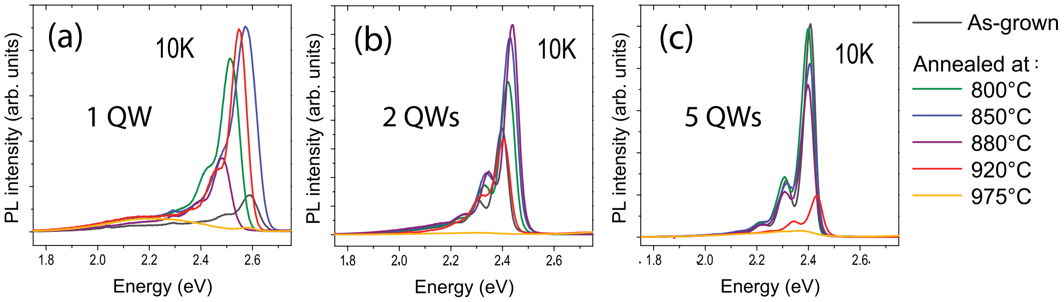

Figure 3.7: PL spectra of series C taken at 10K. The spectra of sample with the single QW are displayed in (a), the spectra for the DQW sample in (b) and the spectra for the sample with five QWs in (c). The indium content is 25% and the QW thickness is 2.5 nm for all samples.

To differentiate between the possible effects of the amount of indium in the QWs and the elastic energy, series C is investigated. The amount of indium in a QW remains unchanged, while the elastic energy increases with the number of QWs. In Fig. 3.7 the 10K PL spectra of the as-grown and annealed samples of series C are displayed. Note that the emission energy is higher for the SQW sample despite nominally the same growth conditions. This might be due to a delayed In incorporation, or slight variations in T_{gr}. The PL intensity is reduced for all samples annealed at 975°C. When annealed at 920°C, the reduction of the PL intensity is stronger for 5 QWs than for 2 QWs. On the contrary, the PL intensity is actually increased for the SQW and slightly less for the DQW sample. In addition, the peak position seems to shift. This will be discussed in part 3.2.4. Nevertheless, when looking at the reduction in the 10K PL intensity, it can be concluded that the number of QWs affects the degradation threshold: more QWs implies a slightly faster degradation. This might be due to the increase in elastic energy.

In Fig. 3.8 pictures of the samples are displayed. Here, it needs to be noted that the link of the changed color with the 10K PL intensity reduction can not be maintained. The change

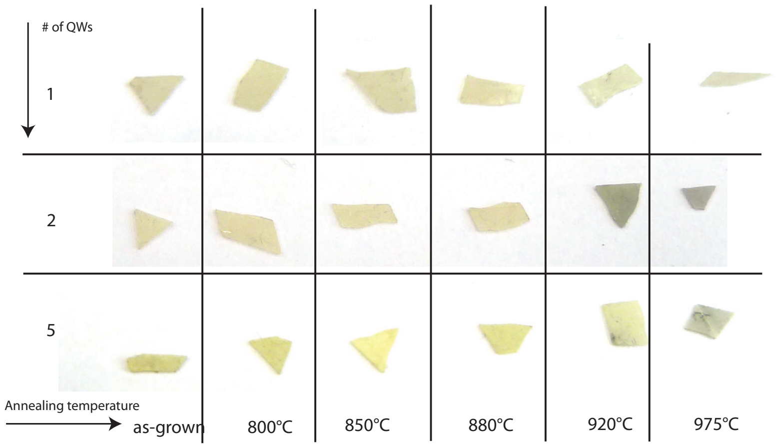

Figure 3.8: Pictures of the as-grown and annealed samples of series C (grown on FS Gan). The as-grown sample with one QW and the corresponding annealed samples for 800°C, 850°C, 880°C, 920°C and 975°C are shown on top. The same is shown for the two QWs sample in the middle and for the five QWs sample at the bottom.

in color appears stronger for the DQW sample annealed at 920°C than for the corresponding sample with 5 QWs, and the degraded sample with 1 QW shows a normal color. This could be tentatively explained by an effect of the TA procedure on the FS GaN.

Parameters that affect the degradation

It is time to take a closer look at the parameters affecting the degradation. An increase in In content, QW thickness and number of QWs all reduce the annealing temperature at which the PL signal degrades. Apart from the binding energy, which depends on the indium content, the elastic energy and the total amount of indium atoms might affect the degradation. In addition, it has been reported that the dislocation density seems to play a role as well [16], but the role of dislocations is discussed later, when the origin of the degradation is treated. Other potential parameters are the homogeneity of the InGaN layer and its growth temperature (see part 3.4). In addition, it has been reported that AlGaN barriers can improve the thermal stability of InGaN QWs [146].

To differentiate between to different parameters investigated so far, they are plotted over the annealing temperature to probe their correlation with the degradation. Fig. 3.9 (a) shows no clear correlation between the degradation of the PL signal and the elastic energy. Therefore it is unlikely that an increase in elastic energy is the main cause of the reduced thermal stability. Note that the influence of the substrate has been neglected, as it should not strongly affect the elastic energy. In Fig. 3.9 (b) the total amount of indium per QW is investigated. A better correlation between the amount of indium atoms and the degradation threshold is observed. One deviation from the trend can be seen for the DQW sample with 40% and a QW thickness of 1.5 nm, which degrades much faster than the others. Such a deviation

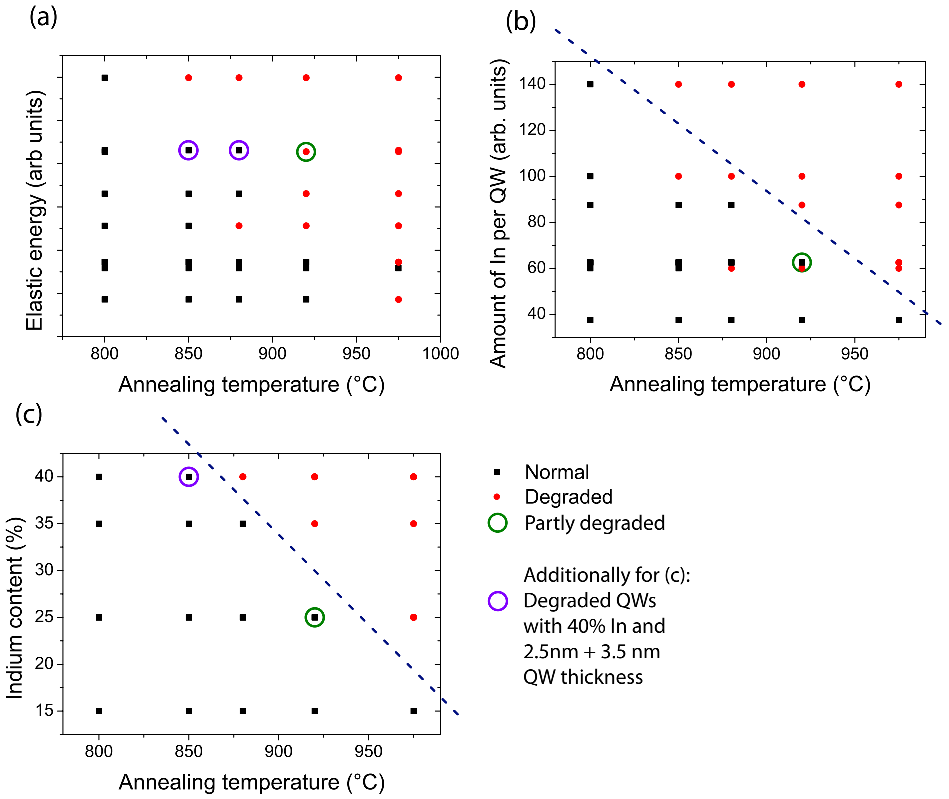

Figure 3.9: Parameters affecting the degradation over the annealing temperature. (a) elastic energy, (b) amount of indium atoms per QW and (c) indium content in a QW. Samples with normal QW emission are in black, degraded samples in red. One sample is partly degraded (25% In, 5 QWs, T_a = 920°C and displayed in green. The degraded samples with 40% In and 2.5 nm and 3.5 nm annealed at 850°C are shown in violet circles for (c) when they overlap with an undegraded sample. Trends are indicated by dotted lines.

could originate from a lower material quality for such high indium content, such formation of misfit dislocations or a inhomogeneous indium distribution, which are also likely to affect the degradation. A similar and even stronger correlation is observed when the indium content dependency is analyzed (Fig. 3.9 (c)). Therefore it can be concluded that lower binding energy due to higher indium content seems to be the main origin of the reduced thermal stability.

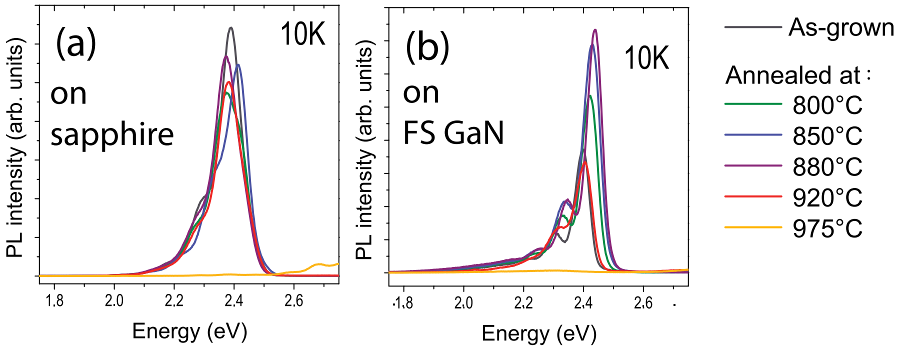

Figure 3.10: PL spectra of the DQW samples with 25% In taken at 10K pumping into the GaN barriers with low excitation power. (a) grown on sapphire and (b) grown on FS GaN.

Effect of the substrate

To probe the role of the substrate, the DQWs with 25% In grown on sapphire (series A) and on FS GaN (series C) are compared. Their 10K PL spectra are displayed in Fig. 3.10. It can be seen that there is a slight improvement in PL intensity for the sample grown on FS GaN (until T_a = 850°C) but not for the one grown sapphire. In addition, it exhibits a reduced PL intensity for T_a = 920°C, which is not the case for the DQW grown on sapphire. This difference could either be due to a faster degradation on FS GaN, or to a different sensitivity to the degradation for the FS GaN sample. The different cap layer thickness could also play a role. These differences will be discussed in detail in part 3.2.4. Focusing on the degradation of the 10K PL emission, no major difference between the samples grown on sapphire and FS GaN has been observed.

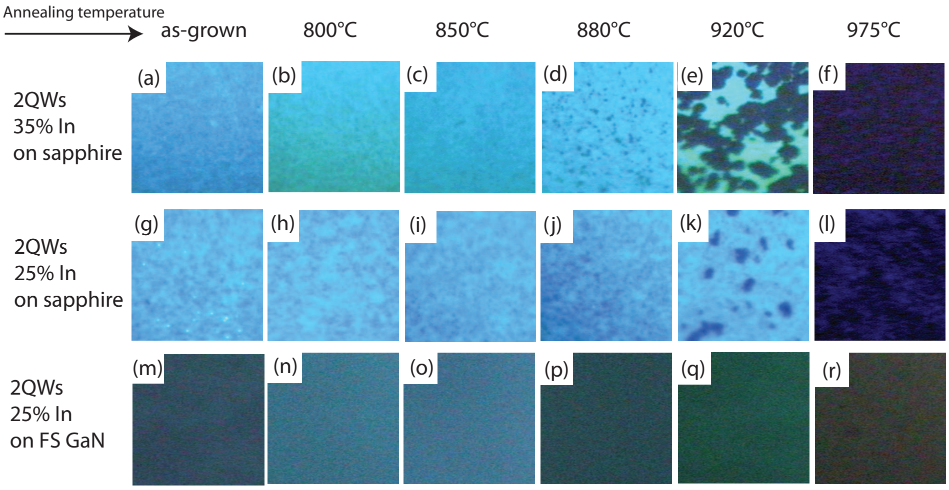

Figure 3.11: 60 x 60 μm^2 RT fluorescence maps of as-grown and annealed InGaN DQWs grown by MOVPE. (a)-(f) show a DQW with 35% In and (g)-(l) a 25% In DQW, both grown on sapphire. (m)-(r) correspond to a DQW with 25% In grown on FS GaN.

3.2.2 Investigation of the degradation

In this part, the focus will be on the sample degradation. First, fluorescence measurements are presented. This measurements are then correlated to PL and micro-PL measurements. Finally, XRD and HR-TEM analysis allow to discuss the origin of the degradation in more detail.

Dark spots

One feature of the degradation of InGaN QWs is the appearance of dark spots in fluorescence maps [146, 147]. These dark spots have been attributed to non-radiative centers created by the diffusion of indium towards dislocations [147] or v-pits [16]. Annealed samples have been investigated by fluorescence measurements at RT. The fluorescence maps of three DQWs are presented in Fig. 3.11 (as-grown and after TA). First, one can see that no dark spots appear in the sample grown on FS-GaN (3rd line). However, its intensity becomes really low for T_a > 920°C. This is in line with the observations from the LT PL data (Fig. 3.7 (b)), where no emission is observed for T_a = 975°C. For the samples grown on sapphire, dark spots appear as early as 880°C for the sample with 35% indium and at 920°C for the one with 25% In. Their size and density increase when increasing T_a. For a better quantification, the samples in Fig. 3.11 (d), (e) and (k) are highlighted by an adjusted color map (Fig. 3.12). It can be clearly seen that the proportion of dark spots increases with higher T_a, or for higher indium content at the same T_a. These results are in good agreement with the observations of Queren *et al.* [146, 147] who used a lower indium content but a higher T_a above 1000°C. Therefore, correlating the dark spots with the change in color and PL emission seems reasonable.

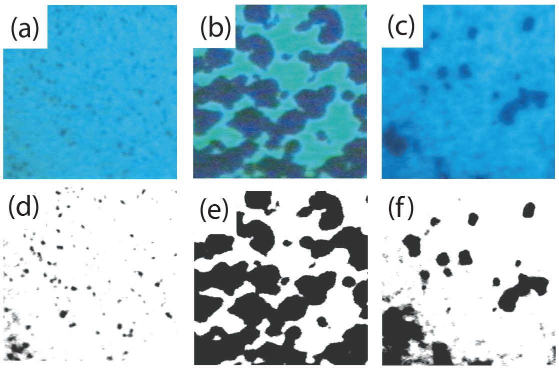

2QWs, 35% In 2QWs, 35% In 2QWs, 25% In
T_a: 880°C T_a: 920°C T_a: 920°C

Figure 3.12: 60 x 60 μm^2 RT Fluorescence maps of InGaN DQWs grown on sapphire by MOVPE. A DQW with 35% In annealed at (a) 880°C and (b) 920°C and a DQW with 25% In annealed at (c) 920°C are displayed. (d)-(f) the colormap has been adjusted to highlight the dark spot area.

Blue luminescence peak in the degraded samples

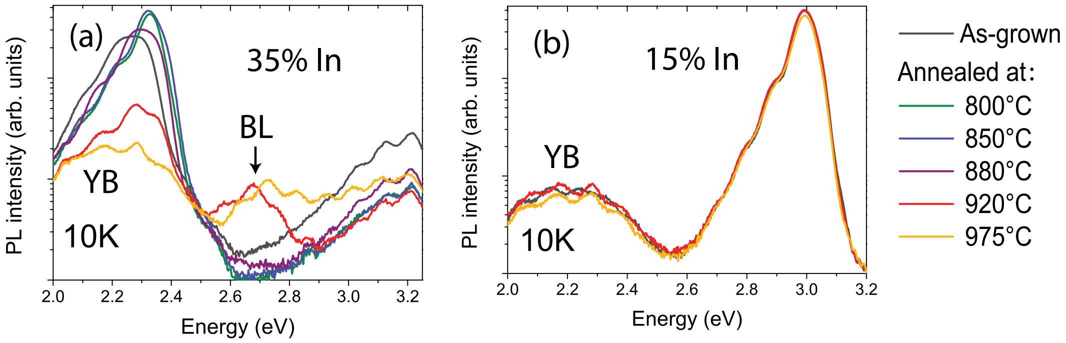

Figure 3.13: 10K PL spectra of samples with (a) 35% In and (b) 15% In for different T_a.

When looking at the PL spectra of the samples with dark spots in more detail, a second peak can be observed at ≈ 2.75 eV, as shown in Fig. 3.13 (a) for the DQW with 35% In. This peak at about 2.75 eV will be referred to as blue luminescence (BL). It is worth noting that its position seems to vary slightly for the different samples: values between 2.85 eV and 2.67 eV were observed. This BL is also present in the completely degraded samples. When the annealing temperature is reduced, this BL peak vanishes and is already no longer present in PL for $T_a \leq 880$°C. When looking at the sample with 15% (Fig. 3.13 (b)), this peak is not observed not even when the sample is annealed at 975°C. Therefore, this peak might be correlated to the degradation of the InGaN QWs. The energy of the transition, above the QW and below the GaN, could make one think about a deep level in the GaN. However, since it only appears in annealed InGaN QWs with a high indium content that are degraded, it should be correlated to the degraded InGaN alloy.

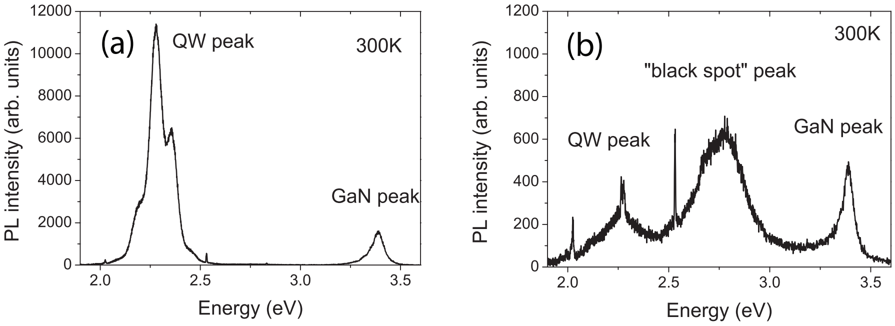

Figure 3.14: Spectra taken with the micro-PL setup for the sample with 35% In annealed at 920°C at RT. (a) a typical spectrum of a non-degraded area is displayed, (b) a typical spectrum taken at a dark spot location. The sharp lines seen around 2 eV and 2.5 eV originate from the Ar-laser.

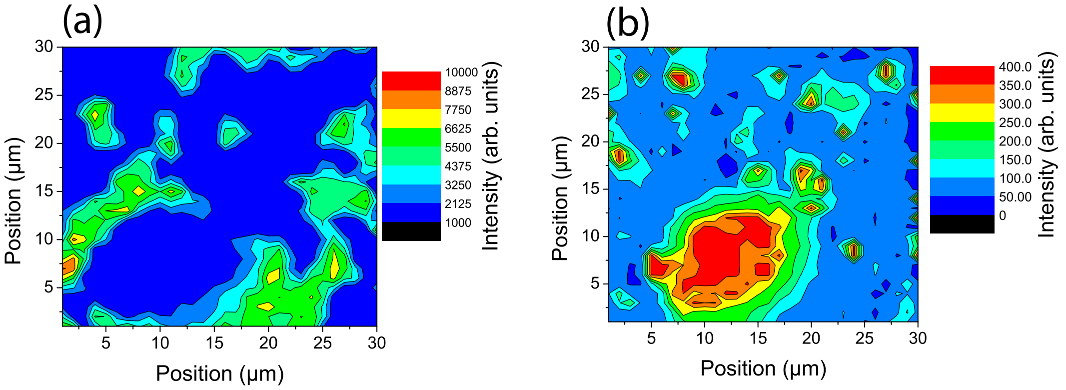

Figure 3.15: 30 x 30 μm^2 micro-PL intensity maps of the sample with 35% In annealed at 920°C at RT. (a) intensity of the QW peak (2.3 eV), (b) intensity of the peak at 2.75 eV.

To analyze this BL in more detail, micro-PL has been performed. In Fig. 3.14 two single spectra are presented for the DQW sample with 35% In annealed at 920°C. In Fig. 3.14 (a), a typical spectrum from a region in between the dark spots is shown. At this position, the sample exhibits a sharp and non degraded QW emission. However, the QW emission is strongly reduced by about two orders of magnitude in the dark spot region (Fig. 3.14 (b)). In addition, the peak at 2.75 eV is observed with a higher intensity than the QW peak itself (at this spot). Therefore, micro-PL allows to differentiate between the areas of normal QW emission and the blue luminescence regions. In Fig. 3.15, 30 x 30 μm^2 micro-PL mappings of this sample with 1 μm steps is presented. It can be seen that the BL at 2.75eV only originates from some regions. It is reasonable to attribute the BL area in to the dark spots observed by fluorescence (Fig. 3.12 (b)). The QW as well as the overall emission from this region is strongly reduced, thus it appears darker compared to the regions around it. However, in this region the 2.75 eV peak is the most intense, which again means the BL is linked to the dark spot area.

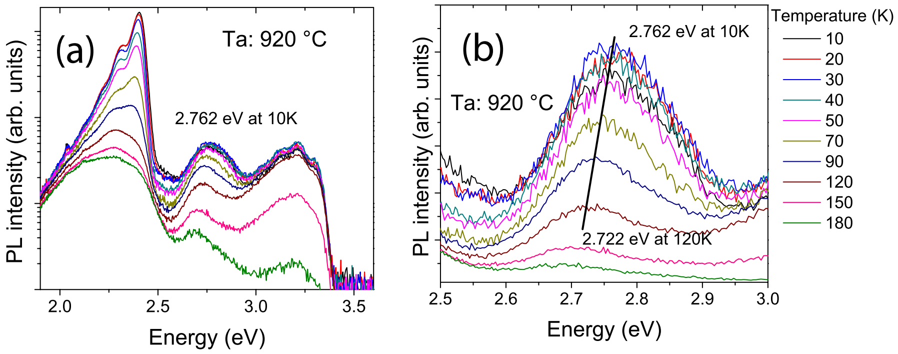

Figure 3.16: PL spectra taken at low excitation power pumping into the GaN. (a) The PL spectra of the DQW sample with 25% grown on FS annealed at 920°C are displayed for different temperatures. In (b) the BL peak is highlighted.

3.2.3 Origin of the blue luminescence

The BL peak is also observed for samples grown on FS GaN, as shown in Fig. 3.16 for a DQW sample with 25% In annealed at 920°C. The BL is highlighted in Fig. 3.16 (b). It can be seen that it exhibits a redshift with increasing temperature. The shift of the peak position of the QW and the BL are displayed in Fig. 3.17 (a). The BL shifts a bit slower than the QW. In Fig. 3.17 (b), the normalized integrated PL intensity of both peaks is shown as a function of the temperature. The QW peak quenches faster with the temperature. Fitting the curves with two exponentials allows extraction of an activation energy (E_a) of 16 meV and 59 meV for the QW peak and 25 meV and 179 meV for the BL peak. When looking at the excitation power dependence of the BL (Fig. 3.18) at a dark spot position (using micro-PL), no shift in the peak position is observed. This could indicate a deep level being involved. It could thus be likely that the BL is related to a localized defect that appears after annealing in certain areas (dark spots). The dark spots have been tentatively attributed to indium diffusion towards dislocations [16]. However, the 2.75 eV peak is also observed on samples grown on FS GaN, where the dislocation density is much lower. In addition, it is worth mentioning that the dark spot density on the samples grown on sapphire is far below the dislocation density. Therefore, it can be assumed that dislocations are not the main origin of the dark spots.

To gain further insight on the possible origin of the BL peak, HR-TEM was performed on the 35% In DQW sample annealed at 920°C. The as-grown reference and the annealed sample are displayed in Fig. 3.19. White and dark spots are observed for the annealed (and degraded) samples; white spots have been attributed to metallic indium clusters (by EELS) and dark areas to voids. Similar observations have also been reported by other groups for InGaN QWs [148, 149, 150]. The appearance of metallic indium clusters is not unexpected. The bond between indium and nitrogen is weaker that the one between gallium and nitrogen [151], and should thus break more easily, allowing the formation of metallic indium clusters.

If indium clusters form, a strong structural degradation should be observable by XRD. In Fig. 3.20, an omega-2theta XRD scan of the DQW samples with 35% In grown on sapphire is shown

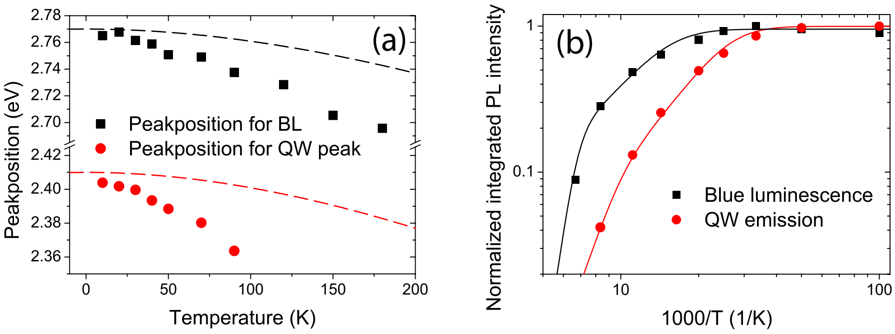

Figure 3.17: Sample with 25% In grown on FS GaN. (a) peak position *vs* temperature and (b) integrated PL intensity *vs* temperature. Varshni plots and arrhenius fits are indicated by dotted and full lines, respectively.

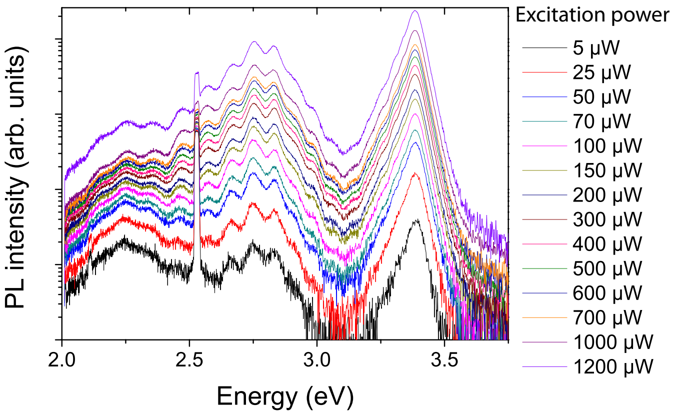

Figure 3.18: PL spectra of the 35% In DQW sample taken at different excitation powers with a spotsize of about 1 μm^2, which leads to excitation power densities from 200 W/cm^2 to 48 kW/cm^2 (when the transmission of the microscope objective is taken into account). Note that the 2.5 eV emission comes from scattered laserlight from the cw Ar laser used to pump into the GaN.

for the as-grown reference and annealed samples. It seems that the TA has already some effect at 800°C. The shift of the SL0 peak, highlighted by the dotted line, indicates a reduction in the average In content, which is likely due to out-of-plane diffusion. In addition, the shift of the superlattice peaks indicates a loss of interfaces. Note that the XRD is not sensitive to local variations in the indium content. However, the loss of interface indicated by the XRD measurement is in good agreement with the results from HR-TEM.

The possible origin of the BL needs to be discussed in more detail. BL in the 2.75 eV energy range is observed in undoped GaN, as well as in Mg- (and Zn-) doped GaN [144]. Note that a similar peak, at 2.65 eV, was also reported for InGaN QWs annealed for over 8h at 950°C [152], together with the appearance of In-rich clusters. In a follow up study, this peak was tentatively attributed to gallium vacancies [148], but emission in this energy range is commonly attributed to other defects [144]. In the following, the likelihood of the different potential origins will be

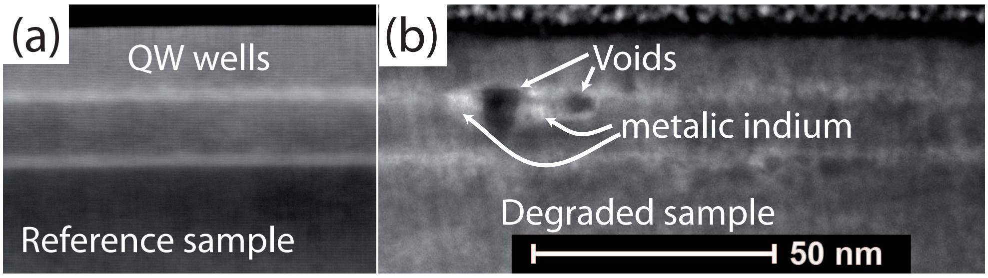

Figure 3.19: HR-TEM image of the 35% In DQW sample (a) as-grown and (b) annealed at 920°C. The white spots corresponds to metalic indium clusters (by EELS), while the dark areas have been tentatively attributed to voids. The data is by courtesy of Francesco Ivaldi and Dr. Slavomir Kret (IFPAN, Poland).

discussed:

(a) Impurities, such as Zn, which could cause BL are unlikely, due to the fact that the peak is visible in completely degraded InGaN QW samples grown by two different MOVPE reactors as well as by the MBE reactor (not shown here). In addition, the BL is not observed in as-grown samples.

(b) Plasmonic effects could potentially be involved, as metallic indium clusters are observed by HR-TEM. Some plasmonic effects have been reported e.g. for In clusters in InN [153]. However, after a small calculation, the clustersize observed by HR-TEM is nearly an order of magnitude smaller than what would be needed for an emission at 2.75 eV. In addition, metal nanoparticle size fluctuations should lead to variations in the peak position. However, only broad peaks without strong variations in peak position have been observed using micro-PL. Thus plasmonic effects of the nanoparticles are not likely to be responsible for the BL at 2.75 eV. However, the metallic In clusters could be indirectly responsible: their formation goes hand in hand with the breaking of the In-N bond. In the degraded areas, there should be Ga with dangling bonds (nitrogen vacancies, V_N), as well as additional nitrogen (nitrogen interstitials). But interstitials are supposed to be very mobile already in a temperature range of about 200°C [154], and can thus be expected to have already diffused out during the TA step. Three other effects could however occur:

(c) Oxygen is a common impurity and could diffuse to Ga dangling bonds created during TA. On a nitrogen position, it is a shallow donor [155] with a low formation energy [156]. Oxygen was proposed to be responsible for BL observed in etched GaN [144, 157]) and could thus potentially cause BL in the degraded InGaN region.

(d) Gallium vacancies (V_{Ga}) were proposed before to be at the origin of the BL in degraded InGaN QWs. V_{Ga} are supposed to have a transition in the right energy range (at 0.64 eV above the valence band)[144]. It should be mentioned that the BL peak observed for degraded InGaN

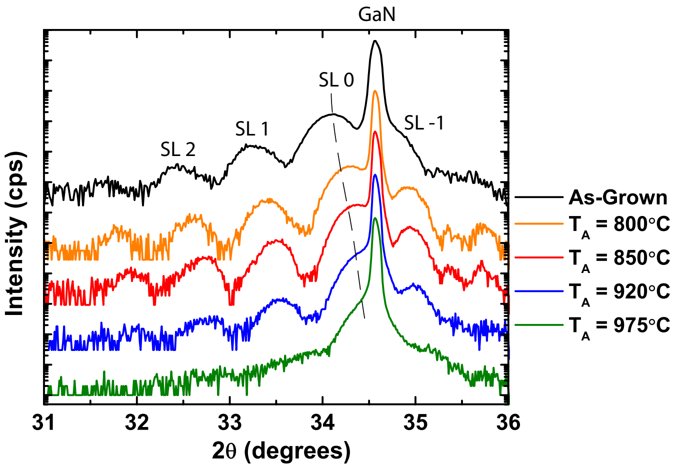

Figure 3.20: XRD curve of the DQW sample with 35% In (from series A) for as-grown and annealed. The superlattice peaks are indicated, and a guide to the eye (dotted line) shows the evolution of the SL0 peak.

samples [152] could be suppressed when the TA is performed under nitrogen and gallium overpressure [148] and that the BL is normally not linked to V_{Ga} [144]. Another option is more likely:

(e) V_N should appear around the metallic In clusters. They are supposed to be deep donors with an energy level at around 0.59 eV above the valence band maximum [154]. The observed BL peak is around 0.6 eV below the GaN emission, and could thus correspond to a transition involving V_N. Consequently, nitrogen vacancies are good candidates to explain the BL peak. In fact, similar BL has been observed for Mg-doped GaN, and attributed to V_N related transitions [144, 158]. More information about BL from Mg-doped GaN can be found in the review from Reshchikov and Morkoc [144]. Note that the formation energy of V_N is strongly reduced in Mg-doped GaN, making them common defects there. This is different to the degraded InGaN QWs, where V_N would be mainly created post-growth during the formation of the indium metal clusters; nevertheless, BL could originate from V_N in both cases.

To summarize, BL at 2.75 eV is observed for the degraded samples. This peak is linked to the degraded areas observed by micro-PL. HR-TEM indicates the appearance of metallic In clusters in those samples. There is probably an intermediate state where the interfaces start to disappear and In-rich clusters form, as indicated by XRD. The peak at 2.75 eV could originate from the breaking of the In-N bond leading to the formation of nitrogen vacancies, gallium vacancies, or possibly gallium oxide. While all three have been attributed to BL, a transition involving nitrogen vacancies seems to be the most likely explanation for the peak at 2.75 eV.

3.2.4 Improvement in QW luminescence of indium-rich InGaN QWs by thermal annealing

Annealing is used in many semiconductor systems to improve the material quality. While the thermal instability of In-rich InGaN alloys might be detrimental for InGaN-based devices, there is a window where thermal treatment can have a beneficial effect.

In an earlier study, Chuo *et al.* annealed InGaN QWs grown by MOVPE at 750 °C with a nominal thickness of 40 Å and a nominal indium content above 40% [159]: the authors observed an homogenization of the QW upon annealing at 900°C for 10 minutes under N_2 atmosphere. Their QWs turned from islanded to a more homogeneous layer. In addition, this homogenization was accompanied by an increase in the integrated PL intensity at 25K, a reduction in FWHM and a blueshift of the emission peak. In a follow-up study, they showed that this improvement was enhanced with increased annealing duration [160]. It is worth to mention that the cap on top of their active region was only 40 nm thick. Consequently, overgrowth did not impose a strong thermal budget on the underlaying QW region. A similar improvement was observed by Wang *et al.* [161] for InGaN QDs grown by MOVPE: when annealed at 775°C for 20 min in N_2 atmosphere, an improvement in EL as well as a blueshift were observed. At high T_a, in their case 830°C, the EL intensity decreases again and the FWHM reduces. This was attributed to a shrinking of the QD size and an eventual mergence into the wetting later. Therefore, thermal annealing seems to lead a homogenization of the indium content, which could be beneficial for QWs. Apart from possible indium homogenization, TA could also be beneficial for a defect curing process (discussed in more detail in part 3.5).

Beneficial effects of thermal annealing on indium-rich QWs grown by MOVPE

In Fig. 3.21, the spectra of the DQW sample with 35% In grown on sapphire are displayed at different temperatures. In Fig. 3.21 (d), the integrated PL intensity has been calculated and normalized to the as-grown intensity (at 10K and 70K). It can be observed that before the sample gets degraded ($800°C \le T_a < 920°C$), the intensity at 10K is nearly constant. However, the PL emission at 70K is increasing for annealed samples until $T_a = 880°C$. In particular, the intensity is the most intense for the sample annealed at 850°C). This can be explained keeping in mind the common assumption that the LT PL should not be sensitive to non-radiative defects. Hence, non-radiative defect curing by TA should not be observed at 10K. On the other hand, when the temperature is increased, the PL becomes more sensitive to non-radiative channels, and any improvement in the material quality will then affect the PL intensity. The behavior of the sample annealed at 920°C highlights another interesting point. At 10K, the emission of that sample is very low (Fig. 3.21 (a)), in good agreement to the dark spots observed by fluorescence (see Fig. 3.12 (b)), which indicates that only a minor part of the initial QW area is emitting. However, at 150K, the sample becomes more intense than the as-grown one (Fig. 3.21 (d)), whose QW emission has vanished into the yellow band. Since in this temperature range the non-radiative channels dominate, this increase in intensity is attributed to an improvement

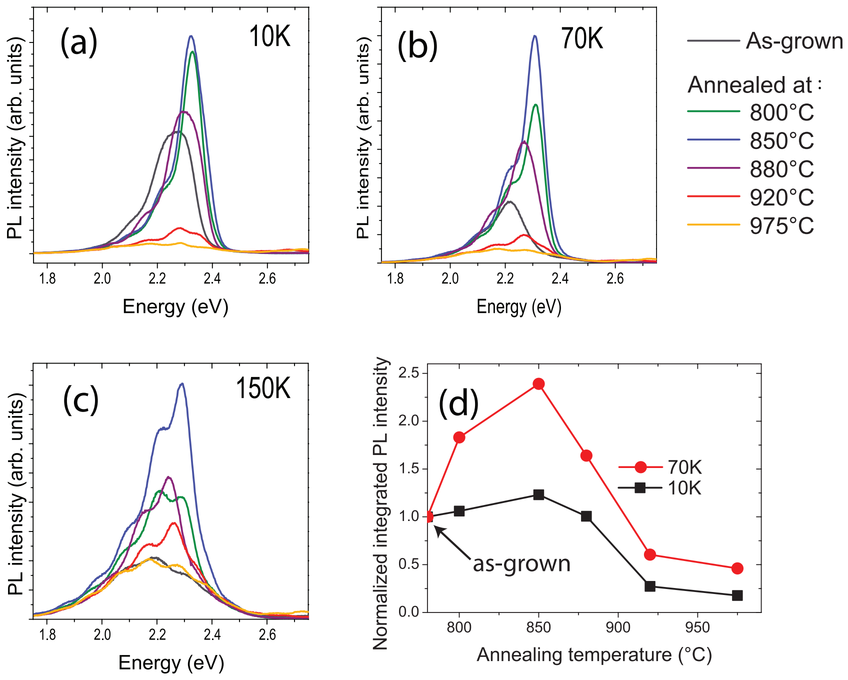

Figure 3.21: PL spectra of the DQW with 35% In as-grown and annealed taken at different temperatures. The spectra are shown at (a) 10K, (b) 70K and (c) 150K. (d) normalized integrated PL intensities of the annealed samples for 10K and 70K. Note that the intensities were normalized to the as-grown intensity.

of the material quality in the remaining QW area. Therefore, it can be concluded that two competing mechanisms govern the behavior of the QW during TA. At a low T_a, the material quality is improved, while at a higher T_a, the QW starts to degrade with the appearence of dark spots, indicating a loss of QW area. Thus there is an optimum T_a where the PL emission from the QWs is maximized. Investigating the sample with 25% In grown on sapphire that degrades at a higher T_a allows one to further extend the temperature range. In particular in Fig. 3.22 it can be seen that the as-grown QW emits up to room temperature. The sample annealed at 975°C is degraded and only exhibits a very feint QW emission. It will not be treated in the following discussion.

At 10K, all samples emit within the same order of magnitude. In Fig. 3.23, the integrated luminescence intensity of the annealed samples is plotted for several measurement temperatures. In each case, the values are normalized to those of the as-grown sample at the same temperature. One can see that the PL signal of the annealed samples is more intense when increasing the PL temperature. For a given PL temperature, the maximum of intensity occurs for a certain T_a. In particular, below 150K, the most intense sample is the one annealed at 880°C. On the other hand, above 150K, it is the one annealed at 850°C. To understand the change in the annealing temperature for which the maximum PL intensity is reached, the interaction of the carriers with the dark spots has to be taken into account. While excitons are localized at low temperatures, they become mobile as the temperature increases. With a

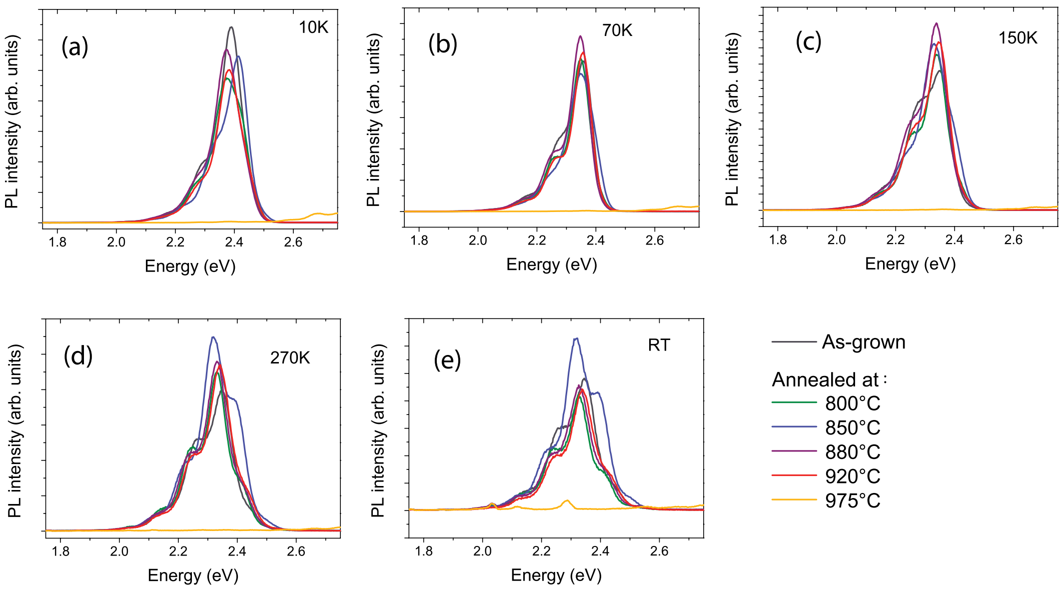

Figure 3.22: PL spectra of the DQW with 25% In as-grown and annealed taken at different temperatures. The spectra are shown at (a) 10K, (b) 70K, (c) 150K,(d) 270K and (e) RT.

larger diffusion length, the probability to encounter non-radiative recombination centers that are located at a dark spot is increased. The change in the optimum T$_a$ is therefore tentatively attributed to a balance between the increase of the material quality and the enlargement of the dark spot areas with the temperature. Another interesting fact is deduced when comparing the maximum improvement for different indium contents. As seen in Fig. 3.23, the intensity of the sample with 25% In annealed at 850°C increases by a factor of 1.15 at 150K, while for the sample with 35% In annealed at the same T$_a$ (see Fig. 3.21), the increase in intensity reaches a factor of 2.3 at 70K. For the sample with 15% In, no significant improvement in PL intensity was observed for the investigated range of T$_a$. Therefore, it seems that the magnitude of improvement not only depends on T$_a$, but also on the indium content. This might be due to the lower growth temperatures needed for the higher In content, which can increase the point defect density. This will be discussed in more detail later on.

To summarize, an increase in PL intensity can be observed upon thermal annealing of In-rich InGaN QWs. However, at high annealing temperatures, the degradation dominates. An optimum T$_a$ exists where the strongest PL emission can be achieved, which depends on the indium content: the higher the indium content, the higher the improvement and the lower the optimum T$_a$.

Effect of TA on the linewidth and peak position

Apart from affecting the PL intensity, the TA can also affect the PL linewidth: looking at the sample with 35% In (Fig. 3.21) the PL linewidth is reduced upon annealing at 800°C, which can

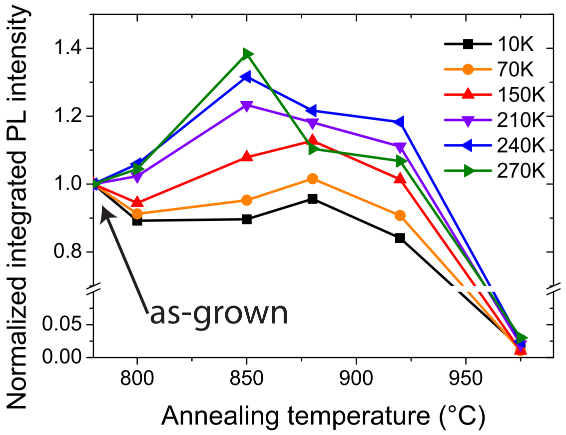

Figure 3.23: The improvement in integrated PL intensity of the QW peak of the annealed as compared to the as-grown sample over T$_a$ for the DQW with 25% In grown on sapphire for different temperatures.

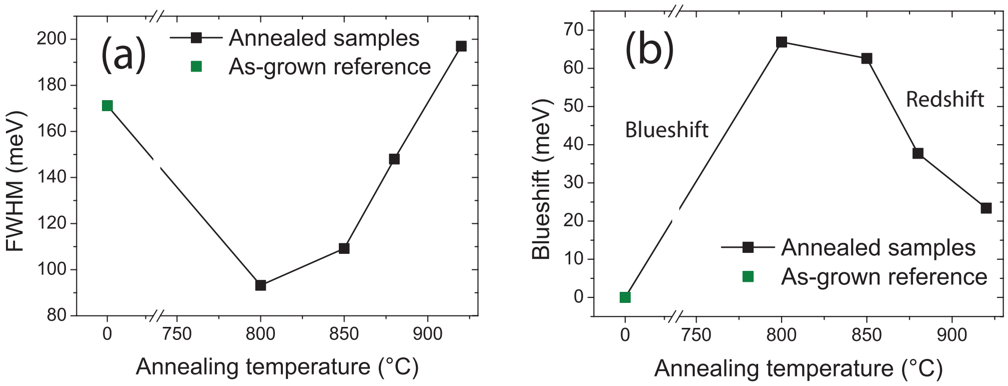

Figure 3.24: PL data of the QW with 35% In as-grown and annealed is displayed. In (a) the linewidth of the QWs at 10K is shown. In (b) the blueshift of the PL peak at 10K is displayed.

be already observed at 10K (Fig. 3.24 (a)). This could originate from a homogenization of tiny indium-rich clusters in the QW, similar to what was observed for InGaN QDs [161]. However, when T$_a$ increases above 800°C, the linewidth broadens, probably due to a degradation of interfaces leading to variation in the QW thickness, in agreement with the XRD analysis (Fig. 3.20). In addition, a blueshift is observed upon annealing at T$_a$ =800°C (Fig. 3.24 (b)), which is in agreement with the homogenization of tiny indium-rich clusters. The redshift that occurs for T$_a$ ≥850°C can be explained by the beginning of indium clustering, as it is accompanied by an increase in linewidth.

Effect of the substrate

QWs grown on FS GaN also exhibit the same improvement, but it is more difficult to assess.

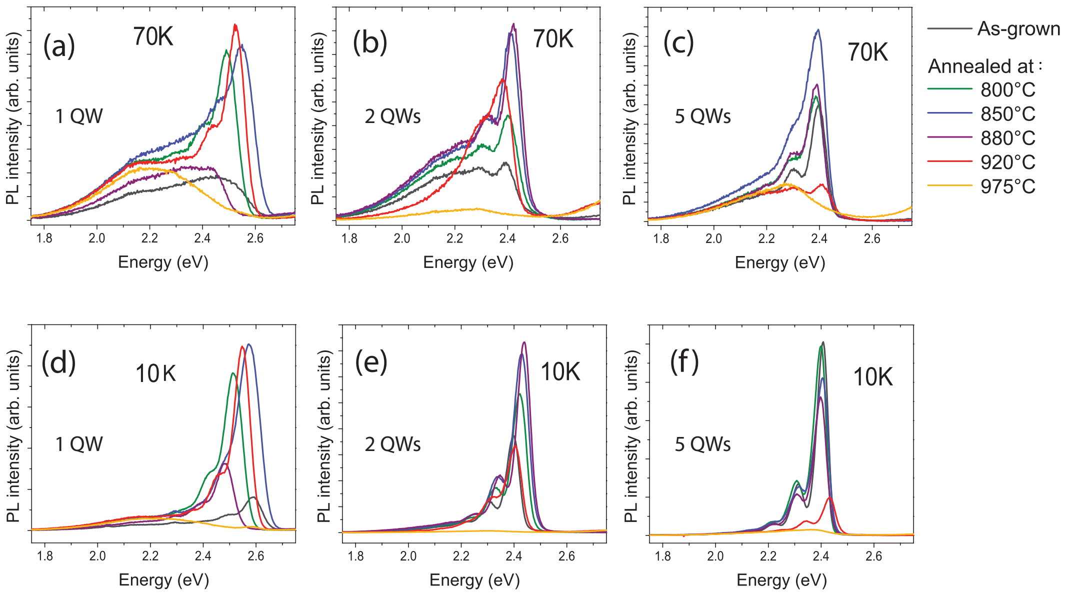

Figure 3.25: PL spectra of the DQWs with 25% In grown on FS-GaN as-grown and annealed. The spectra are shown for 1 QW, 2 QWs and 5 QWs in (a)-(c) at 70K and (d)-(f) at 10K respectively as comparison.

Using low excitation power, the PL emission of indium-rich InGaN QWs grown on FS GaN quenches quickly with rising temperatures and vanishes into the yellow band. At intermediate temperatures however, e.g. at 70K, the PL intensity is increased for some T_a. In Fig. 3.25 the 10K and 70K spectra of the InGaN QWs grown on FS GaN (series C) are displayed. Note that one SQW sample seems to have a different emission energy, which could be due to wafer inhomogeneity. The PL intensity of the samples annealed below the degradation threshold (defined by the loss of the QW emission at 10K) is increased with respect to their as-grown reference samples at 70K. In addition, the optimum T_a at 70K shifts from 880°C for 2 QWs to 850°C for 5 QWs, as expected from the thermal stability study presented earlier. Thus, they follow the trend of the samples grown on sapphire.

However, the increase in PL intensity after annealing with respect to the as-grown intensity is much more pronounced for the SQW and DQW sample than for the MQW one. This is explained in the following.

Self-annealing during MQW growth

Series C also allows to investigate the role of self-annealing that takes place during MQW growth. During the growth of the upper QWs, the first QW is kept at the growth temperature and thus the thermal budget induced on the first QW increases with the number of subsequent QWs. The 10K PL emission of the as-grown references of series C and the samples annealed at 850°C are shown in Fig. 3.26. As already mentioned, the SQW sample exhibits a slightly

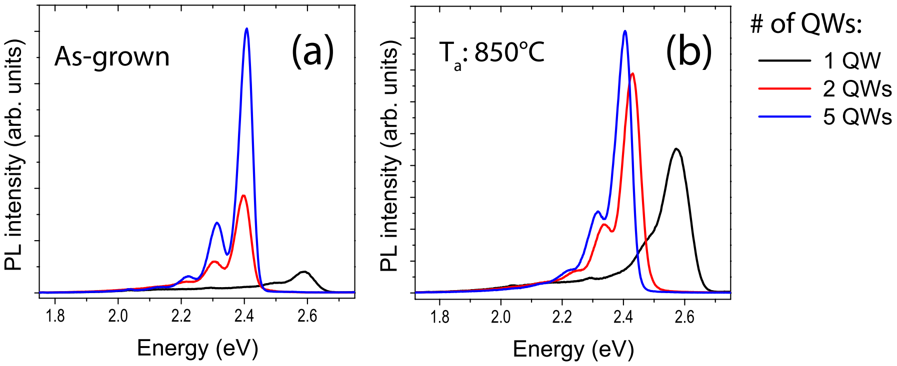

Figure 3.26: PL spectra of the QWs grown on FS-GaN at 10K. (a) As-grown and (b) annealed at 850°C.

lower In content, which could originate from a delayed In incorporation or slight variations in T_{gr}. However, a clear intensity difference between the as-grown samples with one, two and five QWs is observed. This intensity difference is likely to originate from thermal annealing of the lower QWs during growth of the upper ones. After annealing, the difference in intensity between 5, 2 and 1 QWs is decreased, meaning that the sample with 5 QWs has improved less than the two other ones. If it would be due to the number of QWs, the intensity ratio should be independent of T_a. If the thermal budget induced during growth improves the material quality, the MQW stack could be considered as already annealed and should thus display a smaller improvement than the SQW or DQW upon an additional TA. Indeed, the PL intensities of the three samples are much closer after the TA. Therefore, it can be assumed that a part of the different efficiency between SQWs and MQWs comes from a self-annealing of the QWs during the growth of the MQW stack.

Localization

It is interesting to note that the improvement of the QW quality with TA is already observed at 10K for the samples grown on FS GaN. This could mean that the assumption of a 100% radiative emission at 10K is probably not correct even for low dislocation densities. Instead, the shallow localization in the FS GaN samples could make them more sensitivity to non-radiative channels. This could explain the difference in PL intensity at 10K for the DQWs grown on sapphire and FS GaN when annealed at 850°C (see Fig. 3.10). As mentioned before, the samples grown on FS GaN exhibit a lower PL linewidth than the samples grown on sapphire. For comparable samples, the PL linewidth of a DQW with about 25% In grown on FS GaN is about 51 meV, while the one for sapphire is about 88 meV at 10K. This reduced linewidth for QWs grown on FS GaN is explained by a more inhomogeneous indium distribution than in the InGaN QW grown on sapphire. As indicated by Fig. 3.27, the redshift with temperature of the sample on FS GaN seems to be very small compared to the one on sapphire. The latter exhibits a strong S-shaped behavior which is commonly observed for such QWs. This supports a better

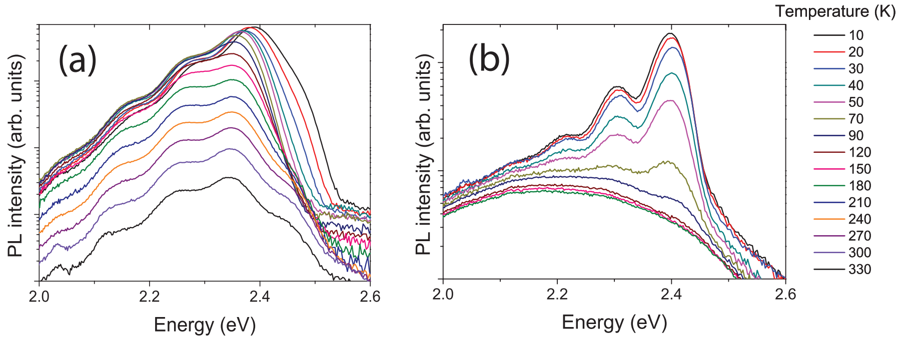

Figure 3.27: PL spectra at different temperature of the as-grown DQWs with 25% In grown on (a) sapphire and (b) FS-GaN. Note that low excitation power was used to pump into the GaN. While the range from 10K to 330K is presented for (a), in (b) the temperatures above 180K are not shown.

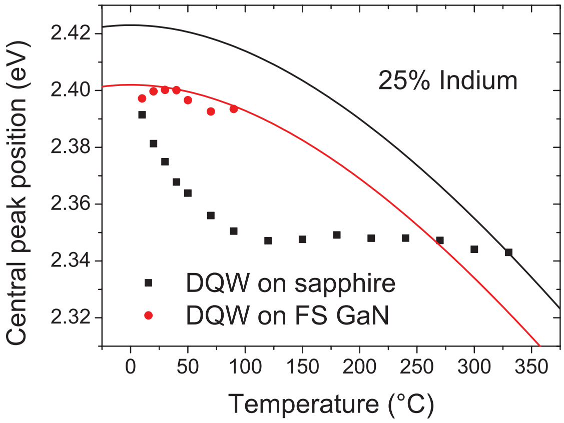

Figure 3.28: Central QW peak position over temperature for the DQWs with 25% In grown on FS-GaN and sapphire. To compare, the varshni-fits are indicated by lines. Note that the peak position is only displayed until it is distinguishable from the yellow band.

alloy homogeneity for samples on FS GaN.

3.2.5 Summary and outlook for applications

Thermal stability is one of the main remaining issues for high indium content QWs grown by MOVPE. This issue is linked to the defect density and homogeneity of the layer. As shown in part 3.2.1, the degradation takes place for both samples grown on sapphire and on FS GaN, indicating that while dislocations might enhance the degradation, they are not necessary. The degradation is indium content related, and increases with rising QW thickness or the number of QWs. It seems to depend mainly on the indium content and amount of In atoms available, while a difference in elastic energy seems to have only a minor effect. However, the material quality seems to play a role as well.

For low indium content QWs, no degradation was observed for the thermal budgets studied here. On the other hand, for a high indium content, a nearly complete degradation could be observed not only by a loss of PL emission, but also by a visual change in the color of a sample. This change probably originates from the appearance of dark spots that are visible by fluorescence and resolved by micro-PL measurements. At the dark spots, a secondary emission peak is measured in micro-PL at 2.75 eV. This peak is also visible in the degraded and partly degraded samples at lower PL temperatures. However, this peak is not observed for non-degraded samples, even when annealed at the same temperatures. A similar peak has been observed in the literature for degraded InGaN [148]. The peak position remains with varying excitation power, and HR-TEM investigations show the appearance of metallic indium clusters and voids in the QW layers. It is thus likely that the peak is related to V_N transitions, created by the formation of the metallic indium clusters.

At the same time, at moderate T_a, an improvement of the luminescence properties takes place. This improvement is only minor, apart from the sample with 35% indium. The TA can reduce the linewidth, but also increases the PL intensity when non-radiative recombinations play a role. Such an annealing already takes partly place when growing a MQW structure, where the upper QWs can introduce a beneficial thermal budget on the lower ones; the same should hold true for the growth of a *p*-type layer (unless its thermal budget degrades the QWs).

There are possibilities that should reduce the sensitivity of the InGaN QWs to the thermal budget up to a certain degree, such as playing with the barrier material (AlGaN barriers seem to reduce the indium diffusion [146]), varying the growth conditions (e.g. T_{gr} of the QWs could affect this) and reducing the defect density. Within some limits, optimized growth conditions and design of the device can thus enable to fabricate indium-rich devices despite the issue of thermal degradation. Such approaches are used for commercial devices [147]. However, these options seem only valid for a not too high indium content. For higher indium content, there is no other option than reducing the temperature of the top layer, which requires a good *p*-type layer grown at much lower temperature than commonly used. However, as the growth window to grow a good *p*-type layer by MOVPE is more limited than for MBE, MOVPE might not be the optimum growth technique for very high indium content based devices.

To briefly summarize, the following points should be taken into account for designing indium-rich InGaN based devices:
(i) High indium content QWs may degrade before it can be resolved by fluorescence measurements.
(ii) To avoid the degradation of DQWs with 25% indium, the T_{gr} of the *p*-type / cladding layer should not exceed 850°C. Low temperature *p*-type is thus essential for indium-rich QWs. For an even higher indium content, a lower T_{gr} of the *p*-type layer should be necessary.
(iii) Thinner QWs are more stable than thicker ones, but since the number of QWs has also a detrimental effect, a balance needs to be found to have a good active medium.
(iv) After growing the QW active region, especially with a single QW, a short TA step before the low temperature *p*-type growth may increase the efficiency. Note that the TA step should be performed prior to the *p*-type layer to avoid any potential Mg migration into the active region.

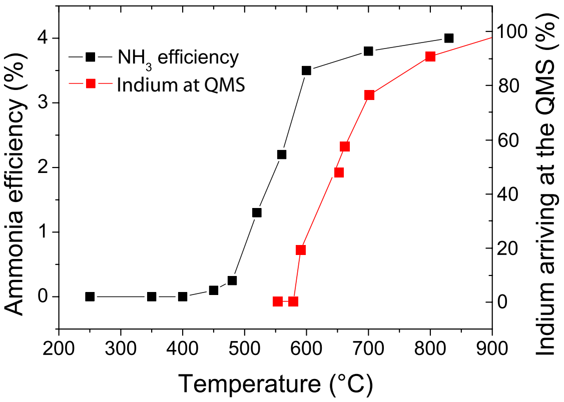

Figure 3.29: The ammonia efficiency (taken from Mesrine *et al.* [167]) and the indium desorption measured by QMS are displayed over the temperature.

3.3 High indium content InGaN QWs grown by NH$_3$-MBE

Even though most commercial nitride-based optoelectronic devices are grown by MOVPE, MBE can be an alternative solution for low temperature growth. Indeed, the MOVPE growth window for the best *p*-type material is at a temperature range (900°C - 1000°C) that can already degrade underlaying In-rich InGaN QWs. NH$_3$-MBE allows to fabricate high quality *p*-type GaN at much lower temperatures, e.g. at 740°C [62]. This temperature is low enough to minimize the thermal budget which leads to the degradation of In-rich InGaN layers. More information about *p*-type GaN by NH$_3$-MBE can be found in the articles by Dussaigne *et al.* [62] or Hurni *et al.* [63]. However, at this low T_{gr} the material quality is lower, especially of the active region. As a general feature, the material quality drops when T_{gr} is reduced [162].

In this part, issues of indium-rich InGaN alloys grown by NH$_3$-MBE will be treated. First, the indium desorption and NH$_3$-efficiency are discussed, and growth conditions to achieve In-rich InGaN alloys presented. Finally, the effect of thermal annealing on MBE grown QWs is investigated.

3.3.1 Indium desorption and NH$_3$ efficiency

To avoid indium desorption, InN and thus high indium content InGaN layers need to be grown at temperatures near or below 550°C [163, 164, 165, 166]. To investigate the indium desorption from the growing surface, a QMS recorded the amount of In reflected back from the surface during InN growth. Fig. 3.29 displays the percentage of indium desorbed as a function of the substrate temperature. For a temperature below 550°C, the In QMS signal is in the background level. However for substrate temperature over 550°C, the In signal increases strongly and starts to saturate around 800°C. At this temperature, no growth occurs any more as all metallic species are re-evaporated. This defines the upper limit of ammonia-MBE growth window for InN. In addition, the ammonia efficiency is plotted on the same graph (the data is taken from Mesrine *et al.* [167]). Here, a lower limit of the growth temperature range can be defined, below

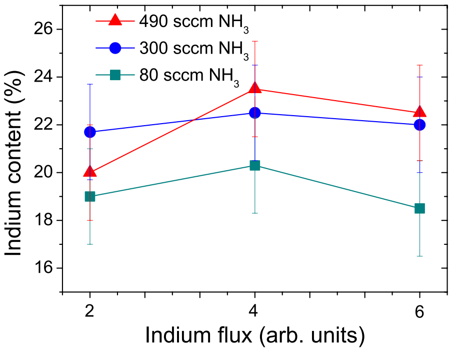

Figure 3.30: Indium content over indium flux for three different NH_3 fluxes, for a fixed Ga flux. The indium content is calculated from simulations using PL measurements under flat-band conditions. The error bar corresponds to the sensitivity of the focus of the microscope objective.

which active nitrogen is no longer available. In the presence of In and Ga, active nitrogen (N^*) will preferentially react with Ga when growing InGaN [168], meaning that the amount of active nitrogen available for indium, N^*_{In}, can be written as:

$$N^*_{In} = N^* - N^*_{Ga}, \tag{3.1}$$

with N^*_{Ga} the amount of active nitrogen available for Ga atoms per unit of time. Subsequently, only the remaining N^* can be used to form InN. Thus, the amount of N^* per unit of time limits the maximum indium content which can be incorporated, for a fixed Ga flux. In principle, supplying additional NH_3 while keeping the Ga and In fluxes constant should provide more N^* available for In and hence increase the indium incorporation. However, blocking site effects must be considered. Also, a higher NH_3 flux will increase the pressure in the growth chamber, and eventually screen the incoming metal flux [104] and consequently reduce V_{gr}.

In order to clarify these issues, a series of SQWs were grown, varying both the In and the ammonia fluxes. 2.5 nm-thick InGaN SQWs were grown with a fixed Ga flux corresponding to a V_{gr} of around 10 nm/h at a T_{gr} of 550°C. At this temperature, the indium desorption is low. Note that the V_{gr} was chosen based on the prior investigation of Dr. Amelie Dussaigne in our group. The indium content in the QWs was extracted from RT PL measurements under flat band conditions, *i.e.* with a very high excitation power, by calculation the peak energy position using the QW thickness (Fig. 3.30). The indium content remains nearly unchanged for all indium fluxes used in this study. A slight increase in the indium content is observed when the NH_3 flux is changed from 80 sccm to 490 sccm.

Under the range of growth conditions used, larger indium fluxes do not lead to an increase in the wavelength, *i.e.* indium content. At these temperatures the indium re-evaporation is low, thus it can be concluded that the growth is nitrogen limited. However, as more NH_3 does not lead to a higher indium incorporation, the dissociation of NH_3 might be limited per unit of time. As already mentioned, this could originate from a site-blocking effect, limiting

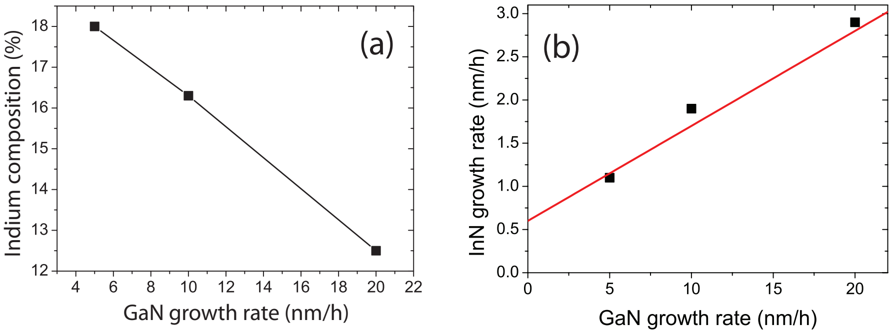

Figure 3.31: (a) The change in indium concentration *vs.* GaN growth rate is displayed, at constant In and NH_3 flux. (b) InN growth rate *vs.* GaN growth rate. A fit is shown by a red line. The NH_3 flux is 300 sccm and an In flux corresponding to the middle range of Fig. 3.30 were chosen.

the NH_3 dissociation at a temperature dependent rate. Another possibility would be indium screening at the growth front. The role of desorption is studied in more detail. To investigate this, three samples have been grown varying the Ga flux, but keeping the QW thickness as well as the In and NH_3 fluxes constant. The indium content is deduced from the QW PL energy and plotted in Fig. 3.31 (a). It can be seen that the indium content changes only slowly. The InN incorporation rate can be calculated from the indium content and the GaN growth rate:

$$x_{In} = \frac{V_{InN}}{V_{InN} + V_{GaN}}, \tag{3.2}$$

with x_{In} the indium content, and V_{InN} and V_{GaN} the incorporation and growth rates of InN and GaN, respectively. Thus V_{InN} is given by:

$$V_{InN} = \frac{x_{In} \cdot V_{GaN}}{1 - x_{In}}. \tag{3.3}$$

Plotting V_{InN} as a function of V_{GaN} (Fig. 3.31 (b)) shows that higher InN incorporation rate is obtained for higher GaN growth rate. Faster GaN growth rate reduces InN desorption, thus enabling higher In incorporation. However, the In content will still be limited by the amount of available N^*. One can remark that the extrapolation for V_{GaN}=0 leads to a very low V_{InN}. This indicates that InN cannot be grown for such growth conditions, as indeed observed.

As a conclusion of this study, the amount of N^* that NH_3 can provide at a given V_{gr} and T_{gr} seems to be limited. It appears to be difficult to achieve highly efficient high indium content InGaN alloys by NH_3-MBE, especially due to a significant desorption.

3.3.2 Circumventing the NH_3 limitation: NH_3 and N-plasma

One of the particularities of the Riber compact 21 NH_3-MBE reactor present in the LASPE is the presence of two nitrogen sources, a NH_3 source and a plasma-source. Here, it will be

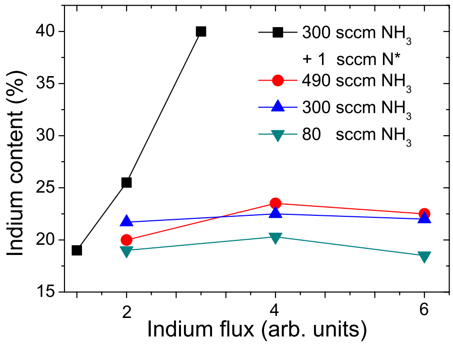

Figure 3.32: Indium content over indium flux for three different NH_3 fluxes and for one with additional N* (for a fixed Ga flux) obtained from simulations using PL data. The PL measurements were performed under flat-band conditions.

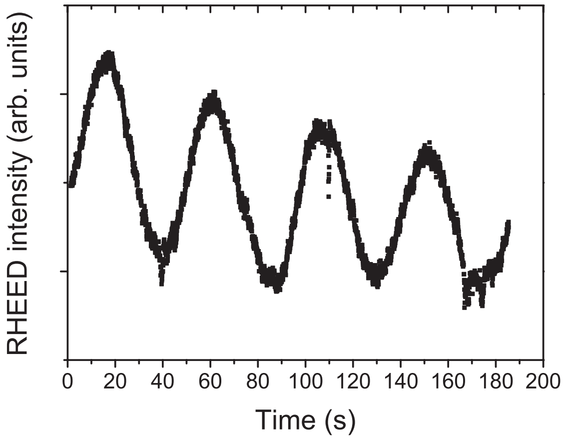

Figure 3.33: RHEED intensity oscillations during the QW growth at 550°C for a QW grown using both NH_3 and N-plasma.

demonstrated that the simultaneous use of both sources allows to overcome the limitations of NH_3-MBE and grow indium-rich InGaN alloys.

The growth window for NH_3-MBE grown InGaN set by indium desorption and NH_3 efficiency is rather sharp, but unpublished work from our previous co-worker Dr. Amelie Dussaigne showed that it is possible to achieved green emission with a 2.5 nm QW grown by NH_3-MBE at 550°C using an additional N-plasma. To understand this behavior, a series of QWs have been grown, using 300 sccm NH_3 and 1 sccm N_2 at a plasma RF power of 360 W. High excitation power PL ($>10^5$ W/cm^2) was performed to extract the In concentration by achieving flat band conditions. A linear dependency between In flux and In incorporation is found when the two sources are used simultaneously (Fig. 3.32), and an In concentration above 40% is reached. When only NH_3 is used, the In concentration in the QW remains around 20%, as discussed in the previous part 3.3.1. This supports the assumption that the growth is nitrogen-limited when using only NH_3.

Before the growth of the InGaN QW, a GaN buffer is grown at 800°C with 100 sccm NH_3, with a thickness over 1 μm (hillock regime). The 2.5 nm-thick InGaN QW is grown at 550°C with both 300 sccm NH_3 and 1 sccm N-plasma (360 W RF power) with a V_{gr} of around 10 nm/h. After completing the InGaN layer, the NH_3 flux is stopped, the shutter of the N-plasma cell is closed, and the temperature is ramped up quickly. This step is used to improve the abruptness of the top interface by removing any remaining In excess from the surface [169]. At around 700°C the NH_3 flux is started again, to avoid desorption of the InGaN layer itself. Finally, while ramping from 750°C to 800°C, a 30nm GaN cap layer is grown for about 2 minutes, under the same conditions as the buffer layer. These growth conditions are nitrogen-rich, not only for the GaN buffer and cap, but also for the active region. The active layer is grown in a layer-by-layer growth mode, as seen by the presence of RHEED oscillations (Fig. 3.33), and follows smoothly the steps of the underlaying GaN buffer, leading to a homogeneous QW thickness as seen by HR-TEM in Fig. 2.47 (part 2.6.1). The slow RHEED oscillations allow a precise *in situ* measurement of V_{gr} and thus a very precise control of the QW thickness. It is worth noting that at this temperature no RHEED oscillations of GaN growth is observed, just a spotty RHEED pattern. Indeed, In acts as a surfactant during InGaN growth.

While it is possible to grow high indium content InGaN alloys by both traditional PAMBE and by NH_3-MBE with additional N-plasma, the crystalline quality might be limited due to the low T_{gr}. At very low T_{gr}, the point defect density can be strongly increased. The point defect creation is tied to their formation energy and the existence of kinetic barriers. The formation energy E^f is correlated to the equilibrium-concentration C_{eq} of a defect [170]:

$$C_{\text{eq}} = N_{\text{sites}} N_{\text{config}} \exp\left(-E^f/kT\right), \tag{3.4}$$

with N_{sites} the number of sites per lattice unit where the defect can be located, N_{config} the number of equivalent configurations in which the defect can be incorporated (usually 1 for vacancies, substitutions or antisites [170]), k the Boltzmann constant and T the temperature. This equation holds true for thermal equilibrium conditions only. Higher temperatures enhance the diffusion which tends to homogenize or out-anneal point defects that exceed their equilibrium concentration. At temperatures below the equilibrium one, kinetic barriers can freeze the defects in place and thus allows to exceed the equilibrium defect concentration, as kinetic barriers can limit the diffusion [170, p. 3854]. Therefore, a higher point defect concentration can be expected in layers grown at low temperature. As the typical growth temperatures for MOVPE are much closer to thermal equilibrium than the MBE ones, MOVPE grown InGaN QWs could exhibit a lower point defect density than MBE grown ones. In order to reduce the point defect density, one can increase T_{gr} and compensate the loss of indium, or apply a TA to improve the material quality (as seen for MOVPE grown QWs in part 3.2.4). These two options will be discussed thereafter.

When increasing T_{gr}, the reduction in indium content leads to a blueshift, to a reduction in FWHM, and to an increase in the RT PL intensity, as observed in Fig. 3.34. However, at T_{gr} = 640°C, nearly no In is incorporated as the In decomposition is strong: the observed weak peak corresponds to a QW with roughly 2% In. Enhanced In desorption was countered with a larger

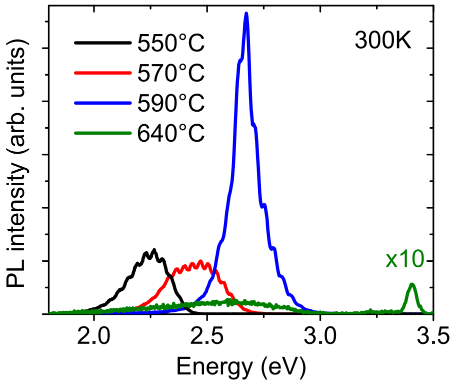

Figure 3.34: RT PL spectra of MBE grown InGaN QWs (with both, NH_3 and N-plasma) for different T_{gr}.

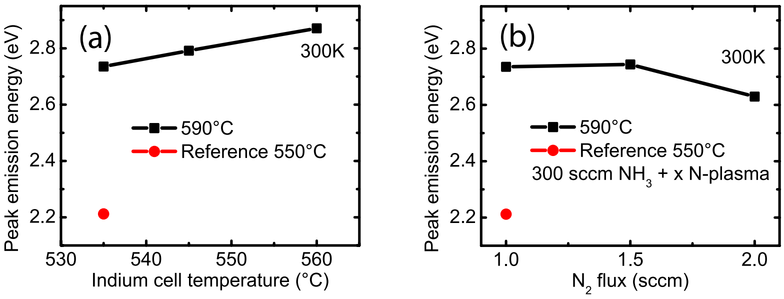

Figure 3.35: Peak emission energy for QWs grown at higher growth temperature and with (a) variations in indium flux and (b) variations in the N-plasma flux (for a fixed In flux)

In flux (Fig. 3.35 (a)) and an increased nitrogen-plasma flux (Fig. 3.35 (b)). Increasing the indium flux does not increase the indium incorporation, but increasing the nitrogen flux does. This is expected, as nitrogen-desorption should be the limiting factor. Note that increasing the In flux actually reduces the indium incorporation, which might be caused by surface site screening. Nevertheless, only a slight change in indium incorporation was realized by doubling the nitrogen flux. Strongly increasing it should allow a higher indium incorporation: it is reported that the best reported InGaN LD structures (emitting up to 500 nm when optically pumped) grown by PAMBE have been grown at elevated temperatures (above 620°C) with a huge nitrogen flux [57, 58], using two nitrogen plasma cells simultaneously. In addition, V_{gr} might need to be increased to reduce the desorption further, but this would reduce the amount of active nitrogen from the NH_3 dissociation.

While it is thus reasonable to assume that the low T_{gr} limits the material quality, the very high N^* flux, which is needed to enhance In incorporation at elevated temperatures, makes it challenging to achieve green emission when growing at high T_{gr}.

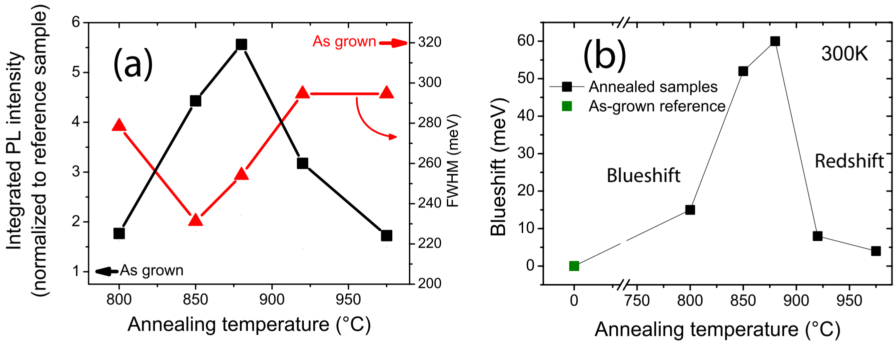

Figure 3.36: (a) Integrated RT PL intensity of the annealed samples and corresponding FWHM over the annealing temperature. The intensities are normalized to the as-grown reference. In (b) the blueshift of the annealed samples with respect to the as-grown one are shown.

3.4 Thermal annealing of MBE grown InGaN QWs

As an increase in T_{gr} is limited, a post-growth TA might be an option to improve the material quality, as a slight improvement was observed for MOVPE grown QWs with a similar indium content (part 3.2.4). It should be mentioned here that for InGaAs it has been also shown that material which is grown at a too low T_{gr} can recover its emission intensity by annealing [171]. For more information about the case of InGa(N)As, where similar features have been observed, the reader is referred to appendix A. As the MBE QWs are grown at much lower T_{gr} than their MOVPE counterparts, a stronger beneficial effect of TA could be expected.

To investigate the effect of a thermal budget, samples with a 2.5 nm-thick SQW with 25 % indium, emitting at about 2.35 eV, were annealed *ex situ* during 2h, in a HVPE reactor, under NH_3 atmosphere to avoid degradation of the 30 nm cap layer. T_a was varied from 800°C (T_{gr} of the cap) to 975°C. In Fig. 3.36 (a), the integrated RT PL intensity of the annealed samples (normalized to the value of the as-grown reference) and the corresponding FWHM are plotted over T_a. When increasing T_a from 800°C up to 880°C, a strong increase in PL intensity is observed, up to roughly a factor of 6 compared to the as-grown reference. At higher T_a, the PL intensity drops, indicating the beginning of the degradation of the QW. In parallel, the linewidth of the PL emission reduces until T_a = 850°C and increases for higher T_a. The TA also causes a blueshift (see Fig. 3.36 (b)) until T_a = 880°C and a redshift afterwards. The reduction in FWHM and the blueshift can be tentatively attributed to a homogenization of indium content in the layer, and the redshift and increase in linewidth to a beginning degradation, which is discussed later. In Fig. 3.37 (a), the RT spectra of the as-grown reference and the sample annealed at 880°C are shown to highlight the different PL intensities. The evolution of the PL peak position over temperature (Fig. 3.37 (b)) supports the interpretation that a homogenization of the indium distribution takes place. Indeed, there is a blueshift in the annealed sample which is accompanied by the suppression of the s-shape behavior of the reference sample. This is an indication that the lowest energy states have been suppressed during annealing, which is consistent with the reduction in the FWHM. Interestingly, the same behavior of PL intensity and FWHM is observed not only for annealed InGaN QWs, but also

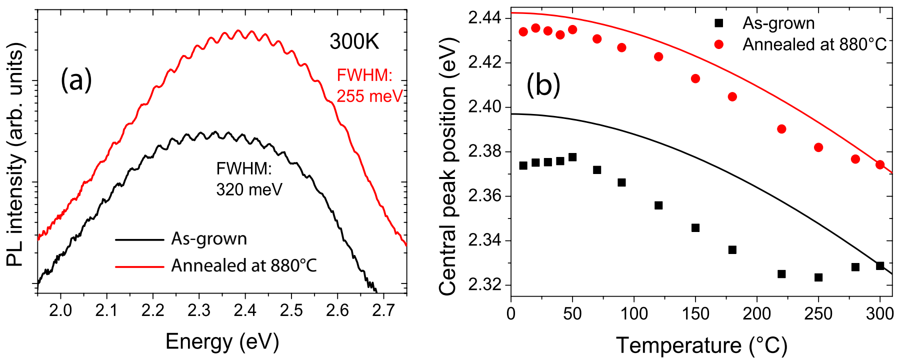

Figure 3.37: In (a) the PL RT spectra of the as-grown QW and after annealing at 880°C are shown. In (b) the evolution of the peak position with the temperature of the two samples is displayed (the lines indicated varshni plots).

Table 3.2: The surface rms roughness (measured by AFM for 10 x 10 μm^2 images) and the corresponding values for PL intensities and IQE are listed.

T_a in °C:	as-grown	800	850	880	920	975
rms roughness for 10 x 10 μ m^2 (nm)	10.9	10.9	7.1	5.7	2.5	5.0
Int. PL intensity at 10K (a. u.) :	6.993	6.090	6.632	6.183	6.234	7.609
Int. PL intensity at 300K (a. u.):	0.051	0.090	0.225	0.282	0.161	0.088
IQE (%)	0.7	1.4	3.4	4.5	2.6	1.2

for the arsenide GaInNAs system [172].

There are two possible origins for the strong improvement in the RT integrated PL intensity: an increase in light extraction efficiency or an increase in internal quantum efficiency (IQE). Light extraction efficiency could enhanced due to the surface roughness [173] increasing during TA. In that case, the improvement should be the same at 10K, as a difference in extraction efficiency is not affected by temperature. On the contrary, if the higher PL intensity is due to an increase in IQE, the improvement should vanish at 10K, where the effect of non-radiative recombinations can be neglected. Consequently, the PL intensities should be similar at low temperatures in the latter case, as observed for the MOVPE QWs grown on sapphire (see part 3.2.4). In addition, a similar or reduced surface roughness would also point towards an increase in IQE as origin of the PL improvement.

The surface morphology changes upon TA (Fig. 3.38). It can be seen that for a T_a >900°C the hexagonal mounds gets rounder. In fact, the surface gets smoother and reduction in rms surface roughness is already observed for a T_a >800°C (see Tab. 3.2). The sample annealed at T_a =920°C exhibits even a rms roughness that is 4 times lower than the as-grown reference one. This rules out a higher light extraction efficiency for the annealed samples. Actually, the light extraction might even be slightly higher for the as-grown reference one. The evolution of the integrated PL intensity with the temperature, displayed in Fig. 3.39, supports this. The intensity of all the samples is roughly the same at 10K, similar to what was observed for

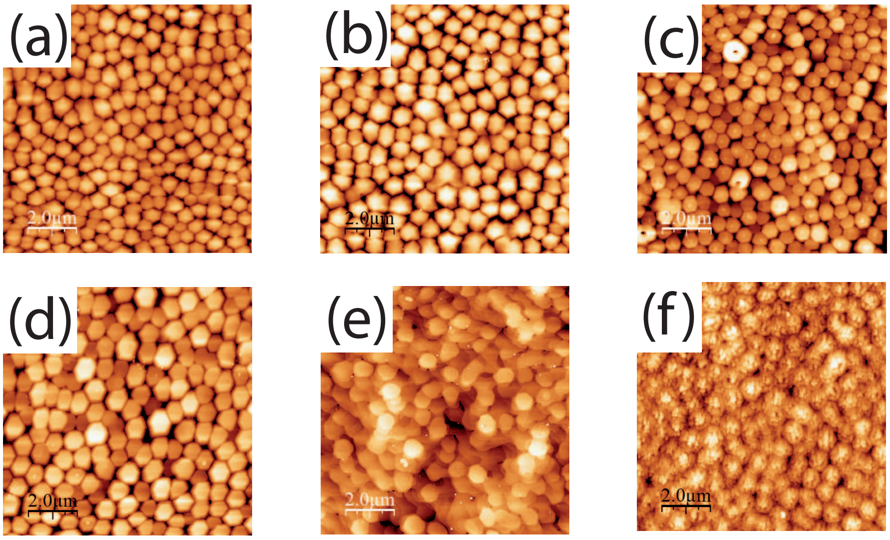

Figure 3.38: 10 x 10 μm^2 AFM images of NH_3-MBE grown InGaN QWs with a 30 nm GaN cap (a) as grown, and upon thermal annealing at (b) 800°C, (c) 850°C, (d) 880°C, (e) 920°C and (f) 975°C.

comparable MOVPE QWs in part 3.2.4. Therefore, light extraction efficiency is ruled out as the origin of the improved integrated PL intensity by both AFM and PL measurements.

However, the intensity drop is different from one sample to the other. The ratio of the integrated PL intensity at RT over the integrated PL intensity at 10K provides, in a first approximation, an indicative value of the IQE. As listed in Tab. 3.2, the IQE of the QW is increased upon TA and the maximum is obtained at T_a = 880°C with an increase of a factor of over 6. Interestingly to note, the improvement in integrated PL intensity upon annealing is larger than for MOVPE grown QWs with the same indium content (Fig. 3.23). However it is lower than what was observed for MOVPE grown QWs with a higher indium content (Fig. 3.21). It can

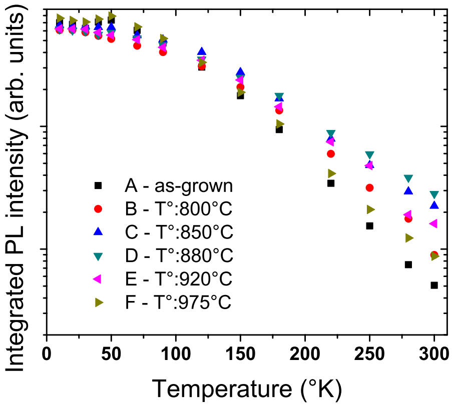

Figure 3.39: Integrated PL intensity of the as-grown and annealed samples over the temperature.

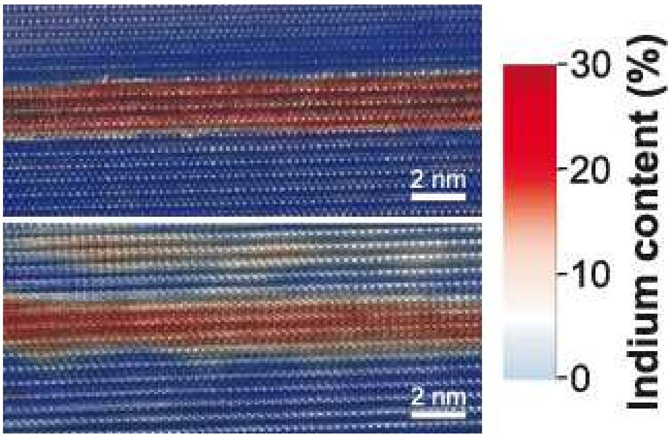

Figure 3.40: A HR-TEM image of the sample annealed at 880°C (top) and the as-grown reference (bottom). The overlaid color code indicates the indium distribution measured by strain analysis.

thus be tentatively concluded that both T_{gr} and indium content determine the magnitude of improvement that can be achieved by TA. The improved IQE could be attributed to either a reduction in non-radiative recombination centers (*i.e.* point defects) upon TA or to an improved localization due to formation of indium-rich clusters or even QD formation.

HR-TEM was performed on the as-grown reference and the sample annealed at 880°C, since it shows the highest improvement in terms of IQE (3.40). For both samples, the QW interfaces are sharp and show no sign of In clusters or QD formation. The as-grown QW is slightly more inhomogeneous than the annealed sample, with tiny indium-rich clusters which are dissolved by annealing at 880°C. Simulating the QW emission energy using the indium concentration measured by HR-TEM (25% and 24% for the as-grown and annealed samples, respectively) leads to the same blueshift as observed on PL measurements. Additionally, a reduction in the FWHM of the PL is observed for this sample compared to the as-grown one, indicating a more homogeneous InGaN layer. Finally, the behavior of the peak position over temperature supports this explanation (Fig. 3.37 (b)), as a shallower localization is observed at 10K. As indium clustering and QD formation can both be ruled out by HR-TEM and PL, the strongly improved IQE for the sample annealed at 880°C is probably due to a reduction of non-radiative recombination centers by point defect curing (PDC).

The initial improvement is followed by a degradation at a T_a >880°C, characterized by the drop of the IQE. Such a behavior was also observed for MOVPE grown InGaN QWs (see part 3.2.1) as well as for GaInNAs QWs [174]. The increase in FWHM and the redshift at higher T_a (Fig. 3.36) can be explained by degradation of the QW interfaces and the formation of In-rich clusters (see part 3.2.2). The loss of interfaces is confirmed by TEM performed on the samples annealed at 920°C (Fig. 3.41 (a)) and at 975°C (Fig. 3.41 (b)), where QDs start to form. Here, it should be mentioned that no dark spots were observed on the fluorescence maps of this sample. However, another MBE sample with a higher In content QW annealed at 975°C showed dark spots areas as well as blue luminescence, as described for highly degraded

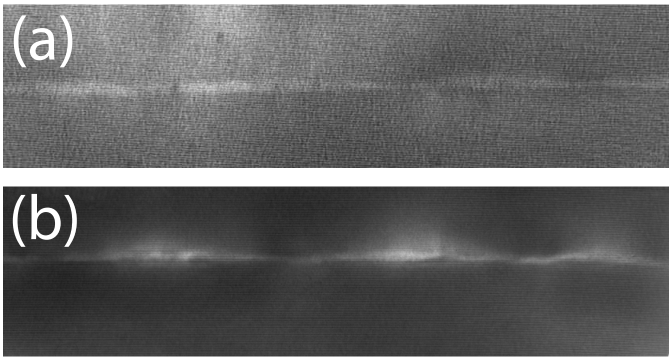

Figure 3.41: TEM images of the QW samples annealed at (a) 920° and (b) 975°C.

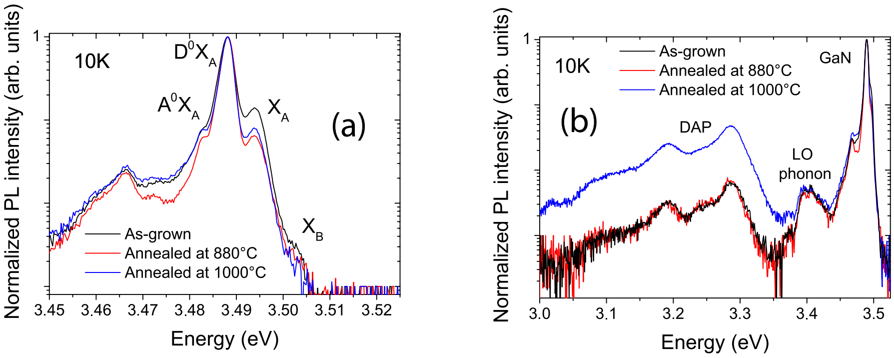

Figure 3.42: Normalized PL spectra of annealed MBE-grown GaN at 10K. In (a) GaN peak is shown, while in (b) the wider energy range includes the donor-acceptor pair peak.

MOVPE QWs (part 3.2.2). This indicates that the formation of metallic indium clusters takes place in MBE grown InGaN QWs as well.

Now one should look at the effect of TA on the GaN barrier itself. In Fig. 3.42 the 10K PL spectra of GaN grown at 800°C by NH_3-MBE is shown for the as-grown reference, as well as for two TA steps (T_a =880°C and T_a =1000°C). The GaN annealed at 880°C shows a slightly less intense exciton peak X_A with respect to the donor bound (D^0X_A) and acceptor bound (A^0X_A) exciton ones. However, when the GaN is annealed at 1000°C, it shows a strong increase in the DAP peak with respect to the GaN peak. The increase could originate from additional defects created at the surface or in the bulk during the annealing step. This increase in the DAP peak at high T_a indicates that there is a limit for TA after which the quality of the GaN itself can degrade, at least for the annealing conditions used in this work.

The improvement in IQE is tentatively attributed to a reduction of non-radiative recombinations by a PDC and not to a stronger localization. To gain further insight, it is important to investigate if only the QW itself or also the barrier is improved. This can be done by probing the QW pumping into the barrier or directly into the QW. In the former case, the carriers are photogenerated in the barrier region and have to diffuse into the well during which they can recombine non-radiatively in the presence of defects. In contrast, pumping only into the QW,

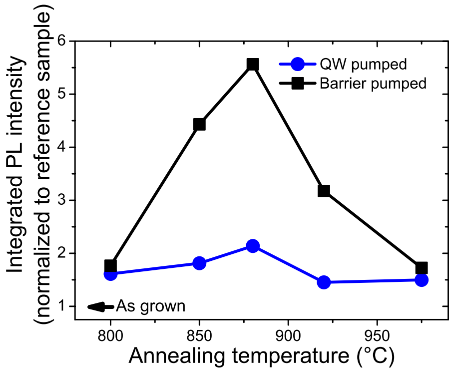

Figure 3.43: Integrated RT PL intensity, normalized to the as-grown value, as a function of the annealing temperature, when pumping into the barrier (black squares) or into the QW (blue circles).

allows to probe the reduction in non-radiative recombinations in the QW. In Fig. 3.43 the integrated RT PL intensity as a function of T$_a$ is displayed for both excitation energies (using a HeCd emitting at 325 nm to pump into the GaN and an InGaN LD emitting at 375 nm to only pump the QW). Note that the intensities are normalized to the as-grown reference sample. The improvement at T$_a$ =800°C is about the same for both pumping energies. This indicates that at this temperature, nearly all of the improvement originates from the QW. Note that since the buffer layer and also the cap layer are grown at approximately the annealing temperature, no improvement is expected for these layers. As the cap layer is 30 nm-thin (about two minutes at 800°C), which corresponds to only a small thermal budget introduced onto the underlaying active InGaN region, negligible compared to the 2 h TA.

When increasing T$_a$ (>800°C), the barrier starts to become the main contributor of the improvement, with a much stronger increase in PL intensity than for the QW. Note that it is not possible to distinguish between the curing of native defects from the barriers, created during the barrier growth itself, and defects that diffused from the QW plane into the barriers and got cured there.

The question remains whether the improvement is indeed due to point defects being cured or passivated by the annealing process. To gain further insight, the effect of the TA on the evolution of the carriers over time is investigated by time-resolved PL (TRPL), performed in Montpellier. First, the basics of TRPL are quickly introduced. The samples are excited with an ultra-short laser pulse. The change in carrier population in the QW (n) over time is given by:

$$\frac{dn}{dt} = n_0 * \delta(t) * \frac{1}{\tau_{dec}}, \tag{3.5}$$

with τ_{dec} the decay time. Here, the ultra-short excitation pulse (at time 0) is expressed by a delta function. This holds if the carriers are excited directly in the QW. Otherwise, they are mainly excited in the barriers. Consequently, the delta function in Eq. 3.5 has to be replaced

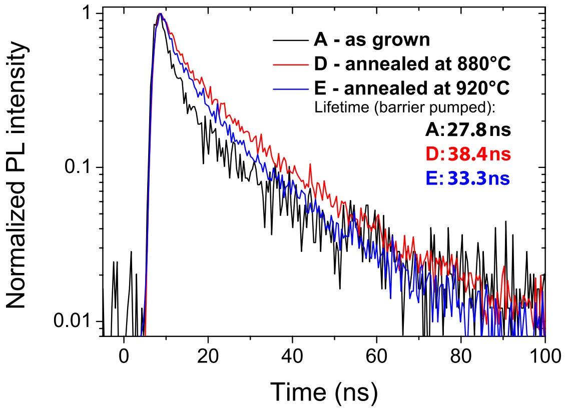

Figure 3.44: Integrated PL intensity of the as-grown sample and the samples annealed at 880°C and 920°C are displayed over time. Lifetimes are indicated for each sample.

by a term allowing for the diffusion from the barriers into the QW:

$$\frac{dn}{dt} = n_0 * e^{\frac{t}{\tau_{diff}}} * (\frac{1}{\tau_{dec}}), \tag{3.6}$$

with τ_{diff} the diffusion time. The decay time τ_{dec} has two components, the radiative decay time τ_r and the non-radiative decay time τ_{nr}, and is given by:

$$\frac{1}{\tau_{dec}} = \frac{1}{\tau_r} + \frac{1}{\tau_{nr}}. \tag{3.7}$$

τ_r corresponds to radiative transitions where a photon is created. On the other hand, τ_{nr} covers all non-radiative processes. At low temperatures, τ_{nr} is very long , and consequently, the recombinations are mainly governed by radiative transitions. However, with increasing temperature, τ_{nr} gets smaller and non-radiative transitions become more and more dominant. At high temperatures, the decay time mainly depends on the non-radiative recombinations. A reduction in non-radiative recombination centers, such as point defects, would thus lead to an increased lifetime. The lifetime is used here as the time it takes for the intensity to drop to a 10th of its initial value.

TRPL was performed during a visit to the Laboratoire Charles Coulomb in Montpellier, using the third harmonic of a mode-locked Ti:sapphire laser (at 266 nm, thus pumping into the GaN barriers and not only into the QW). The integration was performed for the same window around the central wavelength for all samples. The measurement temperature was set to 266K. At this temperature, non-radiative recombinations are already dominant. In Fig. 3.44, the integrated TRPL intensity over time is displayed for the as-grown sample and the samples annealed at 880°C and 920°C. The lifetime starts at 27.8 ns (for the as-grown reference), increases with T$_a$ and peaks for the sample at 880°C at 38.4 ns, before it drops again slightly to 33.3 ns for the sample annealed at 920°C. Assuming the non-radiative recombinations are dominant, the increased lifetime indicates a reduction in non-radiative recombinations for the annealed samples. This agrees very well with the observed improvement in IQE, indicating a reduction in the non-radiative recombination centers and thus a PDC.

Overview for InGaN QWs grown by NH_3-MBE

In the second part of this chapter, In-rich InGaN QWs grown by NH_3-MBE were investigated. First, it was shown that the limitation in indium incorporation for NH_3-MBE originates from the amount of N^* which is limited per unit of time. The combination of two nitrogen sources, NH_3 and N-plasma, allows to obtain QWs with a very high indium content. The low efficiency of the QWs could not be overcome by increasing T_{gr} due to enhanced desorption. However, by utilizing a post-growth TA step, it is possible to strongly enhance the RT PL emission of high indium content InGaN QWs grown at 550°C by NH_3-MBE. The TA improves the IQE by curing point defects out of the active region and the barriers area around it. At higher T_a, the high indium content QWs degrades. A similar behavior is observed for the MOVPE samples (part 3.1). The main result is the increase in RT PL emission by a factor of 6 with a simultaneous reduction in FWHM upon annealing. In combination with the improvement observed for MOVPE QWs, it can be assumed that both a high indium content and a low T_{gr} enhance the window for improvement by TA, as the improvement in PL intensity is more pronounced for MBE QWs than for MOPVE QWs (with the same In content).

3.5 Point defect curing

Indium-rich InGaN QWs that were not exposed to any thermal budget exhibit an increased RT PL emission upon TA. This takes place for both MOVPE and MBE grown QWs. This effect is stronger in MBE QWs, as their T_{gr} is lower. As described in part 3.3.2, point defects are likely to exceed the equilibrium concentration at low T_{gr}, and might be “frozen”. As already mentioned in the previous part, the potential improvement depends on both the indium content and the QW growth temperature. Interestingly, the best improvement happens around a similar temperature (850°C - 880°C) for the investigated In-rich QWs grown by both techniques, hinting that the same type of defects might be affected.

One question that needs to be addressed is whether hydrogen could be responsible of the defect curing or not. Hydrogen passivation could take place during the annealing in NH_3 atmosphere, and surpass the effect of defect diffusion and annihilation (which could explain the curing without hydrogen). To investigate this, the MOVPE DQW sample with 35% indium (from series A) has been annealed at 850°C in N_2 atmosphere. The PL spectra of this annealed sample and an as-grown reference are shown in Fig. 3.45 for different temperatures. It can be cleary seen that the emission at 10K is about the same intensity, while an improvement in PL intensity is observed for the annealed sample at higher temperatures, similar to what is observed for annealing in NH_3 (see Fig. 3.21). This shows that a hydrogen passivation during

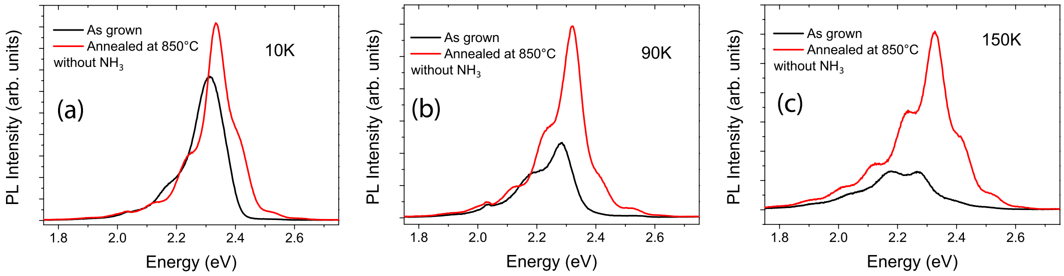

Figure 3.45: PL spectra of the sample with 35% In as-grown and annealed at 850°C without NH_3 at (a) 10K, (b) 90K and (c) 150K.

the annealing is unlikely to be responsible for the observed improvement in PL intensity. Therefore, point defect curing and not hydrogen passivation is likely at the origin of the improvement in quantum efficiency.

To investigate this in more detail, the point defects that are likely to appear in the III-nitrides - impurities, vacancies and interstitial - are discussed with a focus on their diffusion properties. One possibility are impurities, which can come from residual impurities inside the reactor or from the materials used. Their density could be enhanced for both, lower T_{gr} and lower V_{gr}. A second possibility are vacancies or interstitials. Their formation depends on the Fermi level and T_{gr} [154]. Note that for the diluted nitride system reviewed in the appendix, the presence of nitrogen affects the formation energy of Ga interstitial (Ga_I)[175], and for Mg-doped GaN, the formation energy of nitrogen vacancies (V_N) is supposed to be reduced. In the case of the III-nitrides, most research has been done on binary compounds, especially on GaN [176], as the quality of GaN layer is high enough to allow to study the material properties in depth, which is not the case for InGaN. Thus, to the author's best knowledge, it is not known whether the presence of indium at the growth front changes the formation energy of point defects. However, as In incorporation induces strain, it is likely that not only the diffusion, but also the formation of point defects around strained areas or dislocations might be affected [144].

To compare the results of the TA (parts 3.2 and 3.4) and to investigate which kind of defects could be possibly cured, it is worth taking a look at the activation energy (E_A) for the diffusion of the defects. It needs to be pointed out that the additional peak that appears at 2.75 eV for degraded samples is probably also due to additional point defects (namely V_N, V_{Ga} or GaO). However, the curing discussed here concerns the curing of defects that were created during growth and not introduce afterwards by the TA. First, the case of Ga vacancies (V_{Ga}) in GaN is considered. PAS was performed by Tuomisto *et al.* to study the effect of TA on V_{Ga} artificially created by irradiation of GaN [176]. Two regimes were identified: the first half of the V_{Ga} anneals out at low T_a (until 330°C), while the second anneals out completely at a temperature of 850°C [176]. This second temperature is very close to the T_a where the main improvement in RT PL was observed in this work (850°C - 880°C). The authors proposed that this second half of V_{Ga} is more stable with temperature because they could be stabilized by V_N or H [176]. A theoretical calculation of the vacancy-mediated activation energy for Ga diffusion has yielded a value between 3 eV and 4 eV, which corresponds to a temperature range above 800°C [154].

Note that to link the calculated E_A to a temperature, Limpijumnong and Van de Valle assumed a prefactor of $10^{13}s^{-1}$ and a hopping rate of s^{-1} [154, p. 8]. Chuo *et al.* [177] observed In and Ga interdiffusion between 900°C and 1050°C and measured an activation energy of 3.4 ± 0.5 eV. This data fits with the range where the TA-induced PL improvement is observed for both the annealed MOPVE and MBE QWs. However, the effect of T_{gr} might need to be taken into account. It is worth noting that for the GaInNAs system, the optimum annealing temperature and duration depends on the T_{gr} of the layer [174]. In case the defect density is T_{gr}-dependent, the diffusion length of the point defects should also depend on T_{gr}, meaning it could be easier to diffuse in a layer grown at LT.

V_N are more difficult to detect, as they are not negatively charged. PAS can only detect them if they form clusters with V_{Ga}. However, it is possible to look at the nitrogen-diffusion by growing a GaN/GaN/GaN sandwich structure (by PAMBE) where the middle layer is grown with a different nitrogen isotope [178]: Ambacher *et al.* investigated the diffusion of the nitrogen isotope (from the middle layer) during TA by SIMS. For the nitrogen diffusion an E_A of 4.1 eV ± 0.4 eV was found [178]. This E_A is close to the one that as been obtained by calculations for V_N (4.3 eV [154]). Again, these values are in good agreement with the temperature range where the improvement in RT PL was observed in this work (parts 3.2 and 3.4).

Concerning Ga or N interstitials (Ga_I or N_I respectively), little is known about their diffusion. A study which used electron paramagnetic resonance obtained an E_A of 0.7 eV for irradiation-induced Ga_I [179], and similar results have been obtained by calculations [154]. For N_i, no experimental data is known to the author's knowledge, but calculations indicate that they should become mobile at much lower temperatures as well (around 200°C [154]). Thus they are also unlikely to play a dominant role in the observed PDC.

For InGaN grown at 550°C, a small indication can be gathered from recent investigations on point defects in bulk InN performed by Rauch *et al.* [180]. InN grown by MOVPE at 500-550°C was investigated: when decreasing T_{gr} the structural, electrical, and optical properties were degraded and PAS indicated that low T_{gr} promotes the formation of V_{In} - nV_N vacancy complexes [180]. Again, this can be only taken as a possibility for the InGaN QWs under study.

To summarize, comparing the temperature range upon which the improvement in IQE occurs to theoretical calculation for point defect diffusion in bulk GaN (and InN), allows to assume that vacancies are more likely to play a role than interstitials or impurities.

4 Conclusion and outlook

The results of the study of the kinetic growth regime and its consequences are summarized first. In a second step, issues of InGaN QW growth and stability are revisited, before giving an outlook for future work and relevance for designing device structures.

The kinetic growth regime

When the growth temperature is low, as used for example for InGaN QWs and their surrounding barriers, the III-nitride growth is governed by kinetic effects, which are dominated by the asymmetry of attachment to a step-edge, called the Ehrlich-Schwöbel barrier. The ESB has a profound impact on both the micro- and the macrostructure: it suppresses the layer-by-layer growth mode and the step-flow growth mode and makes the growth mode unstable against perturbations.

As a consequence, three ESB-induced surface morphologies can be observed, depending on the growth conditions: mound (or hillock), finger (or step-meander) and step-bunching. In this work, these predicted morphologies have been demonstrated for GaN layers grown homoepitaxially by MOVPE, as well as MBE, and compared to a kinetic Monte Carlo simulation.

These morphologies consist of self-assembled features. Not only the type, but also the dimension can be controlled: on the one hand, the peak-to-valley ratio, or height of the pattern, depends on the thickness of the layer. On the other hand, the lateral feature size, or periodicity, scales with the growth rate and is independent of the layer thickness. Extracting the scaling parameter of the periodicity with the growth rate can allow to differentiate between a 2D kink or a 1D step Ehrlich-Schwöbel barrier (even though further theoretical investigations are needed to firmly conclude). The different morphologies that are usually reported by the different growth techniques (MOVPE, NH_3-MBE and PAMBE) are thus due to the use of different growth windows. Therefore, adjusting the growth parameters allows to achieve the desired surface morphology with all growth techniques. It is also possible to obtain smooth and flat morphologies by reducing or even eliminating the ESB-induced features. The effect of the ESB can be reduced:

a) by increasing the growth temperature, so that the energy of the adatoms is high enough to easily overpass the ESB,
b) by decreasing the growth rate, so that smoothening effects can counter the ESB-induced massflow, and
c) by using adlayers, which can not only affect the diffusion on the steps (surfactant effect), but can also provide a diffusion channel over the step-edges, which allows avoiding the ESB.

Thus adjusting the growth conditions provides a big toolbox to control the surface morphology. Finally, the ESB-induced morphology can have an impact on device performance since the local variations of the misorientation affect the indium incorporation. As a consequence, a finger-like pattern can be observed on the spatial distribution of the light emission of QWs grown on a finger-morphology. As the step-meander formation aligns on pinned dislocations, a self-screening of defects can take place and the ESB-induced morphology can therefore improve device performance, as demonstrated for a SQW InGaN LED.

However, several interesting questions remain that should be investigated in more depth in future research:

(i) the ESB seems to be relevant for other nitrides, as indicated by the presence of characteristic kinetic surface morphologies. For InAlN, where mounds are observed even if lattice-matched to GaN, the degradation of the crystalline quality could be due to diffusion deficits related to the ESB. Thus playing on the kinetics could allow to prevent the hillocks and achieve smoother morphologies.
(ii) it was observed that the growth on an underlaying InGaN layer has some impact on the subsequently grown GaN layers (due to strain, step width variation or a remaining surfactant effect). Thus it would be interesting to extend the research to include the interaction of the different layers in a structure. As a consequence, the growth conditions for a desired morphology need to be tested with the correct structure underneath.
(iii) here, it could not be determined if a SESE or a KESE is at the origin of the observed surface features. A systematical study using different offcut orientation could help to distinguish between them.

Thermal degradation of In-rich InGaN QWs

In the second part of the dissertation, the effect of a thermal budget on In-rich InGaN QWs was studied. The degradation threshold for In-rich InGaN depends on (i) the indium content, (ii) the QW thickness and (iii) the number of QWs. For In-rich QWs, the typical thermal budget of MOVPE p-type layer grown on top can already degrade the QWs. The degradation is characterized by the formation of dark spots where nearly no QW emission is observed. Even though their density and size seem to be enhanced by a high dislocation density, they also appear for QWs grown on FS GaN with a low dislocation density. Therefore, they are more likely connected to indium inhomogeneity, which could trigger the degradation.

The degraded samples exhibit a blue luminescence at 2.75 eV, which has been observed at the dark spot positions. Additionally, HR-TEM reveals the formation of metallic In cluster in the degraded samples. Consequently, this blue luminescence at 2.75 eV is tentatively attributed to V_N related transition, or less likely to V_{Ga} or GaO complex formation around the metal nanoclusters.

Defect annealing

In the case of NH_3-MBE, since the amount of active nitrogen from the NH_3 is limited at low growth temperatures, it is challenging to realize a high indium content. Hence N-plasma has been used simultaneously to achieve green emission. However, as the growth temperature is much lower than the degradation onset, thermal annealing is found first to strongly improve the QW PL emission for a certain range of moderate temperatures. An improvement of the RT PL intensity up to a factor of 6, combined with a reduction in the linewidth, has been observed for a green QW upon annealing. A similar but weaker improvement is also observed for MOVPE grown QWs with the same indium content (25%). However, for InGaN QWs with a higher In content (35%), a strong improvement is also observed for MOVPE grown QWs. This improvement is tentatively attributed to a point defect curing. It seems that not only the growth temperature but also the indium content affects the point defect formation. Note that these observations were made for QWs with a thin GaN cap layer. In the case of a complete device structure, the thermal budget induced by the subsequent layers, if grown at moderate temperatures, could already cure point defects. The different PL efficiencies between single and multiple QWs can be partly attributed to such a self-annealing. Finally, comparing the temperature range where the improvement is observed to the range where the different point defects in GaN become mobile, it seems that thermal annealing most likely induces vacancy out-diffusion, while H passivation is less likely.

Effect of a thermal budget on indium-rich QWs

To summarize, the following processes seem to take place in indium-rich InGaN QWs subject to a thermal budget:

a) a low thermal budget improves the homogeneity of the InGaN layer (by dissolving initially present indium-rich clusters) and cures point defects initially present in the as-grown layer.
b) at an intermediate thermal budget, the point defects continue to be cured, improving the material quality further. However, the QW interfaces start to get rougher and in- and out-of-plane indium diffusion starts to take place, leading to the formation of indium-rich clusters (probably partly enhanced by dislocations).
c) under a higher thermal budget, the In-N bonds start to break, leading to the appearance

of dark spots and metallic indium clusters as observed by fluorescence and HR-TEM, respectively. Blue luminescence is observed at the dark spots and is attributed to newly created point defects. The dark spot area grows with increasing the thermal budget, leaving less intact InGaN QW area to emit and thus causing the QW PL emission to vanish.

Outlook

In this work, a connection has been made between the physical origin of the observed morphologies of GaN and their effect on device performance. Understanding the origin of the self-assembled surface features not only allows to get rid of them, but also to use them on purpose. Controlled ESB-induced features could be of use for self-ordered nano- or microstructures. Such self-assembled patterns could allow aligning QDs without a prepatterning step, or fabricating quantum wires. Indeed, such an ordering has already been demonstrated for Ge dots on meandered Si. In addition, an alignment parallel to the offcut could be also realized this way.

For In-rich InGaN-based devices, two effects could influence the different observed efficiencies of MBE and MOVPE grown QWs: the different growth temperature and interaction of the growth-front with dislocations. The latter refers to the observation that the alignment of the ESB-induced features with dislocations is pronounced in MOVPE but not in MBE grown structures, which might be due to a different surface chemistry. The role of adatoms, especially indium, should be investigated in more depth to provide a more detailed understanding. In addition, further research is required to include plasma-assisted MBE grown QWs into the thermal annealing study.

The thermal budget places a strong limit on the growth conditions for indium-rich devices, but when the active region is grown at a low growth temperature, in order to incorporate indium, an annealing step could improve the material quality. So as a final outlook, two directions might be fruitful for highly indium-rich devices. First, an optimized annealing step combined with a low temperature p-type could allow for the fabrication of efficient MOVPE or MBE grown InGaN-based devices. High efficient devices with an even longer wavelength, pushing far into and/or beyond the green gap, could be realized this way. Note that both the buffer layer underneath as well as the InGaN alloy should be optimized to achieve a very homogeneous In distribution for LDs. Second, hybrid structures, which combine high efficiently In-rich MOVPE InGaN QW with low temperature MBE p-type layer, might be an option to combine the best of the two growth techniques.

A Review of the case of GaInNAs

One system that had issues related to too low T_{gr} and subsequently introduced point defects was GaIn(N)As. While InGaAs is well developed and allows the fabrication of high performance devices, the growth temperature needs to be reduced when willing to incorporate N, as nitrogen incorporation takes place at much lower temperatures than those commonly used for GaAs based devices [162]. At this temperature, the as-grown layers are of poor material quality and exhibits weak luminescence.

However, it was found out that it was possible to recover laser quality material by post-growth thermal annealing [162, 171, 174]. The intensity of the PL signal was increased drastically (by over 50 times), the FWHM of the peak got narrower and a small blue-shift was observed upon thermal annealing [171]. This improvement was attributed to an reduction in point densities upon annealing [171] - a point defect curing (PDC) - and on a homogenization of the N distribution. A few point that should be stressed and discussed into more detail:

First, the PL improvement is not limited to layers with N. An InGaAs QW grown at the same T_{gr} that is used for the GaInNAs QWs (so at a T_{gr} that is necessary for the N incorporation, but much lower than commonly used for InGaAs QWs) also exhibits very poor PL emission, and can also be improved by the same TA as the GaInNAs QWs [171]. Indeed, the PL intensity of a GaInNAs QW grown at the low T_{gr} can increase by nearly two orders of magnitude after TA and InGaAs QWs grown at the same LT grown conditions (just without N) and treated by the same TA process display the same (or even a bit higher) improvement in PL intensity, as shown in Fig. A.1 taken from Tournie *et al.* [171]. However, they do not exhibit a significant blue-shift after TA as observed for GaInNAs QWs.
Second, GaInNAs QWs grown at higher temperatures can show a spotty RHEED pattern and a low PL efficiency that is not enhanced by TA; however, the blue-shift takes still place [171]. This indicates that increasing T_{gr} does not lead to the desired effect.
Third, the effect of the TA depends on the growth temperature [174]. In fact, the optimum annealing time and temperature depend on the initial QW growth conditions: the lower the initial T_{gr}, the shorter the optimum TA duration and also the lower the optimum T_a. This is displayed in Tab A.1 taken from Geelhaar *et al.* [174].

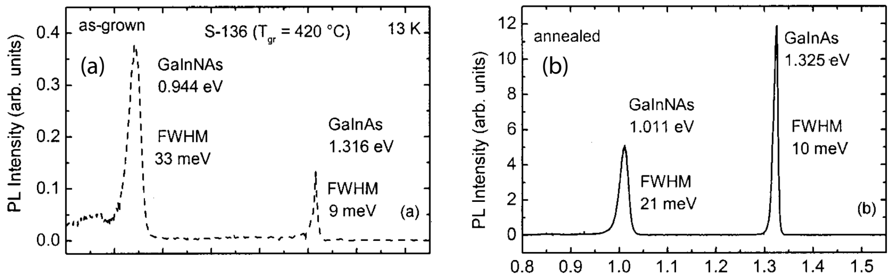

Figure A.1: Effect of TA on GaInNAs and GaInAs QWs grown at the same growth temperature, taken from Tournie *et al.* [171]: (a) as-grown and (b) annealed.

Table A.1: A table of the T_{gr} dependence of the effect of TA on GaInNAs QWs. The conditions for the best PL emission are listed, taken from Geelhaar *et al.* [174].

T_{gr} in ° C:	360	400	430	455	480
T_a in ° C:	600	600	630	690	750
Annealing duration in min:	30	30	30	30	70

Fourth, non-optimized annealing, e.g. too long and at too high T_a, leads also to a reduction in PL intensity [174]. This could be interpreted as a diffusion related effect.

And fifth, it should be also mentioned that the optimum PL intensity (after optimized annealing) was obtained for samples grown at moderate temperatures, as displayed in Fig. A.2 taken from Geelhaar *et al.* [174]. This indicates that the process of annealing of GaInNAs QWs is not straightforward and strongly dependends on the initial growth conditions.

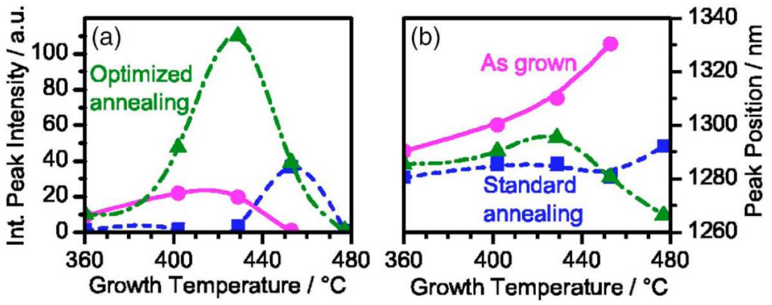

Figure A.2: Effect of TA on GaInNAs samples, taken from Geelhaar *et al.* [174]. (a) The PL intensity over the growth temperature is displayed for different thermal annealing procedures. (b) The peak position over the growth temperature is displayed.

Bibliography

[1] F Fichter, *On aluminium nitride*, ZEITSCHRIFT FUR ANORGANISCHE CHEMIE **54**, 322 (1907)

[2] WC Johnson, JB Parsons, MC Crew, *Nitrogen compounds of gallium III Gallic nitride*, JOURNAL OF PHYSICAL CHEMISTRY **36**, 2651 (1932)

[3] HP Maruska, JJ Tietjen, *Preparation and properties of vapor-deposited single-crystalline GaN*, APPLIED PHYSICS LETTERS **15**, 327 (1969)

[4] HM Manasevi, FM Erdmann, WI Simpson, *Use of metalorganics in preparation of semiconductor materials .4. nitrides of aluminium and gallium*, JOURNAL OF THE ELECTROCHEMICAL SOCIETY **118**, 1864 (1971)

[5] R Dingle, DD Sell, SE STOKOWSK, M Ilegems, *Absorption, reflectance, and luminescence of GaN epitaxial layers*, PHYSICAL REVIEW B **4**, 1211 (1971)

[6] JI Pankove, EA Miller, JE Berkeyhe, *GaN electroluminescent diodes*, RCA REVIEW **32**, 383 (1971)

[7] H Amano, M Kito, K Hiramatsu, I Akasaki, *P-type conduction in Mg-doped GaN treated with low-energy electron-beam irradiation (LEEBI)*, JAPANESE JOURNAL OF APPLIED PHYSICS PART 2-LETTERS **28**, L2112 (1989)

[8] S Nakamura, N Iwasa, M Senho, T Mukai, *Hole compensation mechanism of p-type GaN films*, JAPANESE JOURNAL OF APPLIED PHYSICS PART 1-REGULAR PAPERS SHORT NOTES & REVIEW PAPERS **31**, 1258 (1992)

[9] S Nakamura, T Mukai, M Senoh, *High-brightness InGaN/GaN double-heterostructure blue-green-light-emitting diodes*, JOURNAL OF APPLIED PHYSICS **76**, 8189 (1994)

[10] S Nakamura, T Mukai, M Senoh, *Candela-class high-brightness InGaN/AlGaN double-heterostructure blue-light-emitting diodes*, APPLIED PHYSICS LETTERS **64**, 1687 (1994)

[11] S Nakamura, N Senoh, N Iwasa, SI Nagahama, *High-brightness InGaN blue, green and yellow light-emitting-diodes with quantum-well structures*, JAPANESE JOURNAL OF APPLIED PHYSICS PART 2-LETTERS **34**, L797 (1995)

[12] S Nakamura, M Senoh, S Nagahama, N Iwasa, T Yamada, T Matsushita, H Kiyoku, Y Sugimoto, *InGaN-based multi-quantum-well-structure laser diodes*, JAPANESE JOURNAL OF APPLIED PHYSICS PART 2-LETTERS **35**, L74 (1996)

[13] J Wu, *When group-III nitrides go infrared: New properties and perspectives*, JOURNAL OF APPLIED PHYSICS **106**, 011101 (2009)

[14] JM Phillips, ME. Coltrin, MH Crawford, AJ Fischer, MR K, R Mueller-Mach, GO Mueller, Y O, LES R, JA Simmons, JY Tsao, *Research challenges to ultra-efficient inorganic solid-state lighting*, LASER & PHOTONICS REVIEWS **1**, 307 (2007)

[15] MR Krames, OB Shchekin, R Mueller-Mach, GO Mueller, L Zhou, G Harbers, MG Craford, *Status and future of high-power light-emitting diodes for solid-state lighting*, JOURNAL OF DISPLAY TECHNOLOGY **3**, 160 (2007)

[16] U Strauss, A Avramescu, T Lermer, D Queren, A Gomez-Iglesias, C Eichler, J Mueller, G Bruederl, S Lutgen, *Pros and cons of green InGaN laser on c-plane GaN*, PHYSICA STATUS SOLIDI B-BASIC SOLID STATE PHYSICS **248**, 652 (2011)

[17] A Avramescu, T Lermer, J Mueller, C Eichler, G Bruederl, M Sabathil, S Lutgen, U Strauss, *True Green Laser Diodes at 524 nm with 50 mW Continuous Wave Output Power on c-Plane GaN*, APPLIED PHYSICS EXPRESS **3**, 061003 (2010)

[18] T Miyoshi, S Masui, T Okada, Tomoya Y, T Kozaki, S Nagahama, T Mukai, *510-515 nm InGaN-Based Green Laser Diodes on c-Plane GaN Substrate*, APPLIED PHYSICS EXPRESS **2**, 062201 (2009)

[19] Y Enya, Y Yoshizumi, T Kyono, K Akita, M Ueno, M Adachi, T Sumitomo, S Tokuyama, T Ikegami, K Katayama, T Nakamura, *531 nm Green Lasing of InGaN Based Laser Diodes on Semi-Polar {20(2)over-bar1} Free-Standing GaN Substrates*, APPLIED PHYSICS EXPRESS **2**, 082101 (2009)

[20] A Avramescu, T Lermer, J Mueller, S Tautz, D Queren, S Lutgen, U Strauss, *InGaN laser diodes with 50 mW output power emitting at 515 nm*, APPLIED PHYSICS LETTERS **95**, 071103 (2009)

[21] Tim Boettcher, *Heteroepitaxy of Group-III-Nitrides for the Application in Laser Diodes*, Dissertation, University of Bremen (2002)

[22] G Dhanaraj, K Byrappa, V Prasad, M Dudley (Hg.), *Springer Handbook of Crystal Growth* (Springer, 2010)

[23] Marius Grundmann, *The Physics of Semiconductors* (Springer, 2010)

[24] ME Levinshtein, SL Rumyantsev, M Shur, *Properties of Advanced Semiconductor Materials: GaN, AlN, InN, BN, SiC, SiGe* (Wiley, 2001)

[25] I Vurgaftman, JR Meyer, *Band parameters for nitrogen-containing semiconductors*, JOURNAL OF APPLIED PHYSICS **94**, 3675 (2003)

[26] RAR Leute, M Feneberg, R Sauer, K Thonke, SB Thapa, F Scholz, Y Taniyasu, M Kasu, *Photoluminescence of highly excited AlN: Biexcitons and exciton-exciton scattering*, APPLIED PHYSICS LETTERS **95**, 031903 (2009)

[27] D Volm, K Oettinger, T Streibl, D Kovalev, M BenChorin, J Diener, BK Meyer, J Majewski, L Eckey, A Hoffmann, H Amano, I Akasaki, K Hiramatsu, T Detchprohm, *Exciton fine structure in undoped GaN epitaxial films*, PHYSICAL REVIEW B **53**, 16543 (1996)

[28] D Kovalev, B Averboukh, D Volm, BK Meyer, H Amano, I Akasaki, *Free exciton emission in GaN*, PHYSICAL REVIEW B **54**, 2518 (1996)

[29] F Bechstedt, F Fuchs, J Furthmueller, *Spectral properties of InN and its native oxide from first principles*, PHYSICA STATUS SOLIDI A-APPLICATIONS AND MATERIALS SCIENCE **207**, 1041 (2010), Fall Meeting of the European-Materials-Research-Society, Warsaw, POLAND, SEP 14-18, 2009

[30] C Wood, D Jena (Hg.), *Polarization Effects in Semiconductors* (Springer, 2008)

[31] G Martin, A Botchkarev, A Rockett, H Morkoc, *Valence-band discontinuities of wurtzite GaN, AlN, and InN heterojunctions measured by x-ray photoemission spectroscopy*, APPLIED PHYSICS LETTERS **68**, 2541 (1996)

[32] SR Lee, AF Wright, MH Crawford, GA Petersen, J Han, RM Biefeld, *The band-gap bowing of AlxGa1-xN alloys*, APPLIED PHYSICS LETTERS **74**, 3344 (1999)

[33] J Wu, W Walukiewicz, KM Yu, JW Ager, EE Haller, H Lu, WJ Schaff, *Small band gap bowing in In1-xGaxN alloys*, APPLIED PHYSICS LETTERS **80**, 4741 (2002)

[34] W Terashima, S Che, Y Ishitani, A Yoshikawa, *Growth and characterization of AlInN ternary alloys in whole composition range and fabrication of InN/AlInN multiple quantum wells by RF molecular beam epitaxy*, JAPANESE JOURNAL OF APPLIED PHYSICS PART 2-LETTERS & EXPRESS LETTERS **45**, L539 (2006)

[35] JF Carlin, M Ilegems, *High-quality AlInN for high index contrast Bragg mirrors lattice matched to GaN*, APPLIED PHYSICS LETTERS **83**, 668 (2003)

[36] L Liu, JH Edgar, *Substrates for gallium nitride epitaxy*, MATERIALS SCIENCE & ENGINEERING R-REPORTS **37**, 61 (2002)

[37] FC Frank, JH Vandermerwe, *One-dimensional dislocations .1. static theory*, PROCEEDINGS OF THE ROYAL SOCIETY OF LONDON SERIES A-MATHEMATICAL AND PHYSICAL SCIENCES **198**, 205 (1949)

[38] M Volmer, A Weber, *Germ-formation in oversaturated figures.*, ZEITSCHRIFT FUR PHYSIKALISCHE CHEMIE–STOCHIOMETRIE UND VERWANDTSCHAFTSLEHRE **119**, 277 (1926)

[39] IN Stranski, *On the theory of crystal accretion*, ZEITSCHRIFT FUR PHYSIKALISCHE CHEMIE–STOCHIOMETRIE UND VERWANDTSCHAFTSLEHRE **136**, 259 (1928)

[40] IN Stranski, *Uber die Energieschwellen beim Kristallwachstum*, NATURWISSENSCHAFTEN **37**, 289 (1950)

[41] WK Burton, N Cabrera, FC Frank, *The growth of crystals and the equilibrium structures of their surfaces*, PHILOSOPHICAL TRANSACTIONS OF THE ROYAL SOCIETY OF LONDON SERIES A-MATHEMATICAL AND PHYSICAL SCIENCES **243**, 299 (1951)

[42] JM Burgers, *Some considerations on the fields of stress connected with dislocations in a regular crystal lattice I*, PROCEEDINGS OF THE KONINKLIJKE NEDERLANDSE AKADEMIE VAN WETENSCHAPPEN **42**, 293 (1939)

[43] FC Frank, *The influence of dislocations on crystal growth*, DISCUSSIONS OF THE FARADAY SOCIETY 48–54 (1949)

[44] B Heying, EJ Tarsa, CR Elsass, P Fini, SP DenBaars, JS Speck, *Dislocation mediated surface morphology of GaN*, JOURNAL OF APPLIED PHYSICS **85**, 6470 (1999)

[45] XH Wu, P Fini, EJ Tarsa, B Heying, S Keller, UK Mishra, SP DenBaars, JS Speck, *Dislocation generation in GaN heteroepitaxy*, JOURNAL OF CRYSTAL GROWTH **189**, 231 (1998), 2nd International Conference on Nitride Semiconductors (ICNS 97), TOKUSHIMA CITY, JAPAN, OCT 27-31, 1997

[46] A Hangleiter, F Hitzel, C Netzel, D Fuhrmann, U Rossow, G Ade, P Hinze, *Suppression of nonradiative recombination by V-shaped pits in GaInN/GaN quantum wells produces a large increase in the light emission efficiency*, PHYSICAL REVIEW LETTERS **95**, 127402 (2005)

[47] J Bruckbauer, PR Edwards, T Wang, RW Martin, *High resolution cathodoluminescence hyperspectral imaging of surface features in InGaN/GaN multiple quantum well structures*, APPLIED PHYSICS LETTERS **98**, 141908 (2011)

[48] GB Stringfellow, *Microstructures produced during the epitaxial growth of InGaN alloys*, JOURNAL OF CRYSTAL GROWTH **312**, 735 (2010)

[49] KP O'Donnell, RW Martin, PG Middleton, *Origin of luminescence from InGaN diodes*, PHYSICAL REVIEW LETTERS **82**, 237 (1999)

[50] SE Bennett, DW Saxey, MJ. Kappers, JS Barnard, CJ Humphreys, GDW Smith, RA Oliver, *Atom probe tomography assessment of the impact of electron beam exposure on InxGa1-xN/GaN quantum wells*, APPLIED PHYSICS LETTERS **99**, 021906 (2011)

[51] D Watson-Parris, MJ Godfrey, P Dawson, RA Oliver, MJ Galtrey, MJ Kappers, CJ Humphreys, *Carrier localization mechanisms in InxGa1-xN/GaN quantum wells*, PHYSICAL REVIEW B **83**, 115321 (2011)

[52] Y Wu, R Shivaraman, KC Wang, JS Speck, *Analyzing the physical properties of InGaN multiple quantum well light emitting diodes from nano scale structure*, APPLIED PHYSICS LETTERS **101**, 083505 (2012)

[53] A Rosenauer, T Mehrtens, K Mueller, K Gries, M Schowalter, P Venkata Satyam, S Bley, C Tessarek, D Hommel, K Sebald, M Seyfried, J Gutowski, A Avramescu, K Engl, S Lutgen, *Composition mapping in InGaN by scanning transmission electron microscopy*, ULTRAMICROSCOPY **111**, 1316 (2011)

[54] T Lermer, I Pietzonka, A Avramescu, G Bruederl, J Mueller, S Lutgen, U Strauss, *Interdependency of surface morphology and wavelength fluctuations of indium-rich InGaN/GaN quantum wells*, PHYSICA STATUS SOLIDI A-APPLICATIONS AND MATERIALS SCIENCE **208**, 1199 (2011)

[55] RA Oliver, SE Bennett, T Zhu, DJ Beesley, MJ Kappers, DW Saxey, A Cerezo, CJ Humphreys, *Microstructural origins of localization in InGaN quantum wells*, JOURNAL OF PHYSICS D-APPLIED PHYSICS **43**, 354003 (2010)

[56] B Devaud, JY Emery, A Chomette, B Lambert, M Baudet, *Observation of one monolayer size fluctuations in a GaAs/GaAlAs superlattice*, APPLIED PHYSICS LETTERS **45**, 1078 (1984)

[57] M Siekacz, M Sawicka, H Turski, G Cywinski, A Khachapuridze, P Perlin, T Suski, M Bockowski, J Smalc-Koziorowska, M Krysko, R Kudrawiec, M Syperek, J Misiewicz, Z Wasilewski, S Porowski, C Skierbiszewski, *Optically pumped 500 nm InGaN green lasers grown by plasma-assisted molecular beam epitaxy*, JOURNAL OF APPLIED PHYSICS **110**, 063110 (2011)

[58] C Skierbiszewski, M Siekacz, H Turski, G Muziol, M Sawicka, A Feduniewicz-Zmuda, J Smalc-Koziorowska, P Perlin, S Grzanka, ZR Wasilewski, R Kucharski, S Porowski, *InGaN laser diodes operating at 450-460 nm grown by rf-plasma MBE*, JOURNAL OF VACUUM SCIENCE & TECHNOLOGY B **30**, 02B102 (2012)

[59] A Yoshikawa, E Ohshima, T Fukuda, H Tsuji, K Oshima, *Crystal growth of GaN by ammonothermal method*, JOURNAL OF CRYSTAL GROWTH **260**, 67 (2004)

[60] G Koblmuller, J Brown, R Averbeck, H Riechert, P Pongratz, JS Speck, *Ga adlayer governed surface defect evolution of (0001)GaN films grown by plasma-assisted molecular beam epitaxy*, JAPANESE JOURNAL OF APPLIED PHYSICS PART 2-LETTERS & EXPRESS LETTERS **44**, L906 (2005)

[61] CG Van de Walle, J Neugebauer, *First-principles surface phase diagram for hydrogen on GaN surfaces*, PHYSICAL REVIEW LETTERS **88**, 066103 (2002)

[62] A Dussaigne, B Damilano, J Brault, J Massies, E Feltin, N Grandjean, *High doping level in Mg-doped GaN layers grown at low temperature*, JOURNAL OF APPLIED PHYSICS **103**, 013110 (2008)

[63] CA Hurni, JR Lang, PG Burke, JS Speck, *Effects of growth temperature on Mg-doped GaN grown by ammonia molecular beam epitaxy*, APPLIED PHYSICS LETTERS **101**, 102106 (2012)

[64] JH Neave, BA Joyce, PJ Dobson, N Norton, *Dynamics of film growth of GaAs by MBE from RHEED observations*, APPLIED PHYSICS A-MATERIALS SCIENCE & PROCESSING **31**, 1 (1983)

[65] MA Moram, ME Vickers, *X-ray diffraction of III-nitrides*, REPORTS ON PROGRESS IN PHYSICS **72**, 036502 (2009)

[66] S Kret, P Dluzewski, A Szczepanska, M Zak, R Czerneck, M Krysko, M Leszczynski, G Maciejewski, *Homogenous indium distribution in InGaN/GaN laser active structure grown by LP-MOCVD on bulk GaN crystal revealed by transmission electron microscopy and x-ray diffraction*, NANOTECHNOLOGY **18**, 465707 (2007)

[67] C Misbah, O Pierre-Louis, Y Saito, *Crystal surfaces in and out of equilibrium: A modern view*, REVIEWS OF MODERN PHYSICS **82**, 981 (2010)

[68] G Ehrlich, FG Hudda, *Atomic view of surface self-diffusion - tungsten on tungsten*, JOURNAL OF CHEMICAL PHYSICS **44**, 1039 (1966)

[69] RL Schwoebel, EJ Shipsey, *Step motion on crystal surfaces*, JOURNAL OF APPLIED PHYSICS **37**, 3682 (1966)

[70] RL Schwoebel, *Step motion on crystal surfaces .2.*, JOURNAL OF APPLIED PHYSICS **40**, 614 (1969)

[71] J Villain, *Continuum models of crystal-growth from atomic-beams with and without desorption*, JOURNAL DE PHYSIQUE I **1**, 19 (1991)

[72] P Politi, J Villain, *Ehrlich-Schwoebel instability in molecular-beam epitaxy: A minimal model*, PHYSICAL REVIEW B **54**, 5114 (1996)

[73] P Politi, G Grenet, A Marty, A Ponchet, J Villain, *Instabilities in crystal growth by atomic or molecular beams*, PHYSICS REPORTS-REVIEW SECTION OF PHYSICS LETTERS **324**, 271 (2000)

[74] KA Bratland, YL Foo, JANT Soares, T Spila, P Desjardins, JE Greene, *Mechanism for epitaxial breakdown during low-temperature Ge(001) molecular beam epitaxy*, PHYSICAL REVIEW B **67**, 125322 (2003)

[75] N Galiana, PP Martin, C Munuera, M Varela, C Ocal, M Alonso, A Ruiz, *Pyramid-like nanostructures created by Si homoepitaxy on Si(001)*, MATERIALS SCIENCE IN SEMICONDUCTOR PROCESSING **12**, 52 (2009), 7th Workshop on Epitaxial Semiconductor on Patterned Substrate and Novel Index Surfaces (ESPS-NIS), Marseilles, FRANCE, APR, 2008

[76] J Krug, *Kinetic pattern formation at solid surfaces*, in Radons, G and Just, W and Haussler, P (Hg.), *COLLECTIVE DYNAMICS OF NONLINEAR AND DISORDERED SYSTEMS*, 5–37, WE Heraeus Fdn (SPRINGER-VERLAG BERLIN, HEIDELBERGER PLATZ 3, D-14197 BERLIN, GERMANY, 2005), WE Heraeus Summer School on Collective Dynamics of Nonlinear and Disordered Systems, Chemnits Univ Technol, Chemnitz, GERMANY, AUG, 2002

[77] T Maroutian, L Douillard, HJ Ernst, *Morphological instability of Cu vicinal surfaces during step-flow growth*, Phys. Rev. B **64**, 165401 (2001)

[78] RT Tung, F Schrey, *Topography of the Si(111) surface during silicon molecular-beam epitaxy*, PHYSICAL REVIEW LETTERS **63**, 1277 (1989)

[79] H Omi, T Ogino, *Growth-induced atomic step ordering on patterned and non-patterned Si(111)*, THIN SOLID FILMS **380**, 15 (2000), Spring Meeting of the European-Materials-Research-Society, STRASBOURG, FRANCE, MAY 29-JUN 02, 2000

[80] H Hibino, Y Homma, M Uwaha, T Ogino, *Step wandering induced by homoepitaxy on Si(111) during "1x1"-7x7 phase transition*, SURFACE SCIENCE **527**, L222 (2003)

[81] F Sanchez, G Herranz, IC Infante, J Fontcuberta, MV Garcia-Cuenca, C Ferrater, M Varela, *Critical effects of substrate terraces and steps morphology on the growth mode of epitaxial SrRuO3 films*, APPLIED PHYSICS LETTERS **85**, 1981 (2004)

[82] GS Bales, A Zangwill, *Morphological instability of a terrace edge during step-flow growth*, PHYSICAL REVIEW B **41**, 5500 (1990)

[83] M Rusanen, IT Koponen, J Heinonen, T Ala-Nissila, *Instability and wavelength selection during step flow growth of metal surfaces vicinal to fcc(001)*, PHYSICAL REVIEW LETTERS **86**, 5317 (2001)

[84] O Pierre-Louis, MR D'Orsogna, TL Einstein, *Edge Diffusion during Growth: The Kink Ehrlich-Schwoebel Effect and Resulting Instabilities*, Phys. Rev. Lett. **82**, 3661 (1999)

[85] MVR Murty, BH Cooper, *Instability in molecular beam epitaxy due to fast edge diffusion and corner diffusion barriers*, PHYSICAL REVIEW LETTERS **83**, 352 (1999)

[86] MG Lagally, ZY Zhang, *Materials science - Thin-film cliffhanger*, NATURE **417**, 907 (2002)

[87] SJ Liu, HC Huang, CH Woo, *Schwoebel-Ehrlich barrier: from two to three dimensions*, APPLIED PHYSICS LETTERS **80**, 3295 (2002)

[88] T Maroutian, L Douillard, HJ Ernst, *Wavelength selection in unstable homoepitaxial step flow growth*, PHYSICAL REVIEW LETTERS **83**, 4353 (1999)

[89] J Krug, *On the shape of wedding cakes*, JOURNAL OF STATISTICAL PHYSICS **87**, 505 (1997)

[90] J Kallunki, J Krug, M Kotrla, *Competing mechanisms for step meandering in unstable growth*, Phys. Rev. B **65**, 205411 (2002)

[91] M Vladimirova, A Pimpinelli, A Videcoq, *A new model of morphological instabilities during epitaxial growth: from step bunching to mounds formation*, JOURNAL OF CRYSTAL GROWTH **220**, 631 (2000)

[92] KA Bratland, YL Foo, P Desjardins, JE Greene, *Sn-enhanced epitaxial thickness during low-temperature Ge(001) molecular-beam epitaxy*, APPLIED PHYSICS LETTERS **82**, 4247 (2003)

[93] KA Bratland, YL Foo, T Spila, HS Seo, RT Haasch, P Desjardins, JE Greene, *Sn-mediated Ge/Ge(001) growth by low-temperature molecular-beam epitaxy: Surface smoothening and enhanced epitaxial thickness*, JOURNAL OF APPLIED PHYSICS **97**, 044904 (2005)

[94] H Zheng, MH Xie, HS Wu, QK Xue, *Kinetic energy barriers on the GaN(0001) surface: A nucleation study by scanning tunneling microscopy*, PHYSICAL REVIEW B **77**, 045303 (2008)

[95] S Vezian, F Natali, F Semond, J Massies, *From spiral growth to kinetic roughening in molecular-beam epitaxy of GaN(0001)*, PHYSICAL REVIEW B **69**, 125329 (2004)

[96] AL Corrion, F Wu, JS Speck, *Growth regimes during homoepitaxial growth of GaN by ammonia molecular beam epitaxy*, JOURNAL OF APPLIED PHYSICS **112**, 054903 (2012)

[97] Stephan Vezian, *Application de la microscopie nde locale de de la surface de GaN(0001)*, Dissertation, Universite de Nice-Sophia Antipolis (2000)

[98] MD Johnson, C Orme, AW Hunt, D Graff, J Sudijono, LM Sander, BG Orr, *Stable and unstable growth in molecular-beam epitaxy*, PHYSICAL REVIEW LETTERS **72**, 116 (1994)

[99] A Redinger, O Ricken, P Kuhn, A Raetz, A Voigt, J Krug, T Michely, *Spiral growth and step edge barriers*, PHYSICAL REVIEW LETTERS **100**, 035506 (2008)

[100] C Skierbiszewski, M Siekacz, P Perlin, A Feduniewicz-Zmuda, G Cywinski, I Grzegory, M Leszczyniski, ZR Wasilewski, S Porowski, *Role of dislocation-free GaN substrates in the growth of indium containing optoelectronic structures by plasma-assisted MBE*, JOURNAL OF CRYSTAL GROWTH **305**, 346 (2007), 4th International Workshop on Bulk Nitride Semiconductors, Makino, JAPAN, OCT 17-22, 2006

[101] M Sarzynski, M Leszczynski, M Krysko, JZ Domagala, R Czernecki, T Suski, *Influence of GaN substrate off-cut on properties of InGaN and AlGaN layers*, CRYSTAL RESEARCH AND TECHNOLOGY **47**, 321 (2012)

[102] TC Sadler, MJ Kappers, RA Oliver, *Optimisation of GaN overgrowth of InAlN for DBRs*, in Butte, R (Hg.), *PHYSICA STATUS SOLIDI C: CURRENT TOPICS IN SOLID STATE PHYSICS, VOL 6, SUPPL 2*, Band 6 von *Physica Status Solidi C-Current Topics in Solid State Physics*, S666–S670 (WILEY-V C H VERLAG GMBH, PAPPELALLEE 3, W-69469 WEINHEIM, GERMANY, 2009), International Workshop on Nitride Semiconductors, Montreux, SWITZERLAND, OCT 06-10, 2008

[103] S Sonderegger, E Feltin, M Merano, A Crottini, JF Carlin, R Sachot, B Deveaud, N Grandjean, JD Ganiere, *High spatial resolution picosecond cathodoluminescence of InGaN quantum wells*, APPLIED PHYSICS LETTERS **89**, 232109 (2006)

[104] JR Lang, JS Speck, *NH3-rich growth of InGaN and InGaN/GaN superlattices by NH3-based molecular beam epitaxy*, JOURNAL OF CRYSTAL GROWTH **346**, 50 (2012)

[105] G Koblmueller, F Wu, T Mates, JS Speck, S Fernandez-Garrido, E Calleja, *High electron mobility GaN grown under N-rich conditions by plasma-assisted molecular beam epitaxy*, APPLIED PHYSICS LETTERS **91**, 221905 (2007)

[106] G Koblmueller, F Reurings, F Tuomisto, JS Speck, *Influence of Ga/N ratio on morphology, vacancies, and electrical transport in GaN grown by molecular beam epitaxy at high temperature*, APPLIED PHYSICS LETTERS **97**, 191915 (2010)

[107] MH Xie, SM Seutter, WK Zhu, LX Zheng, HS Wu, SY Tong, *Anisotropic step-flow growth and island growth of GaN(0001) by molecular beam epitaxy*, PHYSICAL REVIEW LETTERS **82**, 2749 (1999)

[108] MVR Murty, P Fini, GB Stephenson, C Thompson, JA Eastman, A Munkholm, O Auciello, R Jothilingam, SP DenBaars, JS Speck, *Step bunching on the vicinal GaN(0001) surface*, PHYSICAL REVIEW B **62**, R10661 (2000)

[109] K Saarinen, T Laine, S Kuisma, J Nissila, P Hautojarvi, L Dobrzynski, JM Baranowski, K Pakula, R Stepniewski, M Wojdak, A Wysmolek, T Suski, M Leszczynski, I Grzegory, S Porowski, *Observation of native Ga vacancies in GaN by positron annihilation*, PHYSICAL REVIEW LETTERS **79**, 3030 (1997)

[110] R Willardson, E Weber, M Stavola (Hg.), *Identification of Defects in Semiconductors* (Academic Press, 1998)

[111] M Pristovsek, A Kadir, C Meissner, T Schwaner, M Leyer, M Kneissl, *Surface transition induced island formation on thin strained InGaN layers on GaN (0001) in metal-organic vapour phase epitaxy*, JOURNAL OF APPLIED PHYSICS **110**, 073527 (2011)

[112] A Matsuse, N Grandjean, B Damilano, J Massies, *Surface morphology of AlN and size dispersion of GaN quantum dots*, JOURNAL OF CRYSTAL GROWTH **274**, 387 (2005)

[113] M Himmerlich, S Krischok, V Lebedev, O Ambacher, JA Schaefer, *Morphology and surface electronic structure of MBE grown InN*, JOURNAL OF CRYSTAL GROWTH **306**, 6 (2007)

[114] G Biasiol, E Kapon, *Mechanism of self-limiting epitaxial growth on nonplanar substrates*, JOURNAL OF CRYSTAL GROWTH **201**, 62 (1999), 10th International Conference on Molecular Beam Epitaxy (MBE-X), CANNES, FRANCE, AUG 31-SEP 04, 1998

[115] G. Perillat-Merceroz, G. Cosendey, JF Carlin, R Butte, N Grandjean, *Intrinsic degradation mechanism of nearly lattice-matched InAlN layers grown on GaN substrates*, JOURNAL OF APPLIED PHYSICS **113**, 063506 (2013)

[116] G Cosendey, JF Carlin, NAK Kaufmann, R Butte, N Grandjean, *Strain compensation in AlInN/GaN multilayers on GaN substrates: Application to the realization of defect-free Bragg reflectors*, APPLIED PHYSICS LETTERS **98**, 181111 (2011)

[117] MA Zaluska-Kotur, F Krzyewski, S Krukowski, *Emergence of regular meandered step structure in simulated growth of GaN(0001) surface*, JOURNAL OF CRYSTAL GROWTH **343**, 138 (2012)

[118] MA Zaluska-Kotur, F Krzyzewski, *Step bunching process induced by the flow of steps at the sublimated crystal surface*, JOURNAL OF APPLIED PHYSICS **111**, 114311 (2012)

[119] MA Zaluska-Kotur, F Krzyzewski, S Krukowski, *Double step structure and meandering due to the many body interaction at GaN(0001) surface in N-rich conditions*, JOURNAL OF APPLIED PHYSICS **109**, 023515 (2011)

[120] MA Zaluska-Kotur, F Krzyzewski, S Krukowski, *Surface patterns due to step flow anisotropy formed in crystal growth process*, JOURNAL OF NON-CRYSTALLINE SOLIDS **356**, 1935 (2010), International Workshop on Functional and Nanostructured Materials (FNMA)/International Conference on Intermoleculat and Magnetic Interactions in Matter (IMIM), L'Aquila, ITALY, SEP 27-30, 2009

[121] MI Larsson, *Surface diffusion mechanism for step bunching*, PHYSICAL REVIEW B **56**, 15157 (1997)

[122] M Sawicka, H Turski, M Siekacz, J Smalc-Koziorowska, M Krysko, I Dziecielewski, I Grzegory, C Skierbiszewski, *Step-flow anisotropy of the m-plane GaN (1(1)over-bar00) grown under nitrogen-rich conditions by plasma-assisted molecular beam epitaxy*, PHYSICAL REVIEW B **83**, 245434 (2011)

[123] O Brandt, YJ Sun, L Daweritz, KH Ploog, *Ga adsorption and desorption kinetics on M-plane GaN*, PHYSICAL REVIEW B **69**, 165326 (2004)

[124] A Hirai, Z Jia, MC Schmidt, RM Farrell, SP DenBaars, S Nakamura, JS Speck, K Fujito, *Formation and reduction of pyramidal hillocks on m-plane {1100} GaN*, APPLIED PHYSICS LETTERS **91**, 191906 (2007)

[125] DJ As, *Cubic group-III nitride-based nanostructures-basics and applications in optoelectronics*, MICROELECTRONICS JOURNAL **40**, 204 (2009), Symposium on Wide Band Gap Semiconductor Nanostructures for Optoelectronic Applications held at the 2008 E-MRS Conference, Strasbourg, FRANCE, MAY, 2008

[126] J Neugebauer, TK Zywietz, M Scheffler, JE Northrup, H Chen, RM Feenstra, *Adatom Kinetics On and Below the Surface: The Existence of a New Diffusion Channel*, Phys. Rev. Lett. **90**, 056101 (2003)

[127] J Massies, N Grandjean, *Surfactant effect on the surface-diffusion length in epitaxial-growth*, PHYSICAL REVIEW B **48**, 8502 (1993)

[128] EL Piner, MK Behbehani, NA ElMasry, FG McIntosh, JC Roberts, KS Boutros, SM Bedair, *Effect of hydrogen on the indium incorporation in InGaN epitaxial films*, APPLIED PHYSICS LETTERS **70**, 461 (1997)

[129] O Ambacher, H Angerer, R Dimitrov, W Rieger, M Stutzmann, G Dollinger, A Bergmaier, *Hydrogen in gallium nitride grown by MOCVD*, PHYSICA STATUS SOLIDI A-APPLIED RESEARCH **159**, 105 (1997)

[130] EV Yakovlev, RA Talalaev, AS Segal, AV Lobanova, WV Lundin, EE Zavarin, MA Sinitsyn, AF Tsatsulnikov, AE Nikolaev, *Hydrogen effects in III-nitride MOVPE*, JOURNAL OF CRYSTAL GROWTH **310**, 4862 (2008), 14th International Conference on Metal Organic Vapor Phase Epitaxy, Metz, FRANCE, JUN 01-06, 2008

[131] W Bergbauer, M Strassburg, Ch Kolper, N Linder, C Roder, J Lahnemann, A Trampert, S Fundling, S F Li, H-H Wehmann, A Waag, *Continuous-flux MOVPE growth of position-controlled N-face GaN nanorods and embedded InGaN quantum wells*, Nanotechnology **21**, 305201 (2010)

[132] W Bergbauer, M Strassburg, Ch Koelper, N Linder, C Roder, J Laehnemann, A Trampert, S Fuendling, SF Li, HH Wehmann, A Waag, *N-face GaN nanorods: Continuous-flux MOVPE growth and morphological properties*, JOURNAL OF CRYSTAL GROWTH **315**, 164 (2011), 15th International Conference on Metalorganic Vapor Phase Epitaxy (ICMOVPE-XV), Incline Village, NV, MAY 23-28, 2010

[133] H Omi, T Ogino, *Positioning of self-assembling Ge islands on Si(111) mesas by using atomic steps*, THIN SOLID FILMS **369**, 88 (2000), 1st Joint Conference on Silicon Epitaxy and Heterostructures (UC-Si), ZAO, JAPAN, SEP 12-17, 1999

[134] H Masui, T Melo, J Sonoda, C Weisbuch, S Nakamura, SP Denbaars, *Effects of Growth Temperature and Postgrowth Annealing on Inhomogeneous Luminescence Characteristics of Green-Emitting InGaN Films*, JOURNAL OF ELECTRONIC MATERIALS **39**, 15 (2010)

[135] M Sawicka, A Feduniewicz-Zmuda, H Turski, M Siekacz, S Grzanka, M Krysko, I Dziecielewski, I Grzegory, C Skierbiszewski, *High quality m-plane GaN grown under nitrogen-rich conditions by plasma assisted molecular beam epitaxy*, JOURNAL OF VACUUM SCIENCE & TECHNOLOGY B **29**, 03C135 (2011)

[136] M Sarzynski, T Suski, G Staszczak, A Khachapuridze, J Z. Domagala, Rrt Czernecki, J Plesiewicz, J. Pawlowska, SP Najda, M Bockowski, P Perlin, M Leszczynski, *Lateral Control of Indium Content and Wavelength of III-Nitride Diode Lasers by Means of GaN Substrate Patterning*, APPLIED PHYSICS EXPRESS **5**, 021001 (2012)

[137] J Neugebauer, TK Zywietz, M Scheffler, JE Northrup, H Chen, RM Feenstra, *Adatom kinetics on and below the surface: The existence of a new diffusion channel*, PHYSICAL REVIEW LETTERS **90**, 056101 (2003)

[138] MJ Galtrey, RA Oliver, MJ Kappers, CJ Humphreys, PH Clifton, D Larson, DW Saxey, A Cerezo, *Three-dimensional atom probe analysis of green- and blue-emitting In(x)Ga(1-x)N/GaN multiple quantum well structures*, JOURNAL OF APPLIED PHYSICS **104**, 013524 (2008)

[139] JY Kim, Y Tak, JW Lee, HG Hong, S Chae, H Choi, M Bokki, Y Park, M Kim, S Lee, N Cha, Y Shin, JR Kim, JI Shim, *Highly efficient InGaN/GaN blue LED grown on Si (111) substrate*, in *2011 CONFERENCE ON LASERS AND ELECTRO-OPTICS (CLEO)* (IEEE, 345 E 47TH ST, NEW YORK, NY 10017 USA, 2011), Conference on Lasers and Electro-Optics (CLEO), Baltimore, MD, MAY 01-06, 2011

[140] M Leroux, N Grandjean, J Massies, B Gil, P Lefebvre, P Bigenwald, *Barrier-width dependence of group-III nitrides quantum-well transition energies*, PHYSICAL REVIEW B **60**, 1496 (1999)

[141] S Kalliakos, P Lefebvre, XB Zhang, T Taliercio, B Gil, N Grandjean, B Damilano, J Massies, *The effects of localization and of electric fields on LO-phonon-exciton coupling in InGaN/GaN quantum wells and quantum boxes*, PHYSICA STATUS SOLIDI A-APPLIED RESEARCH **190**, 149 (2002), International Workshop on Physics of Light-Matter Coupling in Nitrides (PLMCN-1), ROME, ITALY, SEP 26-29, 2001

[142] W. G. Scheibenzuber, U. T. Schwarz, L. Sulmoni, J. Dorsaz, J. F. Carlin, N. Grandjean, *Recombination coefficients of GaN-based laser diodes*, JOURNAL OF APPLIED PHYSICS **109**, 093106 (2011)

[143] G Cosendey, A Castiglia, G Rossbach, JF Carlin, N Grandjean, *Blue monolithic AlInN-based vertical cavity surface emitting laser diode on free-standing GaN substrate*, APPLIED PHYSICS LETTERS **101**, 151113 (2012)

[144] MA Reshchikov, H Morkoc, *Luminescence properties of defects in GaN*, JOURNAL OF APPLIED PHYSICS **97**, 061301 (2005)

[145] JL Lyons, A Janotti, CG Van de Walle, *Carbon impurities and the yellow luminescence in GaN*, APPLIED PHYSICS LETTERS **97**, 152108 (2010)

[146] D Queren, M Schillgalies, A Avramescu, G Bruederl, A Laubsch, S Lutgen, U Strauss, *Quality and thermal stability of thin InGaN films*, JOURNAL OF CRYSTAL GROWTH **311**, 2933 (2009), 2nd International Symposium on Growth of III Nitrides (ISGN-2), Laforet Shuzenji, JAPAN, JUL 07-09, 2008

[147] D Queren, A Avramescu, M Schillgalies, M Peter, T Meyer, G Bruederl, S Lutgen, U Strauss, *Epitaxial design of 475 nm InGaN laser diodes with reduced wavelength shift*, in Butte, R (Hg.), *PHYSICA STATUS SOLIDI C: CURRENT TOPICS IN SOLID STATE PHYSICS, VOL 6, SUPPL 2*, Band 6 von *Physica Status Solidi C-Current Topics in Solid State Physics*, S826–S829 (WILEY-V C H VERLAG GMBH, PAPPELALLEE 3, W-69469 WEINHEIM, GERMANY, 2009), International Workshop on Nitride Semiconductors, Montreux, SWITZERLAND, OCT 06-10, 2008

[148] LT Romano, MD McCluskey, CG Van de Walle, JE Northrup, DP Bour, M Kneissl, T Suski, J Jun, *Phase separation in InGaN multiple quantum wells annealed at high nitrogen pressures*, APPLIED PHYSICS LETTERS **75**, 3950 (1999)

[149] K Jacobs, B Van Daele, MR Leys, I Moerman, G Van Tendeloo, *Effect of growth interrupt and growth rate on MOVPE-grown InGaN/GaN MQW structures*, JOURNAL OF CRYSTAL GROWTH **248**, 498 (2003), 11th International Conference on Metalorganic Vapor Phase Epitaxy, BERLIN, GERMANY, JUN 03-07, 2002

[150] B Van Daele, G Van Tendeloo, K Jacobs, I Moerman, MR Leys, *Formation of metallic In in InGaN/GaN multiquantum wells*, APPLIED PHYSICS LETTERS **85**, 4379 (2004)

[151] JE Northrup, LT Romano, J Neugebauer, *Surface energetics, pit formation, and chemical ordering in InGaN alloys*, APPLIED PHYSICS LETTERS **74**, 2319 (1999)

[152] MD McCluskey, LT Romano, BS Krusor, DP Bour, NM Johnson, S Brennan, *Phase separation in InGaN/GaN multiple quantum wells*, APPLIED PHYSICS LETTERS **72**, 1730 (1998)

[153] TV Shubina, SV Ivanov, VN Jmerik, DD Solnyshkov, VA Vekshin, PS Kop'ev, A Vasson, J Leymarie, A Kavokin, H Amano, K Shimono, A Kasic, B Monemar, *Mie resonances, infrared emission, and the band gap of InN*, PHYSICAL REVIEW LETTERS **92**, 117407 (2004)

[154] S Limpijumnong, CG Van de Walle, *Diffusivity of native defects in GaN*, PHYSICAL REVIEW B **69**, 035207 (2004)

[155] H Wang, AB Chen, *Calculation of shallow donor levels in GaN*, JOURNAL OF APPLIED PHYSICS **87**, 7859 (2000)

[156] J Neugebauer, CG Van de Walle, *Gallium vacancies and the yellow luminescence in GaN*, APPLIED PHYSICS LETTERS **69**, 503 (1996)

[157] MA Reshchikov, P Visconti, H Morkoc, *Blue photoluminescence activated by surface states in GaN grown by molecular beam epitaxy*, APPLIED PHYSICS LETTERS **78**, 177 (2001)

[158] F Shahedipour, BW Wessels, *Investigation of the formation of the 2.8 eV luminescence band in p-type GaN : Mg*, APPLIED PHYSICS LETTERS **76**, 3011 (2000)

[159] CC Chuo, CM Lee, TE Nee, JI Chyi, *Effects of thermal annealing on the luminescence and structural properties of high indium-content InGaN/GaN quantum wells*, APPLIED PHYSICS LETTERS **76**, 3902 (2000)

[160] CC Chuo, MN Chang, FM Pan, CM Lee, JI Chyi, *Effect of composition inhomogeneity on the photoluminescence of InGaN/GaN multiple quantum wells upon thermal annealing*, APPLIED PHYSICS LETTERS **80**, 1138 (2002)

[161] Q Wang, T Wang, J Bai, AG Cullis, PJ Parbrook, F Ranalli, *Influence of annealing temperature on optical properties of InGaN quantum dot based light emitting diodes*, APPLIED PHYSICS LETTERS **93**, 081915 (2008)

[162] AY Egorov, D Bernklau, B Borchert, S Illek, D Livshits, A Rucki, M Schuster, A Kaschner, A Hoffmann, G Dumitras, MC Amann, H Riechert, *Growth of high quality InGaAsN heterostructures and their laser application*, JOURNAL OF CRYSTAL GROWTH **227**, 545 (2001), 11th International Conference on Molecular Beam Epitaxy (MBE-XI), BEIJING, PEOPLES R CHINA, SEP 11-15, 2000

[163] AG Bhuiyan, A Hashimoto, A Yamamoto, *Indium nitride (InN): A review on growth, characterization, and properties*, JOURNAL OF APPLIED PHYSICS **94**, 2779 (2003)

[164] Y Nanishi, Y Saito, T Yamaguchi, *RF-molecular beam epitaxy growth and properties of InN and related alloys*, JAPANESE JOURNAL OF APPLIED PHYSICS PART 1-REGULAR PAPERS SHORT NOTES & REVIEW PAPERS **42**, 2549 (2003)

[165] SV Ivanov, TV Shubina, VN Jmerik, VA Vekshin, PS Kop'ev, B Monemar, *Plasma-assisted MBE growth and characterization of InN on sapphire*, JOURNAL OF CRYSTAL GROWTH **269**, 1 (2004), 1st International Workshop on Indium Nitride, Fremantle, AUSTRALIA, NOV 16-20, 2003

[166] CS Gallinat, G Koblmueller, JS Brown, JS Speck, *A growth diagram for plasma-assisted molecular beam epitaxy of In-face InN*, JOURNAL OF APPLIED PHYSICS **102**, 064907 (2007)

[167] M Mesrine, N Grandjean, J Massies, *Efficiency of NH3 as nitrogen source for GaN molecular beam epitaxy*, APPLIED PHYSICS LETTERS **72**, 350 (1998)

[168] T Bottcher, S Einfeldt, V Kirchner, S Figge, H Heinke, D Hommel, H Selke, PL Ryder, *Incorporation of indium during molecular beam epitaxy of InGaN*, APPLIED PHYSICS LETTERS **73**, 3232 (1998)

[169] A Dussaigne, B Damilano, N Grandjean, J Massies, *In surface segregation in InGaN/GaN quantum wells*, JOURNAL OF CRYSTAL GROWTH **251**, 471 (2003), 12th International Conference on Molecular Beam Epitaxy (MBE-XII), SAN FRANCISCO, CALIFORNIA, SEP 15-20, 2002

[170] CG Van de Walle, J Neugebauer, *First-principles calculations for defects and impurities: Applications to III-nitrides*, JOURNAL OF APPLIED PHYSICS **95**, 3851 (2004)

[171] E Tournie, MA Pinault, A Guzman, *Mechanisms affecting the photoluminescence spectra of GaInNAs after post-growth annealing*, APPLIED PHYSICS LETTERS **80**, 4148 (2002)

[172] A Hierro, JM Ulloa, JM Chauveau, A Trampert, MA Pinault, E Tournie, A Guzman, JL Sanchez-Rojas, E Calleja, *Annealing effects on the crystal structure of GaInNAs quantum wells with large In and N content grown by molecular beam epitaxy*, JOURNAL OF APPLIED PHYSICS **94**, 2319 (2003)

[173] T Fujii, Y Gao, R Sharma, EL Hu, SP DenBaars, S Nakamura, *Increase in the extraction efficiency of GaN-based light-emitting diodes via surface roughening*, APPLIED PHYSICS LETTERS **84**, 855 (2004)

[174] L Geelhaar, M Galluppi, G Jaschke, R Averbeck, H Riechert, T Remmele, M Albrecht, M Dworzak, R Hildebrant, A Hoffmann, *Influence of structural nonuniformity and nonradiative processes on the luminescence efficiency of InGaAsN quantum wells*, APPLIED PHYSICS LETTERS **88**, 011903 (2006)

[175] XJ Wang, Y Puttisong, CW Tu, AJ Ptak, VK Kalevich, AY Egorov, L Geelhaar, H Riechert, WM Chen, IA Buyanova, *Dominant recombination centers in Ga(In)NAs alloys: Ga interstitials*, APPLIED PHYSICS LETTERS **95**, 241904 (2009)

[176] F Tuomisto, V Ranki, DC Look, GC Farlow, *Introduction and recovery of Ga and N sublattice defects in electron-irradiated GaN*, PHYSICAL REVIEW B **76**, 165207 (2007)

[177] CC Chuo, CM Lee, JI Chyi, *Interdiffusion of In and Ga in InGaN/GaN multiple quantum wells*, APPLIED PHYSICS LETTERS **78**, 314 (2001)

[178] O Ambacher, F Freudenberg, R Dimitrov, H Angerer, M Stutzmann, *Nitrogen effusion and self-diffusion in (GaN)-N-14/(GaN)-N-15 isotope heterostructures*, JAPANESE JOURNAL OF APPLIED PHYSICS PART 1-REGULAR PAPERS SHORT NOTES & REVIEW PAPERS **37**, 2416 (1998)

[179] KH Chow, GD Watkins, A Usui, M Mizuta, *Detection of interstitial Ga in GaN*, PHYSICAL REVIEW LETTERS **85**, 2761 (2000)

[180] C Rauch, O Tuna, C Giesen, M Heuken, F Tuomisto, *Point defect evolution in low-temperature MOCVD growth of InN*, PHYSICA STATUS SOLIDI A-APPLICATIONS AND MATERIALS SCIENCE **209**, 87 (2012)

Acronyms

Materials

Ga	Gallium	GaN	Gallium nitride
Al	Aluminum	AlN	Aluminum nitride
In	Indium	InN	Indium nitride
InGaN	Indium gallium nitride	InAlN	Indium aluminum nitride
AlGaN	Aluminum gallium nitride		
NH_3	Ammonia	N^*	Active nitrogen
N_2	(Molecular) nitrogen	H_2	(Molecular) hydrogen
TMIn	Trimethylindium	TMAl	Trimethylaluminum
TMGa	Trimethylgallium	TEGa	Triethylgallium
Mg	Magnesium	Si	Silicon
Ge	Germanium	C	Carbon
Cu	Copper	Pt	Platinum

Miscellaneous

QW	Quantum well	QD	Quantum dot
LED	Light emitting diode	LD	Laser diode
T_{gr}	Growth temperature	V_{gr}	Growth rate
LT	Low temperature	HT	High temperature
RT	Room temperature	T_a	Annealing temperature
TA	Thermal annealing	ML	Monolayer
FS GaN	Free standing GaN	(0-3)D	(0-3) dimensional
ES	Ehrlich-Schwöbel	ESB	Ehrlich-Schwöbel barrier
SESE	Step ES effect	KESE	Kink ES effect
SSE	Self-screening effect	PDC	Point defect curing
V_N	N vacancies	Ga_N	Ga vacancies
N_I	N Interstitials	Ga_I	Ga interstitials
IQE	Internal quantum efficiency	EQE	External quantum efficiency
KMC	Kinetic Monte Carlo simulation	HR	High resolution
rms	Root mean square	FWHM	Full width at half maximum

Techniques

MOVPE	Metal organic vapor phase epitaxy
MBE	Molecular beam epitaxy
NH_3-MBE	Ammonia MBE
PAMBE	Plasma-assisted MBE
HVPE	Hydride vapor phase epitaxy
AFM	Atomic force microscopy
STM	Scanning tunneling microscopy
(HR-) TEM	(High resolution) transmission electron microscopy
SEM	Scanning electron microscopy
(HR-) XRD	(High resolution) X-ray diffraction
QMS	Quadrupole mass spectroscopy
RHEED	Reflection high-energy electron diffraction
EL	Electroluminescence
PL	Photoluminescence
TRPL	Time-resolved PL
PAS	Positron annihilation spectroscopy
ODMR	Optical detected magnetic resonance

Curriculum vitae

First names	Nils Asmus Kristian
Last name	Kaufmann
Date of birth	07.08.1981
Place of birth	Aachen, Germany
Marital status	single
Citizenship	German
E-Mail	nils.kaufmann@epfl.ch

University studies

Since December 2008	PhD thesis as Marie Curie Fellow (ITN RAINBOW) at the École Polytechnique Fédérale de Lausanne (EPFL), Switzerland, in the Laboratory of Advanced Semiconductors for Photonics and Electronics (LASPE)
Oct. 2001-Aug. 2008	Diploma in physics (master degree equivalent) at the Rheinisch Westfälische Technische Hochschule Aachen University (RWTH), Germany in 2008 04/ 2007-06/2008: Internship and master-thesis at Philips Research Laboratories Aachen (PFLA) in cooperation with Aixtron (grade for thesis: 1.3) Title of master-thesis: Exzitonische Tieftemperatur Transientenspektroskopie an LED Strukturen kurzer Moleküle (Excitonic low temperature transient spectroscopy of small molecule LEDs)

07/2004-05/2005: Erasmus year at the NTNU Trondheim, Norway

Education

06 / 2001 - 08 / 1992	High school education at Kaiser Karls Gymnasium, Aachen, Germany. Final grade (Abitur): 1.4
08 / 1988 – 06 / 1992	Elementary school: Katholische Grundschule Passstraße, Aachen, Germany

Language skills

German	Native speaker
English	Business fluent / proficient
French	Intermediate (A2)
Norwegian	Fluent

Miscellaneous

2010-2012	Fellow-representative at the Marie Curie ITN steering committee
Since August 2005	Voluntary service at AEGEE Aachen e.V (Association des Etats Généraux des Etudiants de l´Europe): 2007 board member: treasurer

Lausanne, the 10th of March 2013

Publications

Thermal annealing of molecular beam epitaxy-grown InGaN/GaN single quantum well, **NAK Kaufmann**, A Dussaigne, D Martin, P Valvin, T Guillet, B. Gil, F Ivaldi, S Kret and N Grandjean, SEMICONDUCTOR SCIENCE AND TECHNOLOGY **27**, 105023 (2012)

Strain compensation in AlInN/GaN multilayers on GaN substrates: Application to the realization of defect-free Bragg reflectors, G Cosendey, JF Carlin, **NAK Kaufmann**, R Butte and N Grandjean, APPLIED PHYSICS LETTERS **98**, 181111 (2011)

Investigation of the In composition in InGaN/GaN quantum wells deposited by MOVPE and/or MBE with emission from violet to green, GR Mutta, P Ruterana, JL Doualan, MP Chauvat, F Ivaldi, S Kret, **NAK Kaufmann**, A Dussaigne, D Martin and N Grandjean, PHYSICA STATUS SOLIDI B-BASIC SOLID STATE PHYSICS **248**, 1187-1190 (2011)

Effects of the annealing temperature on the structural and electronic properties of MBE grown InGaN/GaN quantum wells, F Ivaldi, **NAK Kaufmann**, S Kret, A Dussaigne, B Kurowska, M Klepka, J Dabrowski, P Dluzewski and N Grandjean, 17TH INTERNATIONAL CONFERENCE ON MICROSCOPY OF SEMICONDUCTING MATERIALS 2011 Book Series: Journal of Physics Conference Series **326**, 012012 (2011)

TEM and XANES study of MOVPE grown InAlN layers with different indium content, S Kret, A Wolska, MT Klepka, A Letrouit, F Ivaldi, A Szczepanska, JF Carlin, **NAK Kaufmann** and N Grandjean, 17TH INTERNATIONAL CONFERENCE ON MICROSCOPY OF SEMICONDUCTING MATERIALS 2011 Book Series: Journal of Physics Conference Series **326**, 012013 (2011)